INVESTIGATING THE PHOTOTHERAPY POTENTIAL OF NANOPARTICLES IN BRAIN–TUMOR BARRIER MODELS IN VITRO

A THESIS SUBMITTED TO
THE GRADUATE SCHOOL OF NATURAL AND APPLIED SCIENCES
OF
ANKARA UNIVERSITY

by

Esen KİRİT

IN PARTIAL FULFILMENT OF THE REQUIREMENTS
FOR THE DEGREE OF
MASTER OF SCIENCE IN
DEPARTMENT OF BIOMEDICAL ENGINEERING

ANKARA
2025

All rights reserved

ABSTRACT

Master's Thesis

INVESTIGATING THE PHOTOTHERAPY POTENTIAL OF NANOPARTICLES IN BRAIN-TUMOR BARRIER MODELS IN VITRO

Esen KIRIT

Ankara University
Graduate School of Natural and Applied Sciences
Department of Biomedical Engineering

Supervisor: Assoc. Prof. Dr. Açelya YILMAZER AKTUNA

The blood–brain barrier (BBB) and blood–tumor barrier (BBTB) are major obstacles in the treatment of glioblastoma multiforme (GBM), a highly aggressive brain tumor. Light-activated nanoparticles used in photothermal therapy (PTT) and photodynamic therapy (PDT) have shown promise in overcoming these barriers due to their enhanced specificity and reduced invasiveness. However, their transport mechanisms across the BBB/BBTB and their therapeutic effects under nanomaterials and light remain poorly understood. This thesis investigates the phototherapeutic potential of novel fluorescent nanoparticles using in vitro BBB and BBTB transwell models constructed with human brain endothelial cells. Barrier integrity, nanoparticle transport, and cytotoxicity were evaluated under controlled light exposure conditions. The results provide insights into the photothermal and photodynamic effects of fluorescent nanoparticles on the BBB and BBTB. This study could contribute to the development of innovative nanomaterial-based therapies to complement conventional cancer treatments.

September 2025, 103 pages

Key Words: Glioblastoma multiforme, Blood–brain barrier, Blood–tumor barrier, Nanoparticles, Phototherapy, Photothermal therapy, Photodynamic therapy, Cytotoxicity

ÖZET

Yüksek Lisans Tezi

NANOPARTİKÜLLERİN FOTOTERMAL POTANSİYELLERİNİN İN VİTRO BEYİN TÜMÖR BARİYER MODELLERİNDE ARAŞTIRILMASI

Esen KİRİT

Ankara Üniversitesi
Fen Bilimleri Enstitüsü
Biyomedikal Mühendisliği Anabilim Dalı

Danışman: Doç. Dr. Açelya YILMAZER AKTUNA

Kan-beyin bariyeri (KBB) ve kan-tümör bariyeri (KTB), oldukça agresif bir beyin tümörü olan glioblastoma multiforme'un (GBM) tedavisinde önemli engellerdir. Fototermal tedavi (FTT) ve fotodinamik tedavide (FDT) kullanılan ışıkla aktive olan nanopartiküller, gelişmiş özgüllükleri ve azaltılmış invazivlikleri sayesinde bu zorlukların üstesinden gelmede umut vaat etmektedir. Bununla birlikte, bu nanopartiküllerin BBB/BBTB'yi geçme davranışları ve nanomalzeme ile terapisi yapılmış BBB/BBTB'nin terapötik etkileri henüz yeterince anlaşılamamıştır. Bu tez, insan beyin endotel hücreleri ile oluşturulan in vitro kan-beyin bariyeri ve kan-tümör bariyeri modellerinde kullanılan yenilikçi floresan nanopartiküllerin fototerapötik potansiyelini incelemektedir. Bariyerin işleyişi, nanopartiküllerin taşınması ve sitotoksisitesi, düzenli ışık maruziyeti altında değerlendirilmiştir. Bulgular, floresan nanopartiküllerin; kan-beyin bariyeri ve kan tümör bariyeri üzerine fototermal ve fotodinamik etkileri hakkında fikir sahibi olmamıza yardımcı olacaktır. Bu sayede geleneksel kanser tedavilerinin yanı sıra yenilikçi nanomalzeme terapilerinin de yolunu açacaktır.

Eylül 2025, 103 sayfa

Anahtar kelimeler: Glioblastoma multiforme, Kan-beyin bariyeri, Kan-tümör bariyeri, Nanopartiküller, Fototerapi, Fototermal tedavi, Fotodinamik tedavi, Sitotoksisite

FOREWORD and ACKNOWLEDGEMENTS

This thesis is more than an academic work for me; it is a journey that began with a purpose, shaped by the people, memories, and hopes that walked beside me.

First and foremost, I dedicate this work to the memory of Hatice Zehra Güney and her beloved mother, whose story has been my deepest source of motivation, whose courage and strength have inspired me throughout this path.

I would like to express my heartfelt gratitude to Assoc. Prof. Dr. Açelya YILMAZER AKTUNA for guiding me not only as a supervisor but also as a mentor who shared her wisdom, patience, and encouragement at every step. Her belief in me has been a light on days when the road felt too heavy.

I am thankful to Prof. Dr. Sanjiv DHINGRA for kindly providing the MXene Quantum Dots (MQDs) that made this research possible, and to Res. Asst. Abdullah EYİDOĞAN and Res. Asst. Oğuzhan PANATLI for their support and valuable contributions in the academic life.

To my amazing lab mates and friends—Umay KOPARAN, Cansu GÜRCAN KARATEPE, Cemile GÖKÇE, Buse ALTUN, and all the other teammates who stood by me—thank you for the laughs, the coffee breaks, the brainstorming sessions, and for reminding me that research is as much about people as it is about data.

I gratefully acknowledge the Scientific and Technical Research Council of Turkey (TUBITAK) for their financial support through the 1004 Center of Excellence Support Program, and the Ankara University Biomedical Engineering Department for providing the necessary materials and facilities.

To my precious kitten, whose quiet company and soft purrs kept me grounded during endless hours of writing and experiments — you made this journey warmer. The North Star has always been a symbol of guidance and hope in my life — a steady light in the distance that reminded me where I was headed, even in moments when the path was unclear.

Most importantly, my deepest gratitude belongs to my family.

To my mother, Ayşe Esra ÜNLÜER, who, even without fully understanding the technical details of my work, always listened with patience, found her special ways to encourage me, and, above all, has been my mother — whose sacrifices and unconditional love have carried me through every stage of my life.

To my grandparents, Mehmet Hidayet ÜNLÜER and Mümine ÜNLÜER, whose unwavering faith in me has been a constant source of strength. To my dear aunt, Ayşe Zeynep ÜNLÜER, for her endless encouragement; to my sister, Ece ÖZER, for being my lifelong friend; and to my uncle, Ömer ÜNLÜER, and his dear wife Hande ÜNLÜER, for their generosity, care, and support — both emotional and financial — which have made this journey possible.

I truly owe this achievement to each of you, and your belief in me will forever remain one of the most valuable gifts I carry forward.

This thesis carries all of you in its pages.

Esen KİRİT
Ankara, September 2025

TABLE OF CONTENTS

THESIS APPROVAL
ETHIC ..... **i**
ABSTRACT ..... **ii**
ÖZET ..... **iii**
FOREWORD and ACKNOWLEDGEMENTS ..... **iv**
LIST OF SYMBOLS ..... **ix**
LIST OF FIGURES ..... **xi**
LIST OF TABLES ..... **xiii**
1. INTRODUCTION **1**
2. LITERATURE SURVEY **3**
2.1 BBB, BBTB, and Their Comparison **3**
2.1.1 Structural and cellular composition of the BBB **3**
2.1.1.1 BMECs **5**
2.1.1.2 TJ complexes **6**
2.1.1.3 Astrocytes: inducers and modulators of barrier phenotype **7**
2.1.1.4 Pericytes and their regulatory functions **8**
2.1.1.5 BM and ECM **10**
2.1.1.6 Adherens junctions **11**
2.1.2 Neovascular heterogeneity and pericyte dynamics **13**
2.2 Structural and Functional Alterations Defining the BBTB **15**
2.2.1 Pathological transition to the BBTB in GBM **17**
2.2.2 Functional implications of barrier heterogeneity on therapeutic transport **17**
2.2.3 Clinical implications of BBTB heterogeneity for drug delivery **19**
2.2.4 Therapeutic strategies targeting the BBTB **20**
2.3 NP Transport Mechanisms Across the Brain Endothelium **21**
2.3.1 Paracellular and transcellular routes of nanomaterial translocation **22**
2.3.2 Active vs. passive strategies for barrier penetration **22**
2.3.3 Hybrid and stimuli-responsive strategies **23**
2.3.4 Influence of physicochemical properties on endothelial interaction **24**
2.4 Photoresponsive Nanotherapeutics For BBTB **25**
2.4.1 Fundamentals of PTT and PDT mechanisms **25**
2.4.2 Design criteria for light-activatable NPs in CNS applications **27**
2.4.2.1 Optical properties and photothermal conversion efficiency **27**

2.4.2.2 Size and surface characteristics for BBB penetration 27
2.4.2.3 Responsiveness to stimuli and controlled release 28
2.4.2.4 Tumor targeting and biomimicry 28
2.4.2.5 Clearance and biodegradability 28
2.4.2.6 Theranostic integration 28
2.4.3 Synergistic integration of PTT and PDT in nanomedicine platforms 30
2.5 In Vitro Modeling of the BBTB for Nanomaterial Evaluation 31
2.5.1 Static monoculture vs multicellular co-culture systems 32
2.5.2 Transwell models as a framework for the BBB and BBTB 33
2.5.3 Electrophysiological and permeability assessments for barrier validation 35
2.5.3.1 TEER assessments 35
2.5.3.2 Paracellular permeability evaluations 36
2.5.3.3 Consolidated utilization and functional analysis 36
2.6 Assessment of Cytotoxicity and Functional Responses in Phototherapy Research 37
2.6.1 Summary of conventional in vitro toxicological assays for NPs 38
2.6.2 Application of live/dead cell staining in barrier-integrated models 39
2.7 Methodological Limitations and Developing Opportunities for BBB and BBTB 41
3. MATERIAL AND METHODS 45
3.1 Materials 45
3.2 Methods 47
3.2.1 Culture of the cell lines 48
3.2.1.1 Thawing of cell lines 48
3.2.1.2 Cell culture and passaging protocol for hCMEC/D3 48
3.2.1.3 Cryopreservation of hCMEC/D3 50
3.2.1.4 Subculturing of hCMEC/D3 for BBB constructions 50
3.2.1.5 Culturing of U87 Cancer Cell Line 51
3.2.2 Formation of in vitro BBTB models 53
3.2.2.1 Models with hCMEC/D3 and U87 53
3.2.3 Cytotoxicity assay in BBTB models 54
3.2.3.1 Optimization of proper Mxene type, concentration, and wavelength 54
3.2.3.2 Protocol for phototherapy exposure in cytotoxicity assessment 55
3.2.3.3 LDH assay for viability assessment after PTT & PDT 56
3.3 Live/Dead Cell Staining Protocol In Transwell-Based co-culture Model 57
3.4 Statistical Analysis 59

4. RESULTS 60
4.1 Determination of Appropriate Material Concentration and Wavelength 60
4.2 Live/Dead Assay Results 67
4.3 Intensity of Live/Dead Assay Results 73
5. DISCUSSION 79
6. CONCLUSION 84
REFERENCES 86
CURRICULUM VITAE 103

LIST OF SYMBOLS

mm	Millimeter
nm	Nanometer
µg	Microgram
µl	Microliter
µm	Micrometer
min	Minute
h	Hour

Abbreviations

ABCB1	P-glycoprotein
ABCG2	Breast Cancer Resistance Protein
AAV	Adeno-Associated Virus
AJ	Adherens Junction
AQP4	Aquaporin-4
ATCC	American Type Culture Collection
BSA	Bovine Serum Albumin
BBB	Blood–Brain Barrier
BBTB	Blood–Brain Tumor Barrier
BM	Basement Membrane
BMECs	Brain Microvascular Endothelial Cells
CNS	Central Nervous System
CT	Computed Tomography
DPBS	Dulbecco's phosphate-buffered saline
EC	Endothelial Cell
ECM	Extracellular Matrix
ESAM	Endothelial cell–Selective Adhesion Molecule
ESIPT	Excited-state Intramolecular Proton Transfer
EthD-1	Ethidium Homodimer-1
FBS	Fetal Bovine Serum
FGF2	Fibroblast Growth Factor
FUS	Focused Ultrasound
GBM	Glioblastoma Multiforme
GDNF	Glial-derived Neurotrophic Factor
GLUT1	Glucose Transporter 1
GSCs	Glioma Stem-like Cells
HSPs	Heat Shock Proteins
ICD	Immunogenic Cell Death
IL-1β	Interleukin-1β
IL-6	Interleukin-6
ILM	Inverted Light Microscopy
JAMs	Junctional Adhesion Molecules
LAT1	Large neutral Amino acid Transporter 1

LDH	Lactate Dehydrogenase
MEM	Minimum Essential Medium
MHC	Major Histocompatibility Complex
MLCK	Myosin Light Chain Kinase
MQD	MXene Quantum Dots
MSC	Mesenchymal Stem Cells
NPs	Nanoparticles
NVU	Neurovascular Unit
OCLN	Occludin
P/S	Penicillin–Streptomycin
PECAM-1	Platelet Endothelial Cell Adhesion Molecule-1
PDT	Photodynamic Therapy
PKC	Protein kinase C
PS	Photosensitizer
PTT	Photothermal Treatment
QSAR	Quantitative Structure–Activity Relationship
rhEGF	Recombinant Human EGF
RMT	Receptor-Mediated Transcytosis
ROS	Reactive Oxygen Species
Shh	Sonic hedgehog
Ta_4C_3	Tantalum carbide derived.
TGF-β	Transforming Growth Factor-β
Ti_3C_2	Titanium carbide derived
Ti+Ta	Tantalum and Titanium combined solution
TJP	Tight Junction Protein
TJs	Tight Junctions
TNF-α	Tumor Necrosis Factor-α
VEGF	Vascular Endothelial Growth Factor
ZO-1	Zonula Occludens-1
2D	Two-Dimensional
3D	Three-dimensional

LIST OF FIGURES

Figure 2.1 Structure of the neurovascular unit and cross-section structure of the BBB ... 5
Figure 2.2 Comparison of the BBB and GBM-Affected Brains ... 15
Figure 2.3 Representation of NP-mediated photothermal PTT and photodynamic PDT therapy in GBM ... 27
Figure 3.1 (A)Visualized image under ILM and (B) realistic hemocytometer image on ILM ... 50
Figure 3.2 ILM images of hCMEC/D3 cell line at passage +4 (A: 10X, scale bar: 100 μM, B: 20X, scale bar: 50 μM) ... 51
Figure 3.3 ILM image of U87 at passage +7 (A: 10X, scale bar: 100 μM, B: 20X, scale bar: 50 μM) ... 52
Figure 3.4 Co-culture protocol (Created by BioRender) ... 53
Figure 3.5 Illustration of Photothermal and Photodynamic Therapy Protocol ... 56
Figure 3.6 Experimental setups for Naive, Indirect, and Direct conditions in the hCMEC/D3–U87 Transwell co-culture model ... 58
Figure 4.1 Cell viability of U87 cells. The cells treated with 520 nm and Tantalum carbide derived MQD after PTT & PDT protocol (n=5, P value>0.05) ... 61
Figure 4.2 Cell viability of U87 cells. The cells treated with 850 nm and Tantalum carbide derived MQD after PTT & PDT protocol (n=5, P value>0.05) ... 62
Figure 4.3 Cell viability of U87 cells. The Cells treated with 520 nm and Titanium carbide derived MQD after PTT & PDT protocol (n=5, P value>0,05) ... 63
Figure 4.4 Cell viability of U87 cells. The cells treated with 850 nm and Titanium carbide derived MQD after PTT & PDT protocol (n=5, *P value<0,05) ... 64
Figure 4.5 Cell viability of U87.The cancer cells treated with 520 nm, Ti+Ta combination MQD after PTT & PDT protocol (n=5, P value>0,05) ... 65
Figure 4.6 Cell viability of U87 cells.The cells treated with 850 nm, Ti+Ta combination MQD after PTT & PDT protocol (n=5, *P value<0,05) ... 66
Figure 4.7 Schematic workflow of hCMEC/D3 and U87 co-culture in the Transwell system for Live/Dead cell viability assay (Created by BioRender) ... 67
Figure 4.8 Representative Live/Dead fluorescence microscopy images of U87 glioblastoma cells (A) and hCMEC/D3 endothelial cells (Bin the groups. Scale bar: 200 μm ... 68
Figure 4.9 Representative Live/Dead fluorescence microscopy images of U87 glioblastoma cells (left) and hCMEC/D3 endothelial cells (right) in the Indirect group (Transwell configuration). Scale bar: 200 μm ... 69
Figure 4.10 Representative Live/Dead fluorescence microscopy images of U87 glioblastoma cells (A) and hCMEC/D3 endothelial cells (B) in the Direct group.Scale bar: 200 μm ... 71

Figure 4.11 Live/Dead fluorescence intensity profiles and quantification of naïve U87 and hCMEC/D3 cells 73
Figure 4.12 Live/Dead fluorescence intensity profiles and quantification of U87 and hCMEC/D3 cells in the Indirect (Transwell) group 75
Figure 4.13 Live/Dead fluorescence intensity profiles and quantification of U87 and hCMEC/D3 cells in the Direct group 77

LIST OF TABLES

Table 2.1 Comparative overview of passive and active nanoparticle transport mechanisms 23

Table 2.2 Summary of design criteria and representative examples of light-activatable nanoparticles for CNS applications 29

Table 3.1 Cell types and cell culture materials used in the thesis 45

Table 3.2 Comparative overview of Ti_3C_2 and Ta_4C_3 Mxenes in light-activated cancer treatment 46

Table 3.3 Assay types, assay materials, and devices used in the thesis 46

Table 3.4 Culture conditions and seeding parameters for hCMEC/D3 and U87 cell lines 52

Table 3.5 Summary of Mxene NP types with corresponding concentrations and light wavelengths 55

1. INTRODUCTION

GBM is among the most aggressive and is resistant to the therapeutic forms of tumors in the brain. Conventional therapies, including surgery, radiation, and chemotherapy, can extend survival but are insufficient to prevent recurrence. Innovative approaches like immunotherapy, targeted pharmacological drugs, nanotechnology-based drug delivery mechanisms, and gene therapy are being explored to mitigate the limitations. Overcoming the restrictions of the BBB and BBTB plays a crucial role in the fight against GBM for the advancement of innovative cancer treatments (El Kheir et al., 2022; D. Liu et al., 2023; Stylli, 2020).

Recent nanotechnology-based approaches, particularly those capable of traversing the BBB and BBTB, have shown promise in GBM therapy. Nanoparticles (NPs) enable controlled drug delivery and release across these barriers owing to their tunable size, surface properties, and carrier capabilities. Light-activated nanotherapies, including PDT and PTT, provide enhanced accuracy, less systemic toxicity, and the capability to destroy tumor cells with selection. PTT elevates local temperatures to cause apoptosis in tumor cells, whereas PDT employs light-activated photosensitizers (PS) to produce reactive oxygen species (ROS) (Fang et al., 2024; Hsu et al., 2021; M. Zhang et al., 2021).

The BBB and BBTB's intricate architecture pose considerable obstacles for the implementation of NP-based phototherapies. Nowadays, there is an absence of physiologically pertinent in vitro models to assess their transport pathways and therapeutic effectiveness. Conventional static monolayer models inadequately mimic the multicellular structure, tight junction (TJ) stability, and dynamic control of the neurovascular unit (NVU), hence limiting their prediction accuracy for in vivo results (Tsai et al., 2018; H. Wu et al., 2020). Therefore, advanced BBB/BBTB models in vitro incorporating endothelial cells (ECs), glioma cells, and co-culture systems are essential for assessing NP permeability and phototherapeutic potential (Hanada et al., 2014; Kaya, Callan, & Hawthorne, 2023; Lubin, Xu, Sluka, & Knipp, 2024). Combining these models with functional assessments such as transendothelial electrical resistance (TEER),

live/dead cell imaging, and permeability assays can provide comprehensive insights into NP–barrier interactions and potential adverse effects under controlled conditions.

This thesis aims to address a significant deficit, since no prior research has thoroughly investigated the phototherapeutic effects of MXene quantum dots (MQDs) on physiologically pertinent BBB and BBTB models. Although various nanomaterials, including gold, copper sulfide, Prussian blue, and graphene derivatives, have been assessed for glioblastoma treatment, they have been mostly examined in direct tumor cultures or animal models, without integration into barrier-based systems. This research established static and co-culture Transwell models of the BBB/BBTB to investigate the capacity of titanium carbide ($Ti_3C_2T_x$) and tantalum carbide ($Ta_4C_3T_x$) MQDs to traverse endothelial barriers, assess their impact on glioblastoma and endothelial cell viability, and identify the molecular determinants influencing their light-activated responses. This study presents the inaugural demonstration of integrating two distinct MQDs within BBB/BBTB models, positing that their complementary photothermal and photodynamic properties will synergistically enhance cytotoxicity against glioblastoma cells compared to either material individually, while maintaining endothelial function.

2. LITERATURE SURVEY

2.1 BBB, BBTB, and Their Comparison

2.1.1 Structural and cellular composition of the BBB

The BBB is a semi-permeable and dynamic interface composed of brain microvascular endothelial cells (BMECs) that border the blood vessels within the CNS. The primary function is to facilitate the bidirectional transfer of ions, chemicals, antibodies, and more between the peripheral blood circulation and the cerebral microenvironment. It maintains cerebral homeostasis and functional autonomy from external disruptions (Abbott, Patabendige, Dolman, Yusof, & Begley, 2010; Hawkins & Davis, 2005).

Anatomically and physiologically, as shown in Figure 2.1, the BBB is a basic and crucial element of the NVU, a meticulously organized multicellular assembly that regulates cerebral blood flow, supplies anatomical and physiological support, and enables neuroimmune interactions. The NVU consists of ECs, pericytes, astrocytes, and a specific extracellular matrix referred to as the basement membrane (BM). Every component aids in upholding the integrity of the barrier, restricting the uncontrolled movement of molecules, maintaining CNS homeostasis, and guaranteeing accurate neuronal transmission.

BMECs are positioned at the forefront of the barrier, forming a continuous monolayer that covers the cerebral microvasculature. Unlike ECs, BMECs are devoid of fenestrations, demonstrate extremely minimal percentages of transcytosis, and are connected by TJs that include occludin (OCLN), claudin-5, and zonula occludens-1 (ZO-1) proteins. These structures reduce the paracellular space and prevent passive diffusion of solutes (Nitta et al., 2003).BMECs also express specialized carriers like glucose transporter 1 (GLUT1), large neutral amino acid transporter 1 (LAT1), and P-glycoprotein (ABCB1), which facilitate targeted transcellular transport while restricting CNS entry of xenobiotics and harmful agents (Daneman & Prat, 2015; S. W. L. Lee et al., 2020)

Pericytes are mural cells located inside the BM and in immediate direct physical contact with BMECs. They are crucial for preserving vascular integrity, facilitating angiogenesis, and regulating BBB permeability through signaling pathways such as PDGFR-β and TGF-β. The experimental ablation of pericytes leads to increased BBB permeability, aberrant capillary shape, and elevated leukocyte infiltration (Armulik et al., 2010; Bell et al., 2010).

Astrocytes, characterized by their star-shaped and end-feet, envelop over 90% of the abluminal surface of cerebral capillaries. These structures are abundant in aquaporin-4 (AQP4) water channels and inversely conducting potassium channels, enabling the regulation of extracellular ion and water balance in response to neuronal activity (Simard & Nedergaard, 2004). Astrocytes release bioactive chemicals, including glial-derived neurotrophic factor (GDNF), which enhance BMEC activity and maintain TJ integrity (Abbott, Rönnbäck, & Hansson, 2006).

The BM, composed primarily of laminin isoforms (α4 and α5), collagen type IV, nidogen, and heparan sulfate proteoglycans, provides the structural scaffold for BBB cellular components. It supports cell adhesion, defines polarity, and localizes signaling molecules essential for barrier maintenance and repair (Halfter, Dong, Yip, Willem, & Mayer, 2002). Disruption or degradation of the BM, often mediated by matrix metalloproteinases (MMP-2, MMP-9), increases permeability and is associated with neuroinflammatory and neoplastic pathologies.

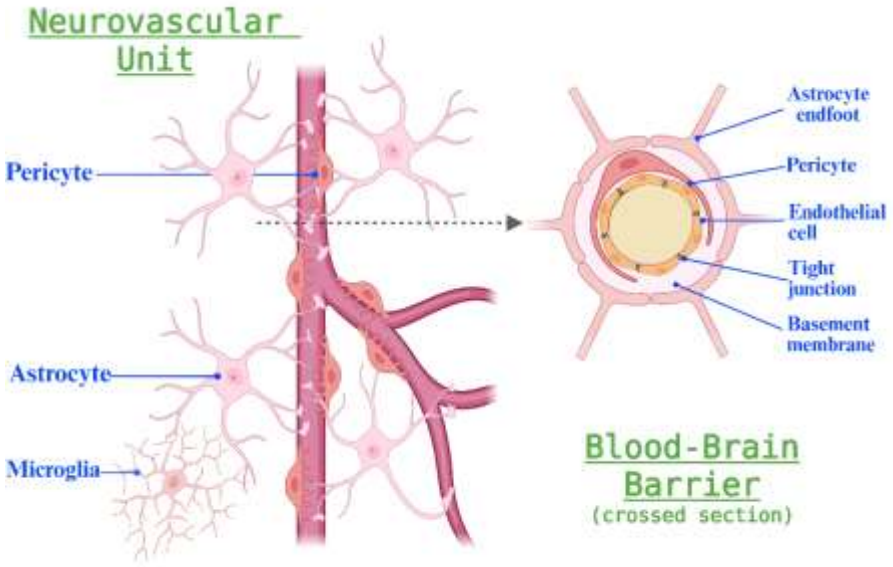

Figure 2.1 Structure of the neurovascular unit and cross-section structure of the BBB (Created by BioRender)

2.1.1.1 BMECs

BMECs are crucial for the structure of the BBB and serve as a physiological component of the barrier, imparting its selective semipermeable characteristics. Their principal roles encompass protecting neural tissue and controlling the translocation of chemicals into the CNS. BMECs have transcytotic vesicle production and establish continuous tight intercellular connections, leading to elevated high TEER values and limited paracellular permeability (Abbott et al., 2010).

At the molecular level, BMECs produce various TJ and adherens junction (AJ) proteins that provide mechanical stability and maintain barrier integrity. Among TJ components are claudin-5, which regulates size-selective paracellular permeability; OCLN, which contributes to junctional assembly and signal transduction; and ZO-1, a scaffold protein that anchors TJ compounds to the actin cytoskeleton and mediates intracellular signaling (Furuse et al., 1993; Hawkins & Davis, 2005; Nitta et al., 2003).

Beyond their structural role, BMECs are metabolically active and exhibit a variety of solute carrier (SLC) and ABC transporters, which bind to ATP, in order to modulate

transcellular nutrient uptake while restricting xenobiotics and neurotoxicants. Notable examples include GLUT1 for glucose uptake, LAT1 for amino acids and thyroid hormones, and the efflux pumps ABCB1 and the resistance protein of breast cancer (ABCG2) for the removal of lipophilic drugs (da Silva Chaves, 2016; Löscher & Potschka, 2005b). These transporters are polarized across luminal and abluminal membranes, supporting the metabolic demands of the CNS while maintaining pharmacological selectivity.

In addition, BMECs produce enzymes like monoamine oxidase, alkaline phosphatase, and γ-glutamyl transpeptidase to degrade potentially harmful compounds before they reach the brain parenchyma. Immunologically, BMECs exhibit low baseline expression of major histocompatibility complex (MHC) molecules under homeostatic conditions but can upregulate adhesion molecules and cytokines during inflammation, promoting leukocyte recruitment and neuroimmune surveillance (Engelhardt & Ransohoff, 2005). Under pathological stress, such as ischemia, infection, or tumorigenesis, these cells may lose their regulatory capacity, leading to endothelial dysfunction and BBB disruption.

2.1.1.2 TJ complexes

TJs create a continuous, belt-like junction in the apicolateral region of BMECs, restricting the paracellular movement of hydrophilic molecules, thereby enhancing the BBB's very high TEER (Abbott et al., 2010).

The BBB's TJ complex mostly consists of transmembrane proteins, primarily of claudin-5, OCLN, and junctional adhesion molecules (JAMs), which collectively establish a continuous intercellular barrier. Claudin-5 is essential for restricting the paracellular diffusion of low-molecular-weight substances; its genetic deletion markedly enhances permeability to molecules under 800 Da, underscoring its significance in molecular size selectivity (Nitta et al., 2003). OCLN, not crucial for the TJ strands formation, regulates barrier permeability through phosphorylation-dependent mechanisms (Furuse et al., 1993; Saitou et al., 2000). JAM-A promotes cell-to-cell adhesion and facilitates leukocyte transmigration. It also interacts with scaffold protein (Bazzoni et al., 2000).

Multiple signaling pathways dynamically regulate TJs. Protein kinase C (PKC) and myosin light chain kinase (MLCK) influence TJ assembly by phosphorylating junctional proteins, whereas Rho family GTPases control actin cytoskeletal organization and endothelial stiffness (Garcia et al., 1995). Pro-inflammatory mediators such as necrosis of tumor cells factor-α (TNF-α), interleukin-1β (IL-1β), and bradykinin can induce internalization or degradation of TJPs, thereby compromising barrier integrity and increasing paracellular permeability (Mark & Davis, 2002).

Thus, TJ dysfunction is a characteristic of several neurological diseases and is often linked to heightened BBB permeability and neuroinflammation.

2.1.1.3 Astrocytes: inducers and modulators of barrier phenotype

Astrocytes, among the various glial cell types in the CNS, are essential for the maintenance and dynamic regulation of the BBB. As key components of the NVU, astrocytes extend specialized processes known as end-feet, which envelop approximately 90% of the brain capillaries abluminal surface (Simard & Nedergaard, 2004). These end-feet from the gliovascular interface enable bidirectional communication between neurons and the vascular compartment.

Astrocytes contribute to BBB function through diverse molecular and physiological mechanisms. A primary function is the release of soluble substances that enhance and maintain the barrier phenotype of BMECs. Prominent instances encompass GDNF, which upregulates the transcription of TJPs; transforming growth factor-β (TGF-β), a compound that encourages endothelial quiescence and vascular integrity; Sonic hedgehog (Shh), which facilitates junctional assembly through the Patched–Smoothened signaling pathway; and angiopoietin-1, which diminishes vascular permeability by activating the Tie2 receptor (Abbott et al., 2006; Alvarez et al., 2011).

Astrocytic end-feet are enhanced in AQP4 water channels and inwardly rectifying potassium channels, allowing precise regulation of extracellular ion concentrations and

water homeostasis, particularly during neuronal activity (Amiry-Moghaddam & Ottersen, 2003).

The dysregulation of AQP4 transcription has been associated with clinical diseases, including vasogenic edema, epilepsy, and neuromyelitis optica. Astrocytes interact with Ecs at the gliovascular interface via extracellular matrix (ECM) proteins and cell adhesion molecules, establishing both physical and functional connections. These interactions facilitate TJP expression, polarize endothelial transporters, and influence pericyte positioning (Abbott et al., 2010).

Under pathological conditions, astrocytes exhibit considerable adaptability, adopting a reactive phenotype characterized by hypertrophy, proliferation, and altered gene expression (Zamanian et al., 2012). Reactive astrocytes may preserve BBB integrity by releasing anti-inflammatory cytokines, or conversely, contribute to barrier disruption through secretion of matrix metalloproteinases (MMP-2, MMP-9), nitric oxide, interleukin-6 (IL-6), and TNF-α (Argaw et al., 2012). Experimental and clinical investigations demonstrated that co-culturing Ecs with astrocytes markedly enhances TEER and reduces permeability in comparison to endothelial monocultures (Hayashi et al., 1997). This highlights the astrocytes' instructive role in BBB maturation and functional maintenance.

In conclusion, astrocytes are not merely supportive cells but active regulators of BBB physiology. Through direct contact and paracrine signaling, they modulate endothelial cell function, enhance barrier integrity, and coordinate neurovascular responses to both physiological and pathological stimuli.

2.1.1.4 Pericytes and their regulatory functions

Pericytes, or mural cells, are multifunctional cells situated inside the BM of cerebral microvessels, maintaining intimate physical and functional interactions with endothelial cells. Pericytes, as integral constituents of the NVU, are necessary for the creation, maintenance and modulation of BBB permeability. Their strategic placement between

ECs and astrocytic end-feet designates them as a crucial signaling center within the neurovascular interface.

During embryonic development, pericytes modulate EC proliferation, migration, and differentiation through platelet-derived growth factor-B/PDGFRβ signaling, which is important for their enrollment and sustenance (Armulik et al., 2010). Genetic ablation or loss of pericyte coverage during development results in immature, hyperpermeable vasculature, underscoring their importance in BBB formation (Daneman et al., 2010).

In the adult human brain, pericytes preserve barrier integrity by raising the expression of endothelial TJPs (e.g., claudin-5, OCLN), suppressing transcytosis, and modulating vascular tone. They secrete soluble mediators such as TGF-β, angiopoietin-1, and vascular endothelial growth factor (VEGF), which regulate downstream pathways including RhoA/ROCK, Notch, and Smad signaling (Bell et al., 2010; Sweeney, Ayyadurai, & Zlokovic, 2016).

Pericytes also contribute to the immune surveillance of the BBB. Under homeostatic conditions, they suppress endothelial adhesion molecule expression, thereby limiting leukocyte adhesion and transmigration. In pathological conditions including stroke, multiple sclerosis (MS), and brain tumors, pericytes may assume contractile or anti-inflammatory phenotypes, possibly resulting in impaired BBB integrity (Rustenhoven, Jansson, Smyth, & Dragunow, 2017). In reaction to inflammation or hypoxia, pericytes may disengage from the arterial wall and move into the parenchyma, where they synthesize matrix metalloproteinases (e.g., MMP-9) and chemokines that enhance vascular permeability and facilitate immune cell invasion (Göritz et al., 2011).

Beyond their barrier-regulating roles, pericytes influence angiogenesis and vascular remodeling, particularly under pathological conditions. Interactions between pericytes and endothelial tip cells in sprouting angiogenesis modulate capillary branching and vessel stabilization. In tumors, abnormal pericyte coverage contributes to vascular dysfunction, hypoxia, and impaired drug delivery (Cooke et al., 2012).

In the CNS, pericytes are estimated to encompass 30–70% of the abluminal endothelial surface, much exceeding their coverage in other organs, indicative of the brain's rigorous vascular regulatory demands (Berthiaume, Hartmann, Majesky, Bhat, & Shih, 2018). This comprehensive coverage is facilitated by specific peg-and-socket connections and gap junctions, enabling direct cytoplasmic communication between pericytes and ECs.

2.1.1.5 BM and ECM

The BM is a specialized, thick ECM that surrounds the abluminal surfaces of ECs and pericytes in the CNS microvasculature. The BM, as a structural element of the NVU, is crucial for the BBB by providing mechanical support, molecular architecture, and biochemical signals important for cellular adhesion, polarity, and survival (He et al., 2018).

Composed primarily of laminin isoforms, collagen type IV, entactin, and heparan sulfate proteoglycans, the BM forms a distinct barrier between ECs and astrocytic end-feet (Yao, Chen, Norris, & Strickland, 2014). ECs and astrocytes secrete ECM components that interact with integrin receptors (e.g., α6β1, α1β1) and dystroglycan complexes, thereby modulating cytoskeletal organization and intracellular signaling pathways (Maj S Thomsen, Routhe, & Moos, 2017).

Laminin-α4 and laminin-α5 chains are abundant in CNS microvessels and are critical for BBB development and repair. Laminins provide a scaffold for endothelial adhesion, regulate tight junction protein expression, and promote endothelial polarization (Menezes et al., 2014). Collagen type IV forms a reticular framework that enhances tensile strength and filtration capacity. At the same time, perlecan and other heparan sulfate proteoglycans modulate growth factor bioavailability (e.g., VEGF, FGF-2) and ion transportation across the BBB.

The BM functions like both a passive barrier and an active signaling interface, affecting the activity of ECs and astrocytic cells via matrix-bound signaling molecules. Such interactions regulate TJP synthesis and localization, contributing to the functional

maturation of the BBB in both physiological and pathological contexts (Tilling, Korte, Hoheisel, & Galla, 1998).

Pathological alterations of the BM are a hallmark of various neurological disorders. Upregulation of MMP-2 and MMP-9 in response to hypoxia, ischemia, or inflammation disrupts the BM, impairing endothelial–astrocyte adhesion and increasing paracellular permeability (Rosenberg, Estrada, & Dencoff, 1998). This leads to vasogenic edema, leukocyte infiltration, and dysregulated CNS immune homeostasis, as observed in MS, stroke, and GBM (Liebner, Cavallaro, & Dejana, 2006; Maj S Thomsen et al., 2017).

Studies in laminin-deficient animals have demonstrated increased BBB permeability, aberrant vascular architecture, and reduced expression of endothelial TJPs (Yao et al., 2014), underscoring the central role of BM components in BBB homeostasis and their potential as therapeutic targets in barrier-modulating strategies.

In summary, the BM is an integral molecular interface that governs BBB development, stability, and repair. Simultaneously, its constant remodeling is essential for the maintenance of physiological barriers and the pathological disruption in CNS disorders.

2.1.1.6 Adherens junctions

AJ are essential extracellular complexes that, in conjunction with TJs, preserve the structural cohesion and functional integrity of the BBB. Situated underneath the TJ complexes of BMECs, AJs facilitate intercellular adhesion, maintain endothelial polarity, and are pivotal in the dynamic control of vascular permeability.

The primary transmembrane component of AJs is vascular endothelial (VE)-cadherin, a calcium-dependent adhesion molecule specific to ECs. VE-cadherin mediates homophilic cell–cell binding and connects to the actin cytoskeleton via catenin family proteins (α-, β-, and γ-catenin) (Dejana, Tournier-Lasserve, & Weinstein, 2009). This cadherin–catenin complex not only provides mechanical stability but also serves as a platform for

intracellular signaling pathways regulating endothelial survival, proliferation, and barrier function.

The signaling pathway of Wnt/β-catenin, essential for BBB development, employs β-catenin as both a structural linker and a transcriptional co-activator (Liebner et al., 2008). Activation of Wnt signaling stabilizes β-catenin, thereby promoting the expression of TJPs like claudin-3 and ZO-1 and enhancing barrier tightness.

In addition to VE-cadherin, N-cadherin is expressed on the abluminal surface of ECs, where it facilitates heterotypic adhesion to pericytes and muscle cells within the vascular wall. N-cadherin is thought to preserve endothelial–pericyte interactions and promote bidirectional signal transduction, particularly during angiogenesis and vascular remodeling (Gerhardt & Betsholtz, 2003).

Several auxiliary adhesion molecules further contribute to BBB integrity and immune cell trafficking. Platelet EC adhesion molecule-1 (PECAM-1), localized at intercellular junctions, supports leukocyte transmigration during immune surveillance and inflammation by interacting with cytoskeletal elements and integrins (Muller, Weigl, Deng, & Phillips, 1993; M.-X. Wong et al., 2004). CD99, another junctional transmembrane protein, works in concert with PECAM-1 to mediate transcellular leukocyte migration (Lou, Alcaide, Luscinskas, & Muller, 2007). EC–selective adhesion molecule (ESAM) is abundant in the CNS and contributes to junctional integrity and paracellular resistance (Nasdala et al., 2002).

These adhesion systems respond dynamically to inflammatory mediators, shear stress, and growth factors. For example, phosphorylation of VE-cadherin by Src-family kinases triggers its internalization and AJ disassembly, leading to increased vascular permeability—a process observed in tumor angiogenesis, stroke, and MS (Dejana & Orsenigo, 2013).

Together, AJs and auxiliary adhesion molecules ensure the mechanical stability, selective permeability, and immunological regulation of the BBB. Precise regulation of these

junctional complexes is crucial in addition to vascular equilibrium, as well as for preserving CNS immune privilege.

2.1.2 Neovascular heterogeneity and pericyte dynamics

The neovasculature in GBM consists of many vessel morphologies, including standard endothelial-lined capillaries, vasculogenic mimicry channels, and glomeruloid vascular proliferations. These structures exemplify many angiogenic processes, including sprouting angiogenesis, vascular remodeling, and tumor cell-mediated vasculogenesis. Vasculogenic mimicry, specifically non-endothelial, channel-like structures created from tumor cells, has been shown to correlate with a poorer outcome as well as chemoresistance in high-grade gliomas (Sattiraju & Mintz, 2019).

Neovascular Architecture in GBM – GBM exhibits a unique and highly heterogeneous neovascular network influenced by the interaction of ECs, pericytes, and glioma stem-like cells (GSCs). This vascular variability has a profound impact on BBTB integrity and function. The neovasculature in GBM encompasses multiple vessel morphologies, including conventional endothelial-lined capillaries, vasculogenic mimicry channels, and glomeruloid vascular proliferations. These structures reflect diverse angiogenic processes, including sprouting angiogenesis, vascular remodeling, and tumor cell-mediated vasculogenesis. Vasculogenic mimicry, characterized by non-endothelial, channel-like structures formed by cancer cells, has been associated with a worse outcome and chemoresistance in high-grade gliomas (Sattiraju & Mintz, 2019).

Pericyte Heterogeneity and Function – Pericytes in GBM display marked morphological and functional diversity. They may originate from native brain mural cells or arise via transdifferentiation of GSCs, generating pericyte-like cells with tumor-promoting functions (L. Cheng et al., 2013). Pericytes express varying levels of biomarkers such as PDGFR-β, NG2, and α-SMA, and their arrangement and density directly influence vascular permeability and integrity (Armulik, Genové, & Betsholtz, 2011). Loss or disorganization of pericyte coverage, frequently observed in tumor vessels,

is associated with increased BBTB permeability and reduced vascular functionality (Winkler et al., 2004).

Glioma Stem Cell-Derived Pericytes – GSCs can differentiate into pericyte-like cells, integrating into the tumor vasculature to promote vascular stabilization and preserve barrier characteristics. Targeted breakdown of GSC-derived pericytes in vivo models has demonstrated a compromise of BBTB integrity, a rise in vascular permeability, and an enhancement in the administration and effectivity of anticancer treatments (L. Cheng et al., 2013; W. Zhou et al., 2017). These findings highlight the dual function of GSC-derived pericytes in sustaining tumor vasculature while obstructing therapeutic infiltration in perivascular niches.

Pericyte-Mediated Regulation of the Blood–Tumor Barrier – Pericytes regulate BBTB properties through multiple interconnected mechanisms such as modulating endothelial TJP expression (e.g., claudin-5, occludin), secreting signaling molecules (e.g., TGF-β, angiopoietin-1) that influence endothelial quiescence and barrier permeability, and interacting with the BM to modify ECM composition and mechanical properties (Armulik et al., 2010). These regulatory pathways collectively shape BBTB permeability and stability, representing both obstacles and potential therapeutic targets in GBM treatment.

2.2 Structural and Functional Alterations Defining the BBTB

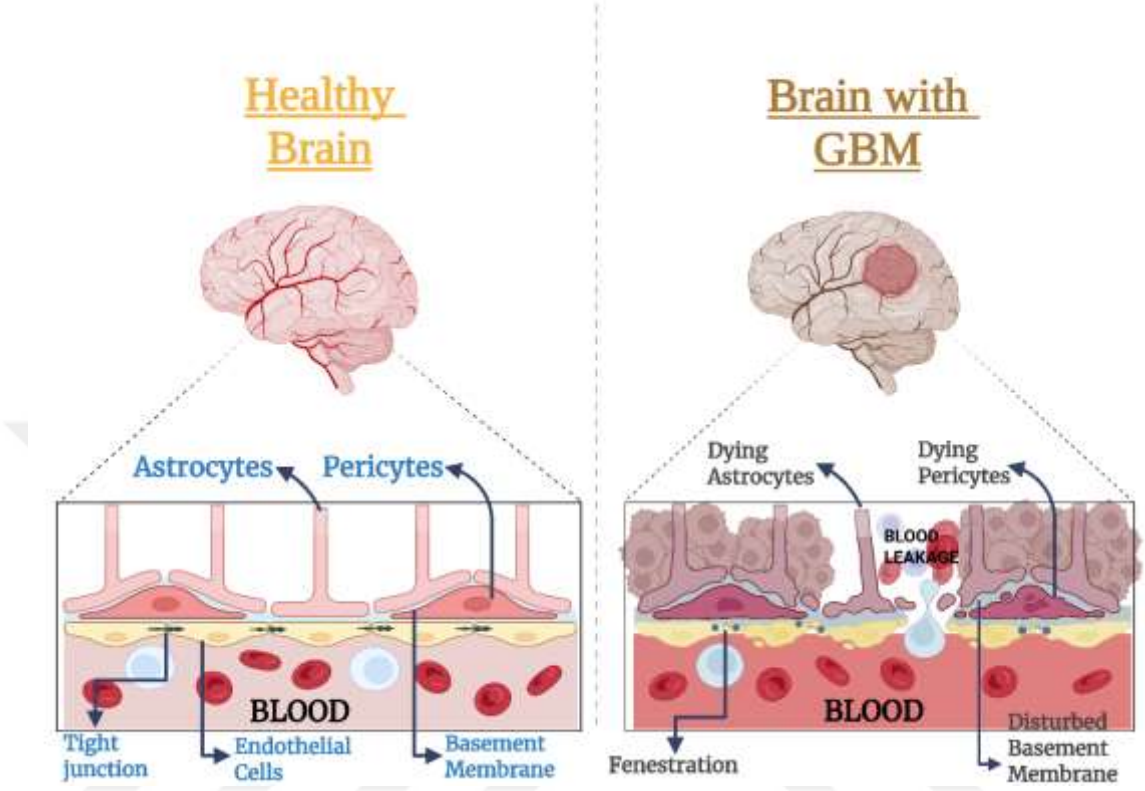

Figure 2.2 Comparison of the BBB and GBM-Affected Brains (Created by BioRender)

GBM induces substantial functional and anatomical alterations in the cerebral microvasculature, transforming the BBB into a heterogeneous and dysfunctional BBTB, as shown in Figure 2.2. Several key pathological changes characterize this transition (Huber et al., 2002).

Breakdowns of Tight Junctions and Endothelial Integrity – In a functioning brain, Ecs are linked by TJs formed by proteins like claudin-5, OCLN, and ZO-1, that govern paracellular permeability. In GBM, tumor-derived factors diminish the expression of TJPs, alter cytoskeletal anchoring, and mislocate junctional components, leading to reduced barrier integrity and increased permeability (Linville et al., 2021; Nitta et al., 2003). A reduction in claudin-5 transcription is directly associated with increased permeability of molecular weight of less than 800 Da in glioma-impacted regions.

Pericyte Coverage and Functional Impairment– Pericytes, which envelop Ecs and are critical for BBB maintenance, are reduced or structurally altered in GBM, promoting microvascular instability, increased vesicular transport, and abnormal endothelial morphology (Armulik et al., 2010). Single-cell transcriptomics have identified PTH1R+ pericyte subpopulations in GBM that remodel the BBTB by altering ECM architecture, leading to abnormal vascular morphology (Y. Li et al., 2024).

Retraction of Astrocytic End Feet – Astrocytic end feet, which ensheath nearly 90% of cerebral capillaries and express AQP4, are essential for BBB integrity. In GBM, astrocytic polarization is diminished, and AQP4 becomes diffusely distributed across the astrocyte membrane, impairing water homeostasis and promoting edema (Amiry-Moghaddam & Ottersen, 2003; Wolburg, Noell, Wolburg-Buchholz, Mack, & Fallier-Becker, 2009). This mislocalization is frequently associated with the degradation of anchoring proteins inside the perivascular basal lamina.

Basement Membrane Degradation – The BM of the BBB, composed of laminin, collagen type IV, nidogen, and heparan sulfate proteoglycans, provides structural integrity and biochemical interactions for EC and glial cells. In GBM, tumor and inflammatory cells activate matrix metalloproteinases, leading to BM degradation, which weakens structural integrity and cellular connections (Maj S Thomsen et al., 2017). This process facilitates tumor cell invasion and immune cell infiltration.

Aberrant Angiogenesis and Vascular Remodeling – GBM is a highly vascularized tumor characterized by VEGF-driven angiogenesis, producing irregular, tortuous, and highly permeable vessels. These vessels frequently display incomplete pericyte coverage and discontinuous endothelial lining, contributing to heterogeneous BBTB permeability (Jain et al., 2007; Y. Li et al., 2024). Vessels in the tumor core are highly permeable, while those at the invasive margin often retain features of an intact BBB, limiting uniform drug delivery (Quail & Joyce, 2017).

Therapeutic Delivery Implications – Contrast-enhanced MRI frequently demonstrates BBB disruption in gliomas; however, significant tumor regions, particularly at the

periphery, maintain barrier function sufficient to impede drug penetration (Arvanitis, Ferraro, & Jain, 2020). BBTB heterogeneity, combined with active efflux transporters such as ABCB1, reduces therapeutic drug accumulation in infiltrative areas. These limitations have driven the development of targeted ultrasound, nanoparticle-based approaches, and receptor-mediated transcytosis (RMT) strategies to transiently or permanently bypass the BBTB (Sarkaria et al., 2018).

2.2.1 Pathological transition to the BBTB in GBM

GBM is a rare, highly aggressive CNS neoplasm characterized by cellular heterogeneity, extensive invasiveness, and considerable compromise of BBB integrity. As malignant cells proliferate and infiltrate the surrounding brain parenchyma, the organized barrier architecture progressively evolves into the distinct BBTB.

This pathological transition entails many modifications in junctional complexes, including the downregulation or mislocalization of VE-cadherin, N-cadherin, and auxiliary adhesion molecules, resulting in abnormal endothelial-pericyte interactions and compromised barrier polarity. The BBTB has fluctuating permeability, abnormal vascular structure, and impaired selective transport, significantly influencing the tumor microvascular environment and modifying drug delivery dynamics.

Such alterations provide a considerable barrier to treatment efficacy, since the fluctuating permeability of the BBTB often results in heterogeneous drug distribution inside the tumor mass. Concurrently, these structural vulnerabilities indicate potential therapeutic pathways for treatments aimed at leveraging compromised junctional integrity to enhance targeted drug delivery in GBM.

2.2.2 Functional implications of barrier heterogeneity on therapeutic transport

The BBTB in GBM exhibits pronounced molecular heterogeneity, influencing drug distribution, accumulation, and efficacy. This variability arises from dysregulated

angiogenesis and atypical perivascular architecture, creating both obstacles and opportunities for targeted drug delivery.

While the GBM core often contains leaky, immature vasculature with increased transcytosis and reduced TJ integrity, the infiltrative tumor margins typically retain intact barrier properties. As a result, drug penetration is uneven: core regions allow partial influx, whereas infiltrative zones remain poorly accessible, fostering treatment-resistant cell populations (Sarkaria et al., 2018; Song, Hu, Fu, & Gao, 2022).

Mass spectrometry imaging (Qmsi) and cerebral microdialysis have shown that even in areas with BBTB disruption, drug concentrations often remain subtherapeutic due to rapid efflux, elevated interstitial fluid pressure, and limited convection (Luptáková et al., 2021). Efflux transporters such as ABCB1 and ABCG2 remain active in both disrupted and intact BTB regions, further limiting intracellular drug accumulation (Wilkins et al., 2024). These pharmacokinetic barriers contribute to selection pressures that favor more aggressive, therapy-resistant tumor clones, especially within poorly perfused regions.

Advances in quantitative neuropharmacokinetic imaging, including MALDI-Qmsi, now allow high-resolution mapping of unbound drug distribution within brain tissue, enabling precise correlation between drug exposure and therapeutic efficacy. Such tools are critical for developing adaptive treatment strategies tailored to the heterogeneous tumor microenvironment.

Promising approaches to address BBTB heterogeneity include such as targeted, localized disruption (e.g., focused ultrasound) in resistant tumor regions, dual-ligand NPs designed to target both leaky and intact BBTB vasculature (Cuitian et al., 2017), and cell-penetrating peptides and Trojan horse delivery systems to enhance transport across intact BBTB areas (Choudhari et al., 2021).

These strategies aim to achieve uniform drug distribution across heterogeneous tumor regions, potentially improving treatment response and patient outcomes.

2.2.3 Clinical implications of BBTB heterogeneity for drug delivery

The variability of the BBTB in GBM poses a considerable challenge to efficient medication administration. While conventional imaging modalities such as contrast-enhanced MRI reveal widespread BBB disruption in gliomas, histological and pharmacokinetic studies demonstrate that substantial tumor regions retain barrier-like properties, limiting therapeutic uptake (Arvanitis et al., 2020; Sarkaria et al., 2018).

GBM displays a marked regional gradient in BBTB permeability: the tumor core typically exhibits highly permeable vasculature, whereas the invasive margin maintains relatively intact barrier characteristics (Jain et al., 2007; Quail & Joyce, 2017). This spatial variability is affected by multiple factors, including the degree of angiogenic remodeling driven by hypoxia and VEGF expression, the distribution and differentiation state of GSCs, the presence or absence of functional pericyte coverage, and differences in inflammatory activity and ECM organization (Y. Li et al., 2024; W. Zhou et al., 2017).

Consequently, therapeutic agents often preferentially accumulate in vascularized core regions, leaving infiltrating cells at the periphery relatively unaffected. Unlike peripheral solid tumors, which frequently benefit from the enhanced permeability and retention (EPR) effect, gliomas do not uniformly exhibit this phenomenon due to the persistence of intact BBB segments. The absence of fenestrated endothelium, combined with high activity of efflux transporters such as ABCB1 and ABCG2, further limits transvascular transport and reduces the efficacy of otherwise potent agents (Löscher & Potschka, 2005a; W. Zhou et al., 2017).

Physical and Physiological Barriers: Beyond structural limitations, GBM is associated with elevated interstitial fluid pressure (IFP) and abnormal vascular architecture, both of which impede convective transport and hinder drug penetration across the BBTB. Tumor-associated vasogenic edema, exacerbated by dysregulated AQP4 expression, further compromises drug delivery in affected areas (Wolburg et al., 2009). These physiological barriers result in subtherapeutic concentrations of chemotherapeutics in BBTB-protected zones, promoting drug resistance and tumor recurrence.

Therapeutic Approaches and Strategies: Addressing BBTB heterogeneity is a central goal in GBM therapy development. Investigational strategies include such as focused ultrasound (FUS) utilizing microbubbles to temporarily breach the BBTB and improve medication penetration (Hynynen & McDannold, 2004), NP-based delivery systems engineered for RMT via targets such as transferrin or insulin receptors (Saraiva et al., 2016), modulation of endothelial–pericyte signaling, including inhibition of PDGFR-β, to reduce barrier integrity (W. Zhou et al., 2017), and BBB-penetrant prodrugs or carrier-modified molecules (e.g., lipophilic analogs) with improved pharmacokinetic properties.

In parallel, advanced in vitro BBB and BBTB models are increasingly used to evaluate and optimize these strategies before moving into clinical testing (Linville et al., 2021).

2.2.4 Therapeutic strategies targeting the BBTB

Various therapeutic methodologies have been developed to either modulate the BBTB to enhance drug delivery or to entirely circumvent its restrictive properties. These strategies encompass mechanical disruption techniques as well as molecular and cellular targeting approaches.

Physical Disruption of the BBTB – FUS paired with intravenous microbubbles can physically break endothelial junctions and temporarily breach the BBTB. This method has shown potential in preclinical and early-phase clinical trials by enhancing the delivery of chemotherapeutics such as doxorubicin and temozolomide to glioma tissue (Hynynen & McDannold, 2004). The effect is temporary and spatially localized, which helps minimize systemic toxicity.

Nanoparticle-Mediated Delivery Systems – NPs facilitate the delivery of therapeutic agents across the BBTB via RMT (e.g., transferrin or low-density lipoprotein receptors), cell-penetrating peptides utilizing adsorptive-mediated endocytosis, and stimulus-responsive systems that release cargo in acidic pH conditions or respond to tumor-specific enzymatic activity (Saraiva et al., 2016). Lipid-based nanoparticles, polymeric micelles,

and metal-organic NPs have been designed to enhance BBB penetration, prolong systemic circulation duration, and minimize off-target toxicity (Shilo et al., 2015).

Molecular Targeting of BTB Components – Another approach involves modulating molecular pathways that preserve BBTB integrity. Inhibition of VEGF or PDGF signaling can destabilize pericytes, leading to increased BBTB permeability (Winkler et al., 2004). Targeting GSC-derived pericytes, essential for vascular integrity, has demonstrated the capacity to sensitize tumors to chemotherapy (W. Zhou et al., 2017). Furthermore, inhibition of efflux pumps such as ABCB1 and ABCG2 with agents like elacridar has enhanced drug accumulation in tumor tissue (Löscher & Potschka, 2005).

Gene and Cell Therapies – Emerging strategies include the use of genetically engineered stem cells, such as neural progenitor cells, which can home to tumor sites and deliver therapeutic agents (Aboody, Najbauer, & Danks, 2008). These cells can be designed to produce cytokines, pro-apoptotic proteins, or NP-encapsulated drugs directly at the BBTB interface. In addition, viral vectors such as adeno-associated virus (AAV) and lentivirus are being developed for BBTB-penetrant gene therapies, often in combination with pharmacological or physical BBTB modulation to improve delivery to infiltrative glioma cells (Naeem et al., 2022).

2.3 NP Transport Mechanisms Across the Brain Endothelium

The BBB is a tightly regulated endothelial interface characterized by TJs, minimal transcytosis, and active efflux systems, which collectively hinder the passage of therapeutic agents to the CNS. NPs can be engineered to exploit multiple transport routes across BMECs, with their efficiency determined by both biological and physicochemical factors.

2.3.1 Paracellular and transcellular routes of nanomaterial translocation

Under physiological conditions, TJs—mainly claudin-5, OCLN, and JAMs—effectively restrict paracellular transport. Consequently, NP movement between Ecs is negligible unless junctions are pathologically disrupted or experimentally modulated (Abbott et al., 2010; Gonzalez-Carter et al., 2020).

Transcellular transport is the primary route for NP passage across the BBB, involving clathrin- and caveolae-mediated endocytosis for vesicle-based uptake, macropinocytosis for larger vesicular internalization, and vesicular diffusion for ultrasmall (<5 nm) NPs, enabling direct cytoplasmic passage (Radka Gromnicova et al., 2016).

Multiple pathways may be operating simultaneously, influenced by NP dimensions, coatings, and local endothelial conditions (Fatima, Gromnicova, Loughlin, Sharrack, & Male, 2020).

2.3.2 Active vs. passive strategies for barrier penetration

The comparison between active and passive transport is shown in Table 2.1.

Passive transport relies on physicochemical compatibility with endothelial membranes or localized TJ loosening (e.g., in BBTB regions of GBM). Small (<20 nm), hydrophobic or neutrally charged NPs may diffuse more readily in compromised barrier areas. However, passive diffusion lacks targeting specificity and results in poor penetration into intact BBB regions.

Active transport exploits ligand-receptor interactions on the luminal endothelial surface, such as transferrin, LDLR, or insulin receptors, to initiate RMT (Gonzalez-Carter et al., 2020; Li et al., 2017). Targeting moieties include peptides, antibodies, or endogenous ligands, and biomimetic coatings can further enhance specificity (H. Chen et al., 2024). While active methods improve selectivity, they face limitations such as receptor

saturation, immunogenicity, and endosomal entrapment (Nowak, Brown, Graham, Helgeson, & Mitragotri, 2020).

Table 2.1 Comparative overview of passive and active nanoparticle transport mechanisms

Transport Mechanism	Mechanism Description	Key Parameters	Advantages	Limitations	Representative Examples	References
Passive Transport	Depends on physicochemical compatibility with endothelial membranes or localized relaxing of tight junctions, as shown in the BBTB sections of GBM.	NP size <20 nm, hydrophobic or neutral surface charge.	Basic mechanism; no requirement for functionalization; improved permeability in compromised barrier areas.	Insufficient targeting specificity; inadequate penetration of the entire BBB; unregulated biodistribution.	Diffusion of small hydrophobic NPs in GBM-associated BBTB.	(Cornelissen et al., 2023; D. Wu et al., 2023)
Active Transport	Utilizes ligand-receptor interactions on luminal endothelial surfaces to initiate RMT.	Targeting ligands include peptides, antibodies, and endogenous ligands; endothelial receptors consist of transferrin, LDLR, and the insulin receptor.	Higher selectivity can cross intact BBB; improved targeting with biomimetic coatings.	Receptor saturation; immunogenicity; endosomal entrapment; requires ligand design and optimization.	Transferrin-conjugated NPs, LDLR-targeted liposomes, insulin-receptor-targeted nanocarriers.	(H. Chen et al., 2024; Gonzalez-Carter et al., 2020)

2.3.3 Hybrid and stimuli-responsive strategies

Hybrid designs combine passive diffusion properties with active targeting ligands to maximize efficiency. Stimuli-responsive carriers—triggered by internal cues (pH, redox potential) or external inputs (light, ultrasound) —enable spatiotemporal control over NP

release (H. Gao, 2016). Such systems are especially valuable for heterogeneous barriers like the BBTB, where regions of intact and disrupted vasculature coexist.

2.3.4 Influence of physicochemical properties on endothelial interaction

The NP-BBB interaction is shaped by size, morphology, charge, and surface chemistry:

Size: <20 nm improves diffusion and transcytosis but risks rapid clearance; 20–80 nm is generally optimal for RMT; >100 nm reduces permeability due to steric hindrance (H. Chen et al., 2024; Hoshyar, Gray, Han, & Bao, 2016).

Shape: Rod-like or filamentous NPs can enhance vascular wall interactions and prolong circulation compared to their spherical counterparts (Kolhar et al., 2013).

Charge: Cationic surfaces increase adsorptive transcytosis but raise cytotoxicity; neutral or slightly negative charges improve biocompatibility and systemic stability (Alyautdin, Khalin, Nafeeza, Haron, & Kuznetsov, 2014; Barbu, Molnàr, Tsibouklis, & Górecki, 2009).

Surface chemistry: PEGylation reduces opsonization and prolongs circulation; biomimetic coatings (e.g., endothelial or leukocyte membranes) facilitate immune evasion while preserving targeting ability (H. Chen et al., 2024; Hu & Zhang, 2012).

Optimizing these parameters requires balancing stability, targeting specificity, and transport efficiency, with design choices tailored to the state of the barrier—e.g., exploiting larger, more cationic carriers in compromised BBTB regions while using stealthy, ligand-targeted systems for intact BBB zones.

2.4 Photoresponsive Nanotherapeutics For BBTB

Recent advancements in nanomedicine have created intriguing opportunities for the therapeutic management of GBM. Photoresponsive nanotherapeutics, which are nanocarriers engineered to react to certain light wavelengths, enable precise spatial and temporal regulation of therapeutic interventions. Unlike traditional chemotherapy or radiation, PTT and PDT provide targeted lethal effects within the tumors while reducing exposure to the entire system (Chakroun et al., 2018; Hsu et al., 2021). However, their efficacy is hindered by the brain's protective physiological barriers, including the BBB and the BBTB.

To overcome these problems, researchers have demonstrated stimuli-responsive NPs capable of penetrating the BBB/BBTB and generating ROS or localized hyperthermia with NIR light. For example, biomimetic proteolipid NPs such as BLIPO-ICG, loaded with FDA-approved indocyanine green, demonstrated efficient BBB penetration and glioma-specific accumulation, enabling fluorescence-guided surgery and >90% tumor growth inhibition without damaging healthy tissue (Jia et al., 2018).

Albumin-based theranostic systems using catalase and gold nanorods facilitated multimodal imaging (fluorescence, photoacoustic, and thermal) and improved phototherapy by alleviating tumor hypoxia via in situ oxygen generation (Yang et al., 2020).

2.4.1 Fundamentals of PTT and PDT mechanisms

PDT involves a PS activated by light in the visible or NIR spectrum. Upon illumination, the PS transitions to an excited state, transferring energy to molecular oxygen to generate ROS, predominantly singlet oxygen ($^1O_2$) (Figure 2.3). Due to their short diffusion radius (<50 nm), ROS require precise subcellular localization—commonly within mitochondria, lysosomes, or the endoplasmic reticulum—to induce apoptosis, autophagy, or necrosis (Hou et al., 2020; Overchuk, Weersink, Wilson, & Zheng, 2023).

PTT, on the other hand, converts NIR light (650–950 nm) into heat using photothermal agents such as gold nanorods, carbon nanomaterials, or semiconducting polymers. Temperatures above ~43 °C disrupt cellular structures, while >55 °C often cause coagulative necrosis. Sub-lethal heating can also sensitize tumor cells to other treatments by modifying heat shock proteins, vascular permeability, and oxidative stress responses (H. S. Han & Choi, 2021; Overchuk et al., 2023).

Nanocarriers enhance both PDT and PTT by improving PS solubility, stability, and tumor targeting. Lipid-based and biomimetic NPs have demonstrated BBB penetration and glioma-specific delivery (Chakroun et al., 2018; Jia et al., 2018). PTT agents, including gold nanoshells, Prussian blue NPs, and hollow gold nanospheres (HauNSs), have elevated photothermal conversion effectiveness and can be modified for imaging-guided treatment (Hou et al., 2020; Melancon, Zhou, & Li, 2011).

Combining PDT and PTT in a single nanoplatform yields synergistic effects: PDT triggers immunogenic cell death (ICD) and promotes dendritic and T-cell activation, while PTT increases antigen release and improves oxygenation, enhancing PDT efficacy (Overchuk et al., 2023; Yang et al., 2020). This dual-modality strategy mitigates PDT's reliance on oxygen while preserving potent tumoricidal efficacy.

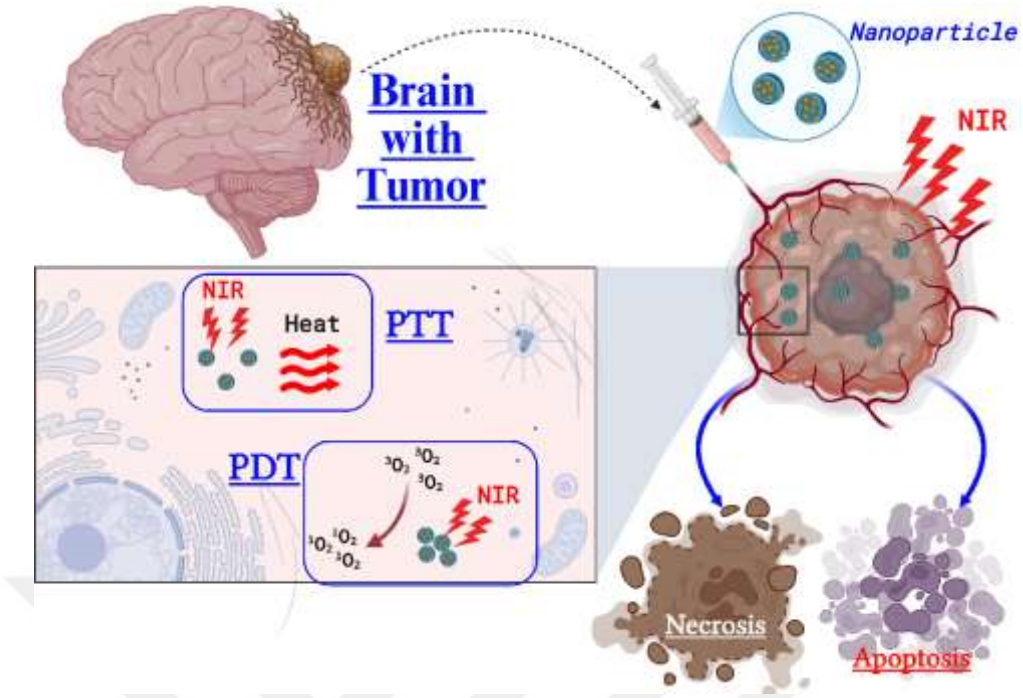

Figure 2.3 Representation of NP-mediated photothermal PTT and photodynamic PDT therapy in GBM (Created in BioRender)

2.4.2 Design criteria for light-activatable NPs in CNS applications

2.4.2.1 Optical properties and photothermal conversion efficiency

Light-activatable NPs should absorb strongly in the NIR "biological window" (650–950 nm) for optimal tissue penetration. Materials such as gold nanoshells, copper sulfide (CuS) NPs, and semiconducting polymers display high photothermal conversion efficiency (L.-J. Chen et al., 2016; X. Cheng et al., 2017; Hiremath et al., 2022; Overchuk et al., 2023). CuS nanoparticle (<15 nm) also allows renal clearance, reducing long-term toxicity (L.-J. Chen et al., 2016).

2.4.2.2 Size and surface characteristics for BBB penetration

For effective brain delivery, NPs should generally be <100 nm and have mildly cationic or near-neutral zeta potential to balance endothelial interaction and serum stability (T. Liu et al., 2023). PEGylation minimizes protein corona formation and prolongs

circulation. RMT using ligands such as transferrin or angiopep-2 enhances BBB penetration (Sun et al., 2023).

2.4.2.3 Responsiveness to stimuli and controlled release

Incorporating photo-cleavable linkers (e.g., azobenzene) or thermosensitive polymers enables light-triggered release. For example, platinum-based nanocomplexes can release cytotoxic Pt^{2+} in a spatially and temporally controlled manner upon NIR exposure, combining PTT and chemotherapy (H. Zhao et al., 2019).

2.4.2.4 Tumor targeting and biomimicry

Biomimetic coatings derived from cancer cell membranes or exosomes preserve adhesion molecules that interact with tumor endothelium or glioma cells, improving targeting efficiency (Z. Chen et al., 2016; Jiang et al., 2024).

2.4.2.5 Clearance and biodegradability

Biodegradable carriers such as polypyrrole and PLGA-based NPs maintain photothermal activity while enabling safe metabolic elimination (M. Wang, 2016). Ultrasmall CuS NPs (<6 nm) are rapidly excreted via renal clearance, reducing systemic accumulation (Overchuk et al., 2023).

2.4.2.6 Theranostic integration

Modern nanoplatforms integrate therapeutic and imaging modalities, enabling MRI, PET, PA, or fluorescence-guided therapy. For instance, gold nanoshells combined with superparamagnetic iron oxide allow simultaneous MRI tracking and photothermal ablation (Kim, Piao, & Hyeon, 2009)

Table 2.2 Summary of design criteria and representative examples of light-activatable nanoparticles for CNS applications

Criteria	Description	Examples / Materials	References
Optical Properties and Photothermal Efficiency	Significant absorption occurs within the 650–950 nm range, facilitating optimal penetration to tissues; high photothermal conversion efficiency.	Gold nanoshells, CuS NPs (<15 nm, renal clearance), semiconducting polymers.	(L.-J. Chen et al., 2016; X. Cheng et al., 2017) (Hiremath et al., 2022; Overchuk et al., 2023)
Size and Surface Characteristics for BBB Penetration	<100 nm; mildly cationic or near-neutral zeta potential for balance between endothelial interaction and serum stability; PEGylation for prolonged circulation; ligand-based RMT for enhanced BBB penetration.	Transferrin, angiopep-2 functionalization.	(T. Liu et al., 2023; Sun et al., 2023)
Responsiveness to Stimuli and Controlled Release	Photo-cleavable linkers or thermosensitive polymers enable light-triggered release; a combination of PTT and chemotherapy is possible.	Azobenzene linkers; Pt-based nanocomplexes releasing Pt^{2+} under NIR.	(H. Zhao et al., 2019)
Tumor Targeting and Biomimicry	Biomimetic coatings preserve adhesion molecules, improving targeting of tumor endothelium or glioma cells.	Cancer cell membrane-coated NPs, exosome coatings.	(Z. Chen et al., 2016; Jiang et al., 2024)
Clearance and Biodegradability	Use of biodegradable carriers for safe elimination; ultrasmall NPs for renal clearance to reduce systemic accumulation.	Polypyrrole NPs, PLGA NPs, CuS NPs (<6 nm).	(Overchuk et al., 2023; M. Wang, 2016)
Theranostic Integration	A combination of therapeutic and imaging modalities for guided therapy and monitoring.	Gold nanoshells + SPIONs for MRI + PTT.	(Kim et al., 2009)

2.4.3 Synergistic integration of PTT and PDT in nanomedicine platforms

Integrating PTT and PDT into a single nanoplatform represents a highly effective strategy to enhance therapeutic efficacy and address the limitations inherent to each treatment modality. PTT utilizes NIR light to induce localized hyperthermia, causing protein denaturation and membrane disruption, while PDT employs light-activated PSs to generate ROS, particularly singlet oxygen ($^1O_2$), which induces apoptosis and necrosis (Chakroun et al., 2018; Yang et al., 2020).

Despite their advantages, both approaches face inherent obstacles: PTT can be limited by uneven heat distribution and the risk of collateral damage at high temperatures (H. Zhao et al., 2019), whereas PDT is hindered by tumor hypoxia and insufficient PS accumulation (Hou et al., 2020). When applied concurrently, PTT and PDT can overcome these limitations through complementary mechanisms. PTT-induced hyperthermia enhances tumor blood perfusion, improving oxygen availability and increasing ROS production during PDT. Conversely, ROS produced by PDT can inhibit heat shock proteins (HSPs), making cancer cells more susceptible to thermal damage from PTT (B. Zhao et al., 2024; Zonglang Zhou et al., 2021).

Recent nanotechnology platforms demonstrate the effectiveness of this synergy. Zhou et al. developed Bi-Ag@PVP NPs enabling concurrent computed tomography (CT) and photoacoustic imaging alongside PTT/PDT via a single 808 nm NIR laser. These NPs exhibited significant ROS generation and photothermal conversion, resulting in enhanced tumor ablation in vitro and in vivo (Shao et al., 2020). Similarly, Choi et al. synthesized pheophorbide-conjugated gold nanorods with glutathione-sensitive linkages for targeted delivery and controlled release, achieving over 95% cancer cell death through combined PTT and PDT with dual-wavelength irradiation (Choi & Kim, 2020).

H. Zhao et al. developed the platinum nanocomplex, which selectively released cytotoxic Pt^{2+} ions upon NIR light activation, providing a dual photothermal-chemotherapeutic effect. This system exhibited prolonged ROS generation and improved tumor selectivity under localized irradiation (H. Zhao et al., 2019).

In addition, two-dimensional (2D) nanomaterials such as molybdenum disulfide (MoS_2) and black phosphorus have gained attention for PTT/PDT integration due to their large surface area, intrinsic NIR absorption, and ease of functionalization. Hiremath et al. (2022) highlighted their ability to co-load both heat-generating agents and PSs, allowing simultaneous co-delivery and spatiotemporal activation with a single optical stimulus(Hiremath et al., 2022).

Overall, synergistic PTT/PDT nanoplatforms combine ROS production, hyperthermia, oxygen modulation, and improved delivery kinetics to enhance therapeutic outcomes while minimizing systemic toxicity. Nevertheless, challenges remain in achieving sufficient light penetration for deep-seated tumors, ensuring NP biodegradability, and precisely controlling dual-function activation. Addressing these factors will be essential for successful clinical translation in neuro-oncology.

2.5 In Vitro Modeling of the BBTB for Nanomaterial Evaluation

The creation of dependable in vitro models that mimic the architecture and functionality of the BBTB is crucial for sophisticated nanotherapeutic approaches aimed at malignant brain tumors like GBM. The healthy BBB is a precisely regulated interface composed of BMECs, pericytes, astrocytes, and a BM, which together uphold CNS homeostasis and limit the entry of xenobiotics (Tang, Rich, & Chen, 2021). In pathological conditions such as high-grade gliomas, the BBB undergoes spatially heterogeneous disruption and transformation into the BBTB, characterized by aberrant angiogenesis, impaired TJs, pericyte loss, astrocytic detachment, and altered transporter function (Ozcelikkale, Moon, Linnes, & Han, 2017; Tréhin et al., 2006).

While in vivo models are crucial for translational studies, they are constrained by interspecies variability, ethical considerations, and insufficient scalability for imaging (Cecchelli et al., 2007; Tricinci et al., 2020). Conventional 2D monoculture or co-culture systems with Transwell inserts are commonly used due to their simplicity and adherence to TEER and paracellular tracer evaluations. Nonetheless, these models sometimes

demonstrate shortcomings in the anatomical and kinetic properties of the in vivo NVU (S. W. L. Lee et al., 2020).

Recent advancements in three-dimensional (3D) models, including spheroids, hydrogel-based constructs, and microfluidic organ-on-chip platforms, have enabled a more accurate simulation of the BBTB microenvironment by integrating vascular perfusion, shear stress, ECM composition, and multicellular architecture (Barciszewska et al., 2024; Tang et al., 2021; Tricinci et al., 2020). Marino et al. developed a biohybrid, full-scale 3D model of the BBB featuring perfusable microchannels lined with endothelial and astrocytic components, demonstrating selective permeability and TEER values comparable to in vivo conditions (Marino et al., 2018). Lee et al. created a 3D in vitro model of the BBB using Ecs that human- derived, inside a collagen hydrogel scaffold, demonstrating NP transport patterns that closely corresponded with in vivo distribution in mice brains (S. W. L. Lee et al., 2020).

These biomimetic in vitro BBTB systems serve as valuable tools for assessing NPs in brain tumor contexts, particularly for light-activated platforms that need precise spatiotemporal dispersion across complex vascular interfaces. As our understanding of tumor-vasculature interactions evolves, the intricacy and therapeutic relevance of these models will likewise advance.

2.5.1 Static monoculture vs multicellular co-culture systems

Static culture models of the BBB, commonly developed using Transwell® devices, have historically functioned as crucial instruments for investigating endothelial permeability, drug transport, and barrier integrity. Conventional monoculture models utilize BMECs cultivated on the top membrane insert, providing a straightforward and economical method for high-throughput screening. Nevertheless, these models exhibit insufficient cellular complexity and physiological significance of the NVU, leading to considerable limitations, including low TEER, underexpression of TJPs, and reduced transporter function (Cardoso, Brites, & Brito, 2010; Helms et al., 2016).

Co-culture and multicellular BBB models have been created to overcome these constraints. These systems incorporate astrocytes, pericytes, microglia, and neurons in either contact or non-contact arrangements. Their incorporation markedly improves the expression of TJ markers, P-glycoprotein activity, and overall barrier integrity (Marino et al., 2018; Park et al., 2023). Co-culturing mouse endothelial bEnd.3 cells with C8-D1A astrocytes on a Transwell insert elevated TEER values and decreased FITC-dextran permeability relative to monoculture conditions, therefore emulating the limiting paracellular transport seen in vivo (Park et al., 2023).

Moreover, triple culture techniques enhance the integrity of the BBB. The inclusion of pericytes has shown an improvement in TEER and a decrease in permeability in brain models. Notably, Cecchelli et al. demonstrated that the same effects are shown regardless of species origin, although syngeneic models are recommended to minimize interspecies variability (Cecchelli et al., 2007). The synergistic engagement of astrocytes and pericytes augments transporter expression (e.g., BCRP and GLUT-1), promotes TJ assembly, and diminishes transferrin receptor levels, thereby highlighting their role in the maturation of the NVU (Al Ahmad, Gassmann, & Ogunshola, 2009; S. Liu, Agalliu, Yu, & Fisher, 2012).

Notwithstanding these advancements, static models intrinsically lack dynamic indicators like shear stress, constraining their capacity to accurately simulate the in vivo BBB environment. Co-culture models continue to serve as excellent platforms for evaluating NP permeability, performing neurotoxicity assessments, and exploring processes related to disease pathogenesis (Garberg et al., 2005; Sweeney, Zhao, Montagne, Nelson, & Zlokovic, 2018). Co-culture systems, unlike monocultures, produce more physiologically relevant data and improved predictive ability, underscoring their importance in preclinical research.

2.5.2 Transwell models as a framework for the BBB and BBTB

The Transwell® system is an established approach for in vitro modeling of the BBB and BBTB, due to its adaptability, economic efficiency, and suitability for permeability and

transport assessments. The Transwell device, originally developed to assess bidirectional solute transport across epithelial and endothelial monolayers, has been modified to allow more complex multicellular models of the NVU (Appelt-Menzel et al., 2017; Helms et al., 2016).

A porous membrane made of polyester or polycarbonate, with pore dimensions between 0.4 and 3 μm, is generally positioned between two chambers, facilitating the separate culture of BMECs on the apical (luminal) side and supporting cells on the basolateral (abluminal) side (Hatherell, Couraud, Romero, Weksler, & Pilkington, 2011). This vertical separation enables the analysis of polarized cellular activity, directional transport, and paracrine communication across cell types—an essential advantage for BBB/BBTB studies. Additionally, it enables real-time evaluation of barrier integrity by TEER and paracellular permeability assays utilizing tracers as sodium fluorescein or FITC-dextran (Kadry & Cucullo, 2023; Prabhakarpandian et al., 2013; Sood, Kumar, Dev, Gupta, & Han, 2022).

Recent developments have improved the authenticity of Transwell-based modeling. For instance, co-cultures of human iPSC-derived BMECs with primary astrocytes and pericytes produced TEER values exceeding 1500 $\Omega \cdot cm^2$, alongside heightened expression of TJPs (claudin-5, ZO-1) and efflux transporters (BCRP), thereby emulating in vivo-like barrier restrictiveness (Neal et al., 2019). Additionally, the modeling of BBTB heterogeneity has been enhanced by including glioma spheroids in the lower chamber or by exposing the endothelial layer to tumor-conditioned fluid. These alterations have successfully duplicated regionally varied permeability patterns and altered the expression profiles of barrier-related markers (Morris, Daignault-Mill, Stehbens, Genovesi, & Lagendijk, 2023; Steeg, 2021; Tang et al., 2021; Tréhin et al., 2006).

Despite its advantages, the Transwell model lacks dynamic flow and shear stress, both of which are essential for endothelial function in vivo. Shear stress affects cytoskeletal structure, transporter positioning, and inflammatory responses, all of which govern the barrier integrity of the BBB (Sweeney et al., 2018). Transwell models are crucial for the

sophisticated evaluation of NP transport and phototherapy responses, particularly when integrated with fluorescence microscopy, live-death assay, and quantitative fluorescence assays (Darrigues et al., 2020; J. Li et al., 2023).

Recent investigations have utilized Transwell devices to simulate NP-mediated PTT and PDT under polarized barrier conditions. These arrangements enable targeted laser irradiation of the apical compartment while monitoring NP diffusion and therapeutic effectiveness in the basolateral chamber, precisely simulating clinical drug delivery pathways to the brain (Chu et al., 2022; X. Huang et al., 2019; Overchuk et al., 2023).

2.5.3 Electrophysiological and permeability assessments for barrier validation

The integrity and functional efficiency of BBB and BBTB models are often evaluated by two complementary methodologies: electrophysiological measurements and permeability assays. The data from those experiments provides statistical insights into paracellular tightness, transcellular transport patterns, and the effectiveness of barrier repair or disruption in response to various stimuli, including therapies.

2.5.3.1 TEER assessments

TEER is a noninvasive, unlabeled technique that quantifies the ionic resistance of a cellular monolayer cultivated on a porous membrane. It serves as a direct indicator of TJ integrity and barrier permeability. In Transwell models, TEER is often measured using electrode-based instruments such as the EVOM3 (World Precision Instruments), which use a pair of chopsticks or planar electrodes to provide a low-voltage alternating current across the monolayer (Raut, Chen, Hori, & Kaji, 2021; Schimetz et al., 2024; Srinivasan et al., 2015). Values are expressed in $\Omega \cdot cm^2$ after normalization for the membrane area. Monoculture models often exhibit TEER values below 200 $\Omega \cdot cm^2$, but co-culture systems that include astrocytes and/or pericytes can surpass 1000 $\Omega \cdot cm^2$, hence providing a more precise representation of in vivo barrier function (Park et al., 2023; Maj Schneider Thomsen et al., 2021).

In microfluidic and organ-on-chip systems, the measurement of TEER is hindered by constrained geometries and the necessity for integrated microelectrodes. Innovations such as gold or platinum interdigitated electrodes incorporated into chip channels have facilitated the real-time, dynamic evaluation of barrier properties under flow circumstances (Gomez, Yarmey, Mane, & San-Miguel, 2025; van der Helm et al., 2016). Although currently less standardized than Transwell-based TEER measurements, these methodologies are becoming recognized for their high-fidelity barrier modeling capabilities.

2.5.3.2 Paracellular permeability evaluations

FITC–dextran, sodium fluorescein, and lucifer yellow are frequently utilized, demonstrating molecular weights from 376 Da to 70 kDa, contingent upon the imaging (Cecchelli et al., 2007; Hoffmann et al., 2011). The apparent permeability coefficient is calculated utilizing Fick's first law of diffusion. Recent improvements involve the use of electroactive markers in place of fluorescent dyes, allowing for integration with miniature biosensors and enabling continuous monitoring by chronoamperometry, or cyclic voltammetry. These electrochemical techniques have been validated against traditional fluorescence-based assays and offer advantages in throughput, signal stability, and real-time kinetic analysis (Godyń et al., 2020; Neumann, Tönsing, Kakorin, Budde, & Frey, 1998; J. F. Wong, Mohan, Young, & Simmons, 2020).

2.5.3.3 Consolidated utilization and functional analysis

The concurrent use of TEER and permeability assays provides a comprehensive assessment of barrier integrity. TEER evaluates changes in ionic conductance and the formation of TJs, whereas permeability assays determine the barrier's selectivity for specific solutes or nanoparticles. A barrier may exhibit increased TEER while still allowing the passage of large or lipophilic molecules, indicating compromised transporter or endocytic regulation. A little reduction in TEER without increased permeability may suggest tight junction reorganization rather than complete disruption (Schimetz et al., 2024; Srinivasan et al., 2015).

Moreover, these assays serve as validation tools in the study of NP transport and phototherapy. Photoinduced barrier breakdown and NP-assisted permeabilization may be objectively assessed using these endpoints, enabling precise dose-response characterization and toxicity evaluation (Palma-Florez et al., 2023; Shinde, Revi, Murugappan, Singh, & Rengan, 2022).

2.6 Assessment of Cytotoxicity and Functional Responses in Phototherapy Research

Assessing the cytotoxic and functional responses of GBM to phototherapy is essential for ascertaining the therapeutic potential of nanomaterials and improving their efficacy. In vitro cytotoxicity studies assess both direct toxicity from NPs and photo-induced effects, including mitochondrial malfunction, ROS production, and apoptosis.

The predominant viability assays are MTT, AlamarBlue®, and lactate dehydrogenase (LDH) release tests. AlamarBlue assays rely on mitochondrial metabolic activity and are widely utilized to evaluate cytotoxic effects of NP exposure across different durations and concentrations. Kolter et al. revealed that PS80-coated PBCA NPs at concentrations of 500 μg/mL or higher resulted in a substantial decrease in the activity of metabolism after 6 hours and practically total cytotoxicity after 24 hours, whereas lower doses displayed time-dependent effects without immediate toxicity (Kolter, Ott, Hauer, Reimold, & Fricker, 2015). LDH assays further validated this, indicating significant cell membrane impairment at increased concentrations (Eder et al., 2022).

Advanced models employing real-time imaging approaches, such as the Incucyte platform, have enabled the dynamic assessment of target cell death inside BBB-integrated systems. Huang et al. utilized Incucyte to assess CAR-T cell-mediated cytotoxicity across the BBB in GBM models, offering an advanced method to measure functional post-transmigration efficacy over 48 hours (J. Huang et al., 2022).

Moreover, phototoxicity can vary significantly between normoxic and hypoxic conditions. Shamjith et al. highlighted this problem by comparing the effects of PDT in normoxic and hypoxic environments, demonstrating reduced ROS generation and

phototoxicity under low oxygen circumstances, hence emphasizing the need for tumor microenvironment simulation in evaluating phototherapies (Shamjith et al., 2024).

2.6.1 Summary of conventional in vitro toxicological assays for NPs

Evaluating NP toxicity in vitro is essential for determining their biosafety before clinical use, especially in phototherapy. These tests often concentrate on essential indicators of cytotoxicity, including metabolic activity, membrane integrity, oxidative stress, and apoptotic activation. The unique physicochemical properties should inform the choice of assay of the NPs to avoid inaccurate results due to assay interference (Kroll, Pillukat, Hahn, & Schnekenburger, 2012; Verissimo et al., 2016).

The MTT test is a widely employed technique that quantifies the transformation of a yellow tetrazolium salt into an insoluble formazan by mitochondrial dehydrogenases. Numerous investigations have shown that metallic NPs, including gold and silica-based particles, can disrupt colorimetric tests by either adsorbing the dye or independently initiating the reduction process, potentially leading to an exaggerated evaluation of viability or cytotoxicity (Braun et al., 2018; Lewinski, Colvin, & Drezek, 2008).

Alternative assays such as WST-1, MTS, and XTT utilize water-soluble tetrazolium salts, offering advantages in solubility and reduced NP interaction; yet, they are still vulnerable to redox-related interferences (Petersen, Reipa, Xia, & Sharma, 2021). ATP-based assays, such as CellTiter-Glo, offer increased sensitivity and reduced vulnerability to NP surface interactions, making them more reliable for high-throughput screening (Xianglu Han et al., 2011).

LDH release assays offer a standard approach for assessing membrane integrity. Upon cellular damage, LDH is released into the culture medium and is quantified enzymatically. This experiment is especially advantageous when employed in conjunction with viability tests to distinguish between necrotic and apoptotic cells (Kokalj, Drobne, & Novak, 2018).

To evaluate sub-lethal effects, ROS detection tests, including DCFH-DA, have been widely employed. These bright sensors indicate intracellular oxidative stress, a primary contributor to nanotoxicity. Nevertheless, NPs can either diminish or enhance fluorescence, necessitating appropriate controls (Fröhlich, 2012).

Innovative tools include flow cytometry-based viability assays (e.g., Annexin V/PI staining) that offer multiparametric evaluation of apoptosis, necrosis, and viability within a single experiment. These methodologies are advantageous for investigating the functional impacts of PDT or PTT, which often involve oxidative stress-induced apoptosis in cells (Shamjith et al., 2024).

Notably, 3D spheroid models offer a more biologically relevant framework for toxicity evaluation compared to 2D monolayers. Lee et al. identified significant variability in the cytotoxicity of CdTe and Gold NPs in 2D vs 3D HepG2 cells, with the 3D configuration demonstrating decreased toxicity due to the ECM and cell-to-cell interactions (J. Lee, Lilly, Doty, Podsiadlo, & Kotov, 2009). These models provide improved assessment of NP diffusion and penetration.

A comprehensive experiment of NP cytotoxicity requires a multi-assay approach tailored to the properties of the nanomaterial and the biological context. Incorporating metabolic, membrane integrity, oxidative stress, and apoptotic evaluations offers a thorough analysis of nanotoxicity.

2.6.2 Application of live/dead cell staining in barrier-integrated models

Live/dead cell labeling techniques are essential for evaluating cytotoxic responses in BBB and BBTB models, especially in intricate in vitro systems that involve many NVU cell types. These assays provide real-time observation and measurement of cell viability, enabling researchers to assess both direct cytotoxicity and functional barrier disruption after NP treatment or phototherapy.

The predominant live/dead test utilizes calcein-AM and ethidium homodimer-1 (EthD-1), where esterase activity in viable cells generates green fluorescence from calcein, while EthD-1 penetrates only damaged membranes and intercalates with DNA to create red fluorescence. This straightforward dual-dye method is efficacious for barrier models utilizing Transwell® inserts, as well as for dynamic co-culture configurations. Khafagy et al. illustrated its efficacy in a 3D microfluidic neurovascular unit model including mouse bEnd.Three endothelial cells, pericytes, and astrocytes effectively detect cell viability across a 21-day culture duration and connect findings with transendothelial electrical resistance and permeability alterations under treatment stresses (J. D. Wang, Khafagy, Khanafer, Takayama, & ElSayed, 2016).

Although straightforward, the calcein/EthD-1 approach is constrained by spectrum overlap, limitations in light penetration, and dye leaking during prolonged incubation. To overcome these constraints, two-photon fluorescent probes have been created for deep-tissue viability imaging. Tian et al. developed a dual-color probe based on excited-state intramolecular proton transfer (ESIPT), termed DACA, which emits orange fluorescence (570 nm) in live cells and blue fluorescence (440 nm) in nonviable cells upon two-photon stimulation. This probe had excellent photostability, little cytotoxicity, and facilitated accurate differentiation between viable and compromised cells in both monolayer and whole-organism models (Tian, Sun, Tang, Dong, & Lin, 2018).

Live/dead staining is especially significant in investigations using BBB or BBTB integrated phototherapy, because cytotoxic responses may manifest heterogeneously across cellular layers or compartments. Zheng et al. recently presented a barrier-integrated glioblastoma-on-chip platform that utilized live/dead assays to yield quantitative viability metrics after light-activated nanoparticle treatment, alongside TEER recordings and permeability assessments (Dmitriev, Borisov, Jenkins, & Papkovsky, 2015). The multidimensional readouts enabled researchers to monitor spatially resolved toxicity within endothelial layers and tumor spheroids—insights that were previously unattainable through traditional 2D culture alone.

Moreover, the implementation of automated high-content imaging technologies, such as the Incucyte platform, has facilitated the real-time kinetic assessment of viability under phototherapeutic stress, particularly in co-culture or organ-on-chip systems (Gust et al., 2017). This facilitates the measurement of treatment efficacy while maintaining the spatial design of barrier models and circumventing disruptive sample processing.

In conclusion, live/dead staining offers a reliable and adaptable method for detecting NP- or light-induced cytotoxicity in intricate BBB/ BBTB systems. The integration of electrophysiological or permeability tests enables a thorough assessment of cellular health and barrier function, hence enhancing the translational potential of therapeutic nanomaterials in brain-targeted applications.

2.7 Methodological Limitations and Developing Opportunities for BBB and BBTB

Accurately simulating the BBB and BBTB remains a critical challenge in preclinical neuroscience and oncology research. Notwithstanding the progress of diverse in vitro platforms, such as Transwell® systems, dynamic microfluidics, and organ-on-chip technologies, significant methodological and biological constraints remain, obstructing the accurate reproduction of barrier physiology and its utility in assessing NP-based phototherapies.

A significant limitation of several conventional models is their failure to capture the entirety of cellular complexity. The absence of pericytes, astrocytes, or neurons leads to subpar TEER values and insufficient TJ formation, compromising the predictive validity of these models for drug and NP evaluation (Helms et al., 2016; J. D. Wang et al., 2016). The ongoing maintenance of NVU-like architecture in co-culture settings is difficult, especially in static systems devoid of shear stress and perfusion mimicry (Brown et al., 2015; Engelhardt, 2003).

The BBTB introduces distinct challenges that differ from those of the healthy BBB. Pathological angiogenesis, glioma-derived factors, and localized inflammatory signals influence the heterogeneous permeability and variable transporter expression of the

BBTB. This geographical variability undermines the dependability of single-time-point permeability measurements and complicates the development of uniform NP-based delivery systems (Arvanitis et al., 2020; Obermeier, Daneman, & Ransohoff, 2013; Xie et al., 2008). The disruption of TJs inside the tumor core, together with partial retention at the invasive edges, hampers the precise assessment of nanoparticle penetration across the whole tumor volume (Jain & Stylianopoulos, 2010).

Another constraint is the limited integration of physiological shear stress and dynamic flow. Notwithstanding progress in microfluidic platforms and 3D perfused models designed to emulate realistic vascular environments, they often face challenges including restricted productivity, complex manufacturing procedures, and inconsistency across laboratories (Prabhakarpandian et al., 2013; Y. S. Zhang et al., 2017). Moreover, the integration of real-time analytics—such as dynamic permeability tracking, electrochemical sensing, or phototherapeutic response monitoring—remains substantially underdeveloped (Straehla et al., 2022).

New prospects arise at the intersection of advanced biomaterials, bioengineering, and computational modeling. For instance, 3D bioprinted NVU constructs that incorporate endothelial, glial, and neuronal populations offer spatial precision and regulation of matrix stiffness and microarchitecture—elements known to influence BBB phenotype and permeability (Nzou et al., 2020; Tang et al., 2021). Moreover, the incorporation of real-time biosensors in microfluidic BBB-on-chip devices has begun facilitating dynamic observation of drug transport, TEER, and cellular survival in therapeutic contexts (Padhani & Miles, 2010).

In silico technologies, including machine learning algorithms and quantitative structure–activity relationship (QSAR) models, are utilized to forecast BBB permeability based on physicochemical characteristics. Despite their potential, these techniques are limited by training datasets that often exclude dynamic or disease-specific features, such as cytokine-induced permeability changes or transporter saturation (F Morales, Scioli Montoto, Fagiolino, & E Ruiz, 2017).

In conclusion, despite significant progress in modeling the BBB and BBTB, several technological and biological constraints persist, impeding their translational application in evaluating NP-mediated phototherapies. Hybrid systems that incorporate co-culture complexity, mechanical stimulation, and real-time sensing—enhanced by in silico modeling—constitute a substantial possibility for progress and offer potential for connecting preclinical evaluation with clinical translation.

Notwithstanding substantial progress in nanomedicine, GBM continues to provide a considerable treatment challenge, mostly due to the restrictive characteristics of the BBB and its pathological equivalent, the BBTB. Nanomaterials, including gold nanorods (GNRs), copper sulfide nanoparticles (CuS), Prussian blue nanocubes, and graphene quantum dots (GQDs), have been examined for their efficacy in PTT and PDT within glioblastoma models (Domingo-Diez et al., 2023; L. Gao et al., 2020; Hill et al., 2024; Kregielewski, Fraczek, & Grodzik, 2025; Tong et al., 2023). Nonetheless, these methodologies were mainly assessed in direct tumor cultures or animal models, and no research has systematically integrated light-activated nanomaterials into Transwell-based BBB/BBTB models, which are considered physiologically relevant in vitro platforms for nanoparticle transport and barrier-tumor interactions.

This thesis examines the phototherapeutic efficacy of titanium carbide and tantalum carbide MQDs, both separately and in conjunction, within static and co-culture Transwell BBB/BBTB systems composed of hCMEC/D3 endothelial cells and U87 glioblastoma cells. MQDs are nanoscale materials measuring approximately 4–5 nm, exhibiting both photothermal and photodynamic characteristics (W. Kong et al., 2019; Zhu, Feng, Zhao, Liu, & Yang, 2024). Nanoparticles within this size range have been documented to penetrate endothelial layers through vesicular and non-vesicular pathways (Fatima et al., 2020; R. Gromnicova et al., 2013).

Hypothesis. Ti_3C_2 and Ta_4C_3 MQDs are combined to cross the BBB and BBTB models, preferentially inducing cytotoxicity in glioblastoma cells upon light activation while preserving endothelial viability. It is hypothesized that the simultaneous use of both MQDs (evaluated here for the first time in barrier-integrated in vitro systems) will provide

a synergistic improvement in phototherapeutic efficacy that surpasses the effects of each material individually.

3. MATERIAL AND METHODS

3.1 Materials

Table 3.1 Cell types and cell culture materials used in the thesis

	hCMEC/D3	U87
Cell Type	Immortalized human microvascular endothelial cells	Human glioblastoma astrocytoma cell line
Growth Medium & Supplements	EndoGRO™-MV Complete Media Kit (Cat. No. SCME004, Merck, Millipore) - EndoGRO™-MV kit components - 1 ng/mL recombinant human FGF-2 (Lot. No. 1563542C, Invitrogen Gibco) - 10% FBS (Cat. No. 10500064, Gibco) - 1% Penicillin-Streptomycin (Cat. No. 15140122, Gibco)	Minimum Essential Medium (1X, Lot. No. 2411746, 31095-029, Gibco) - 10% FBS (Cat. No. 10500064, Gibco) - 1% Penicillin-Streptomycin (Cat. No. 15140122, Gibco)
Culture Substrate	Collagen Type I from rat tail (Lot. No. SLBW1777, Sigma) diluted in DPBS (1X, Cat. No. 14190094, Gibco)	No coating for monoculture; Coated Transwell insert with Collagen Type I for co-culture
Culture Surface	T-75 flask or collagen-coated Transwell insert (Corning®, 3460)	T-75 flask or the bottom wells of the Transwell plate
Incubation Conditions	37°C, 5% CO_2, humidified incubator	37°C, 5% CO_2, humidified incubator
Trypsinization	0.25% Trypsin-EDTA (1X, 0.25 %, Cat. No. 25200056, Gibco)	0.05% Trypsin-EDTA (1X, 0.05 %, Cat. No. A1413201, BI)
Freezing Medium	90% EndoGRO™ Complete Media + 10% DMSO (5X, D2650, Sigma)	90% FBS(Cat. No. 10500064, Gibco) + 10% DMSO (5X, D2650, Sigma)
Storage Temperature	Liquid nitrogen (-196°C)	Liquid nitrogen (-196°C)
Passage Number	5	7

Table 3.2 Comparative overview of Ti_3C_2 and Ta_4C_3 Mxenes in light-activated cancer treatment

Material	Main Mechanism	Key Findings in Literature	Representative Wavelengths	References
Ti_3C_2 Mxene	High NIR photothermal conversion efficiency (~52%), ROS generation under light activation (PDT effect)	Ti_3C_2 quantum dots demonstrated efficient tumor ablation in vitro and in vivo under NIR light	808 nm optimal for PDT+PTT, 660 nm high PDT, 980/1064 nm lower PDT	(Xiaoxia Han et al., 2018; Liao et al., 2023)
Ta_4C_3 Mxene	High photothermal conversion efficiency, especially at 1064 nm; strong hyperthermia (PTT effect)	Ta_4C_3 composites (e.g., Ta_4C_3-IONP-SPs) enabled multimodal imaging and high-efficiency PTT in cancer models	1064 nm optimal for PTT, 808/980 nm moderate PTT, 660 nm low PTT	(Z. Liu et al., 2018)
Ti_3C_2 + Ta_4C_3 Combination	Synergistic PDT (from Ti_3C_2) + PTT (from Ta_4C_3) effects for enhanced cancer cell killing	Predicted to combine high ROS generation of Ti_3C_2 with strong photothermal properties of Ta_4C_3 for synergistic phototherapy; limited direct literature, mainly hypothesis-driven	808 nm predicted optimal for synergy, 1064 nm high PTT, 660 nm moderate PDT	(C. Kong & Chen, 2022; G. Liu et al., 2017)

Table 3.3 Assay types, assay materials, and devices used in the thesis

Assay Name	Purpose	Reagents / Kits	Readout / Instrument
LDH Assay	Quantification of membrane damage and cytotoxicity	CyQUANT™ LDH Cytotoxicity Assay Kit (Thermo Fisher Scientific, Cat. No. C20301)	Absorbance at 490 nm (reference: 680 nm) Microplate reader (Mithras2 LB 943, Berthold Technologies)
Live/Dead Cell Staining	Discrimination of viable vs. dead cells via fluorescence	LIVE/DEAD™ Viability/Cytotoxicity Kit (Thermo Fisher Scientific, Cat. No. L3224) Contains Calcein-AM and EthD-1	Fluorescence microscope (Zeiss)Green: live cells (Calcein), Red: dead cells (EthD-1)

3.2 Methods

This research utilized titanium carbide-derived (Ti_3C_2) and tantalum carbide-derived (Ta_4C_3) Mxene quantum dots (MQDs) as the primary fluorescent nanomaterials. These MQDs were kindly provided by Prof. Sanjiv Dhingra from the Department of Physiology and Pathophysiology, Max Rady College of Medicine, University of Manitoba, Canada. The Mxenes were synthesized via a hydrothermal method in distilled water and characterized as 2D structures with an average diameter of approximately 4.58 nm(Ashraf et al., 2022).

Mxenes are 2D quantum dots increasingly recognized for their unique physicochemical and biological properties, particularly in cell culture and biomedical applications, including tissue engineering. They possess high photothermal conversion efficiency, enabling the transformation of light—especially in the NIR range—into localized heat for PTT. This property enables tumor ablation via focused heat, reducing harm to adjacent healthy tissues.

In addition to PTT, Mxenes exhibit promising potential for PDT. Upon light activation, their surface terminations and electronic structure allow for the generation of ROS, which induce oxidative stress-mediated apoptosis in cancer cells. This dual functionality (PTT and PDT) offers opportunities for synergistic phototherapy, enhancing therapeutic efficacy and overcoming limitations such as tumor hypoxia or uneven heat distribution.

Their intrinsic biocompatibility and substantial surface area provide effective drug or photosensitizer loading, while adjustable surface chemistry permits regulated release in response to tumor-specific microenvironmental stimuli (e.g., pH, enzyme activity). These attributes render MQDs very appropriate for multimodal cancer therapy approaches (L. Chen, Dai, Feng, & Chen, 2022; Rastin et al., 2020; Scheibe et al., 2019).

3.2.1 Culture of the cell lines

Cell proliferation in controlled laboratory conditions, known as *cell culture*, constituted a fundamental aspect of this study. Two distinct human cell lines were used: the U87 GBM cell line, obtained from the American Type Culture Collection (ATCC), and the hCMEC/D3 human brain microvascular endothelial cell, purchased from Sigma-Aldrich.

To establish an *in vitro* BBTB model, the cell lines were initially cultured individually and subsequently co-cultured under optimized conditions. Table 3.1 presents the specific characteristics, growth media compositions, and culture requirements for both cell types. All cell culture procedures were made in a laminar flow hood under aseptic conditions, with ultraviolet light sterilization applied before each session.

3.2.1.1 Thawing of cell lines

Cryopreserved cells were stored in a liquid nitrogen tube (-176°C) and rapidly thawed in a water bath (37 °C) until a small ice crystal remained, allowing for gradual temperature equilibration. The external surface of each cryovial was disinfected with 70% ethanol before transfer into the biosafety cabinet.

The suspension of cells was placed into a 15 mL centrifuge tube, and warmed complete growth media was incrementally added to achieve to volume of 5 mL. The resultant suspension was centrifuged at 300 g for 5 min. to eliminate remaining DMSO. The supernatant was removed, and the cell pellet was resuspended in 7–8 mL of new complete culture media. Following careful pipetting to achieve a uniform suspension, cells were inoculated into a culture flask T-25 and incubated at 37 °C, 5% CO_2 environment.

3.2.1.2 Cell culture and passaging protocol for hCMEC/D3

To enhance attachment of cells, culture placements were pre-coated with type 1 collagen .1:20 dilution of type 1 collagen in Dulbecco’s phosphate-buffered saline (DPBS) was

prepared and added to the designated culture plates or flasks. The coated plates were incubated at 37 °C for at least 1 h before use.

The EndoGRO™ Basal Medium, which was supplemented with the EndoGRO™-MV Complete Supplement Kit and 1 ng/mL basic fibroblast growth factor (FGF2), kept under sterile and light-protected conditions. FGF2 was prepared by dissolving 10 µg of lyophilized FGF2 in 1 mL DPBS containing 0.1% bovine serum albumin (BSA), vortexed thoroughly, and sterilized using a 0.22 µm syringe filter. For 50 mL of complete EndoGRO™ medium, 47.5 mL of basal medium was supplemented with:100 µL EndoGRO LS supplement, 50 µL recombinant human EGF (rhEGF), 50 µL hydrocortisone hemisuccinate, 50 µL ascorbic acid, 50 µL heparan sulfate, and 5 µL FGF2 stock solution.

Following the removal of the type 1 collagen coating, plates were rinsed with DPBS and filled with freshly prepared complete medium. hCMEC/D3 cells were seeded onto the coated plates, and the medium was replaced the following day with fresh EndoGRO™ medium. Passaging was performed when cells reached 80% confluency.

For passaging, flasks were freshly coated with type 1 collagen. After aspirating the old medium, cells were rinsed with 4 mL DPBS in a T-25 flask, 1 mL Trypsin-EDTA was added to the flask, and incubated at 37 °C for ~4 min. Detached cells, verified by inverted light microscopy (ILM), were neutralized with 3 mL of complete medium. The suspension was transferred to a new flask with fresh medium (final volume 4–8 mL for T-25 flasks) and incubated at 37 °C with 5% CO_2.

After trypsin neutralization, cells were centrifuged at 300 x g for 5 min, resuspended in fresh medium, and counted with a hemocytometer (see Figure 3.1). Counting was performed in the four red-marked corner squares of the 4×4 grid, and the average value was multiplied by 10^4 to determine cells/mL. This value was used to calculate total cell numbers and the required seeding volume.

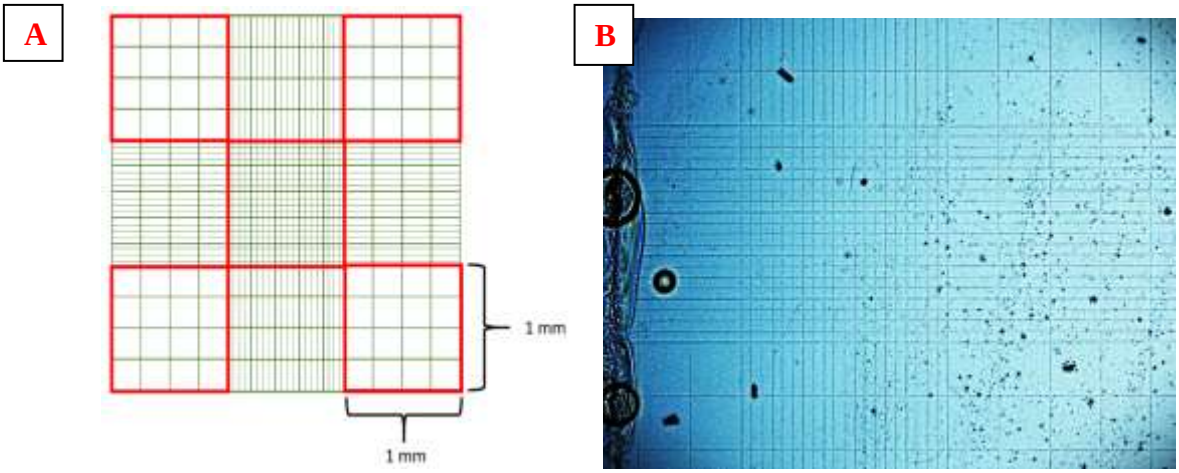

Figure 3.1 (A)Visualized image under ILM and (B) realistic hemocytometer image on ILM

3.2.1.3 Cryopreservation of hCMEC/D3

Cells were cryopreserved for long-term preservation utilizing a controlled rate freezing protocol. The cells were detached as mentioned above in section 3.2.1.2. After detaching cells, the cell suspension was carefully transferred into a 15 mL sterile conical centrifuge tube. Cells were subjected to centrifugation at 300 x g for 5 min, following which the supernatant was discarded. The cell pellet was reconstituted in 1 mL of pre-chilled freezing media, as specified in Table 3.4, for each cryovial. Cryovials were promptly positioned in a Mr. Frosty™ container filled with isopropanol alcohol to facilitate a controlled cooling rate of approximately 1°C per minute, and were subsequently stored overnight at –80°C. The following day, cryovials were moved to –176°C storage for long-term preservation.

3.2.1.4 Subculturing of hCMEC/D3 for BBB constructions

To develop an in vitro monoculture model of the BBB, suitable seeding densities and working volumes were identified according to Table 3.4. Transwell-clear polyester (PET) inserts featuring a 0.4 µm pore size membrane were precisely placed into the wells of 24-well culture plates. Before cell seeding, the upper membrane surface of each insert was coated with type 2 collagen according to the protocol in Section 3.2.1.2 and incubated

in an incubator at 37 °C with 5% CO_2 for a minimum of 1 h to improve cell adhesion. Following the coating process, a suspension of hCMEC/D3 cells was applied to the apical surface of the insert in a dropwise manner, ensuring uniform distribution across the membrane surface while preserving the integrity of the coating. To facilitate nutrient exchange and replicate physiological conditions, 500 µL of fresh medium was introduced to the basolateral compartment of each well.

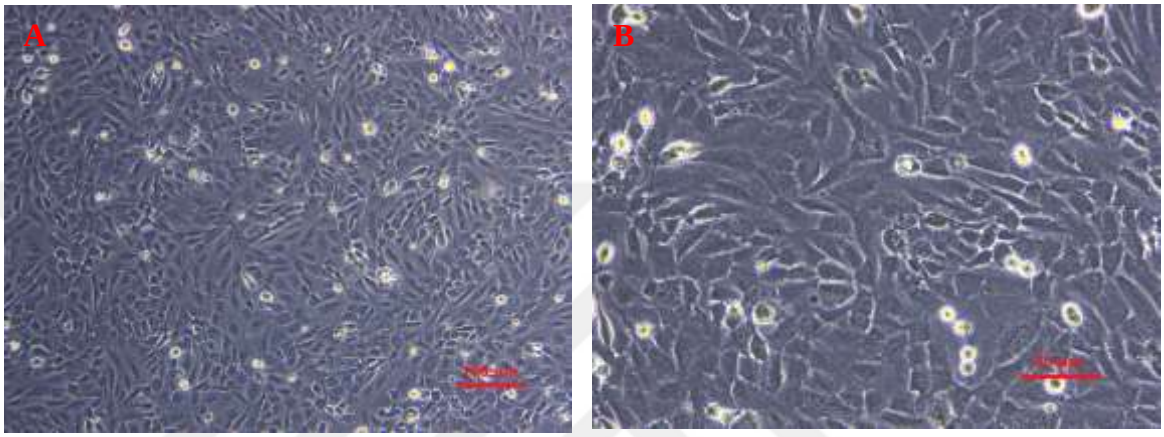

Figure 3.2 ILM images of hCMEC/D3 cell line at passage +4 (A: 10X, scale bar: 100 µM, B: 20X, scale bar: 50 µM)

3.2.1.5 Culturing of U87 Cancer Cell Line

Before starting U87 cell culture, the MEM was augmented with 10% fetal bovine serum (FBS) and 1% penicillin-streptomycin (P/S) to create a complete growth medium.

U87 cells were thawed according to the cryovial thawing protocol outlined in Section 3.2.1.1. Following rapid thawing in a 37 °C water bath and decontamination with 70% ethanol, the vial contents were gradually diluted with complete MEM, centrifuged at 300 x g for 5 min., and resuspended in fresh medium. The cell suspension was placed in a suitable culture vessel and incubated at 37°C with 5% CO_2. Upon reaching approximately 70–80% confluency, U87 were passaged with 0.05% Trypsin-EDTA. The protocol for passaging, seeding, and cryopreservation was consistent with that utilized for hCMEC/D3 cells, except that MEM medium replaced EndoGRO™. The passaging process involved washing with DPBS, enzymatic detachment using Trypsin-EDTA, neutralization with

serum-containing medium, centrifugation, and reseeding into newly prepared culture flasks. Cells that were not utilized immediately were cryopreserved in freezing medium according to the previously outlined protocol.

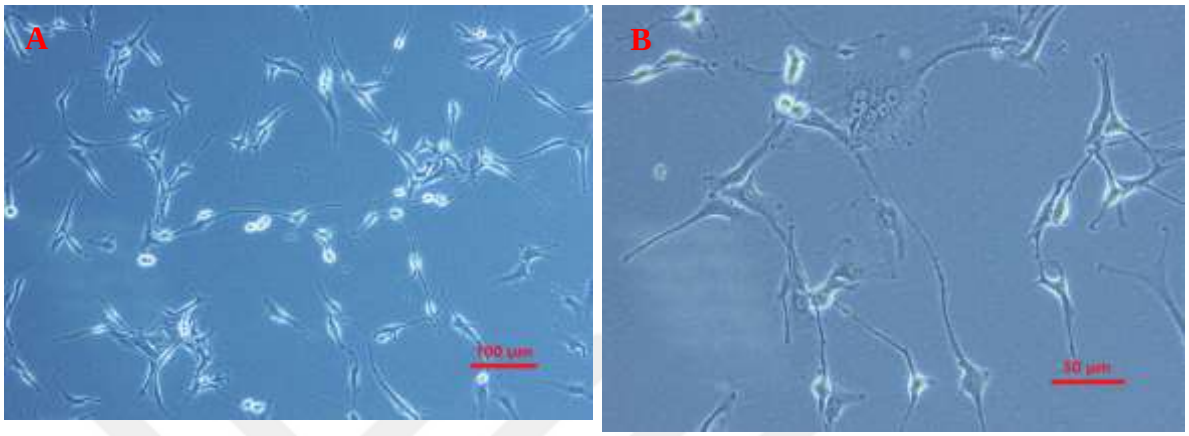

Figure 3.3 ILM image of U87 at passage +7 (A: 10X, scale bar: 100 µM, B: 20X, scale bar: 50 µM)

Table 3.4 Culture conditions and seeding parameters for hCMEC/D3 and U87 cell lines

Cell Line	Culture Medium	Freezing Medium	Trypsin-EDTA	Coating	Seeding (24-well plate)	Seeding (24-well Transwell)	Medium Volume
hCMEC/D3	EndoGRO™-MV + 1 ng/mL FGF2	90% Completed EndoGRO™ + 10% DMSO	0.25%	Collagen type 1 diluted in DPBS	-	20,000 cells/insert	100–300 µL
U87	MEM + 10% FBS + 1% Penicillin-Streptomycin	90% FBS + 10% DMSO	0.05%	-	50,000 cells/well	-	500 µL to 1 mL

3.2.2 Formation of in vitro BBTB models

3.2.2.1 Models with hCMEC/D3 and U87

Before the seeding process, Transwell-clear inserts were systematically positioned into the wells of the Transwell-compatible 24-well plates. The inserts' membranes were coated with type 1 collagen and incubated at 37 °C for 1 h to enhance cell adhesion, as outlined in Sections 3.2.1.4. U87 cells were seeded in the bottom well (basolateral compartment) of the transwell plate for co-culture assembly and permitted to attach for 1–2 hours in a humidified incubator at 37 °C and 5% CO_2.

After adequate adherence of U87 cells, hCMEC/D3 cells were seeded on the apical surface of the pre-coated Transwell insert. An incubation period of approximately 2 h was implemented to promote the initial attachment of hCMEC/D3 cells to the insert membrane. The insert was subsequently reinserted into the well containing the previously adhered U87 cells. Following the attachment period, the co-culture system was sustained overnight under standard culture conditions to facilitate stable cell-to-cell communication across the insert membrane prior to experimental treatments or evaluations. Figure 3.4 provides a schematic representation of this setup.

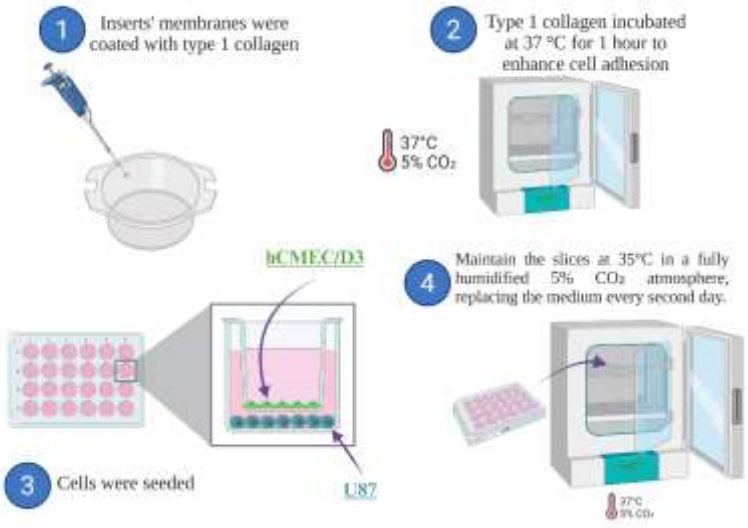

Figure 3.4 Co-culture protocol (Created by BioRender)

3.2.3 Cytotoxicity assay in BBTB models

3.2.3.1 Optimization of proper Mxene type, concentration, and wavelength

Preliminary experiments were conducted to determine the optimal MQD type, concentrations, and excitation wavelengths that maximize phototherapy efficacy by selectively inducing cytotoxicity in GBM cells while maintaining the viability of Ecs. This was crucial for achieving an appropriate equilibrium between optimal tumor cell death (through photothermal or photodynamic effects) and minimal toxicity to the barrier-forming endothelial layer in the co-culture model.

To identify the optimum concentration and radiation wavelength for MQDs in phototherapy applications, in vitro cytotoxicity assessments were performed utilizing U87 cells. Cells were seeded in 96-well plates at 5.000 cells per well in 100 µL of complete MEM and incubated overnight at 37 °C in a 5% CO_2 to facilitate attachment.

After incubation, the old medium was aspirated and substituted with fresh medium containing different concentrations of MQDs, as outlined in Table 3.5, and the cells were subjected to these conditions for 4 h. Control groups were administered fresh medium devoid of nanomaterial exposure. Following the treatment period, the medium with MQDs was aspirated and substituted with 100 µL of fresh medium in all wells. The plates were then exposed to LED irradiation for 1 h at either 520 nm (green light) or 850 nm (near-infrared light), which aligns with the peak absorbance of the MQDs. Following irradiation, the cells were incubated under standard conditions for an additional 24h to assess any delayed cytotoxic effects.

After the incubation period, LDH release was quantified using the Thermo Scientific™ Pierce™ LDH Cytotoxicity Assay Kit, by protocol of the manufacturer's protocol, to assess cell membrane integrity and evaluate phototherapy-induced cytotoxicity. Absorbance values at 490 nm (experimental signal) and 680 nm (background noise) were

recorded and analyzed to produce viability profiles that are dependent on both dose and wavelength.

Table 3.5 Summary of Mxene NP types with corresponding concentrations and light wavelengths

Mxene Type	Concentration	Wavelength
Titanium carbide- derived Mxene	5,10, 25, 50 μg/ml	520 nm /850 nm
Tantalum carbide-derived Mxene	5,10, 25, 50 μg/ml	520 nm /850 nm
Ti MQD + Ta MQD	5,10, 25, 50 μg/ml	520 nm /850 nm

3.2.3.2 Protocol for phototherapy exposure in cytotoxicity assessment

Day 1, U87 brain cancer cells were seeded in 96-well plates (5.000 cells / well) in 100 μL of complete medium. The plates were incubated overnight at 37 °C in a 5% CO_2 environment to facilitate cell attachment and growth.

On Day 2, the old medium was aspirated, and cells were treated with varying concentrations of MQDs, both photosensitive nanomaterials, freshly prepared in culture medium. The plates were incubated at standard conditions (37 °C, 5% CO_2) for 4 h to facilitate cellular uptake of the nanomaterials. Following incubation, the treatment medium was discarded and substituted with 100 μL of fresh medium. The plates were then exposed to light irradiation at specific wavelengths (520 nm or 850 nm) for 1 hour to induce photothermal and/or photodynamic effects. After exposure to light, cells were incubated for 24 hours before cytotoxicity assessment. Figure 3.5 illustrates the schematic representation of the phototherapy protocol.

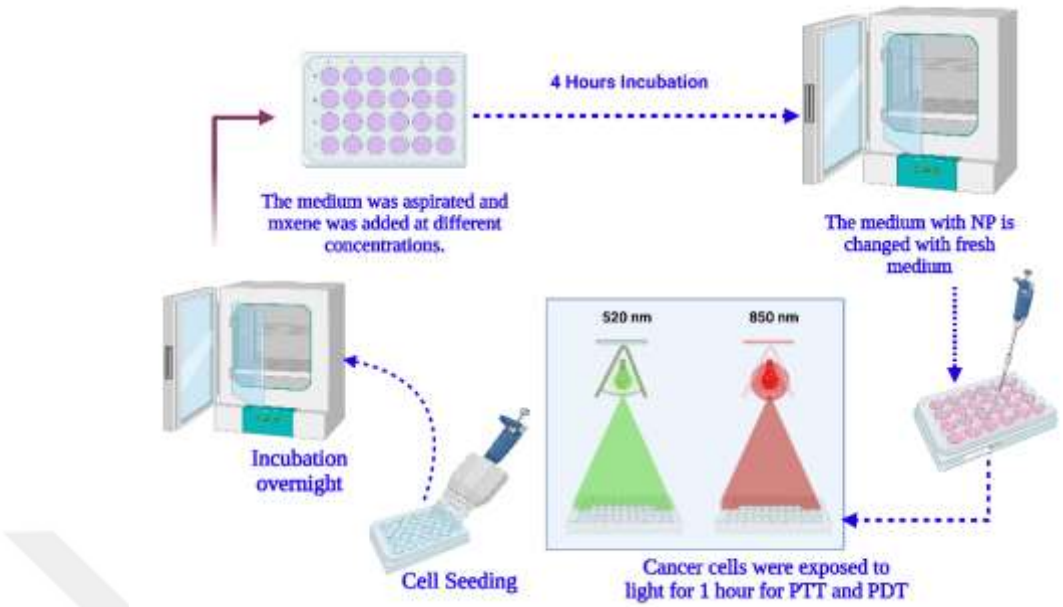

Figure 3.5 Illustration of Photothermal and Photodynamic Therapy Protocol (Created by BioRender)

3.2.3.3 LDH assay for viability assessment after PTT & PDT

An LDH assay was performed to investigate the cytotoxic effects of MQDs on cancer cells, following established protocols with the Thermo Scientific Pierce LDH Cytotoxicity Assay Kit. The experiment aimed to assess cellular viability following PTT and PDT treatments.

On Day 1 and Day 2, the phototherapy treatment was implemented as previously described.

On Day 3, the LDH assay was conducted to measure cytotoxicity. Before the assay, all reagents were melted to room temperature and shielded from light exposure.

The substrate stock solution was prepared by combining 11.4 mL of distilled water with the substrate mix, then adding 600 µL of assay buffer to create the reaction mix. 10 µl of lysis buffer was added to each well, followed by gentle pipetting of the plates and

incubated for 45 min at 37 °C. Lysis buffer and cells were collected in Eppendorf tubes, centrifuged at 13,000 rpm for 10 min, and 50 μL of the supernatant was transferred to a new 96-well plate. 50 μL of reaction mix was dispensed into each well and incubated for 30 min at room temperature in the dark. 50 μL of stop solution was introduced to halt the reaction. Absorbance was quantified at 490 nm and 680 nm utilizing a microplate reader.

Cell viability in the untreated control group was set at 100%, and the percent viability of the treated groups was calculated to produce comparative cytotoxicity profiles.

3.3 Live/Dead Cell Staining Protocol In Transwell-Based co-culture Model

A Live/Dead fluorescence assay was performed on the Transwell-integrated co-culture system of hCMEC/D3 and U87 cell lines to evaluate cell viability following phototherapeutic treatment. This assay enables the simultaneous imaging of viable and non-viable cells by specifically labeling living cells with a membrane-permeant dye (e.g., Calcein-AM) and dead cells with a membrane-impermeant DNA-binding dye (e.g., Ethidium Homodimer-1 or Propidium Iodide).

Three unique experimental arrangements were established as Figure 3.6: **Naive group:** hCMEC/D3 and U87 cells cultivated under regular conditions without phototherapeutic intervention, serving as the baseline viability control. The Naïve group represents the control condition, where hCMEC/D3 endothelial cells were cultured on the apical surface of the Transwell insert and U87 glioblastoma cells on the basal chamber, without exposure to either light or MQDs. **Indirect group:** hCMEC/D3 cells were seeded on the apical surface of the Transwell insert membrane, whereas U87 cells were cultured on the basolateral surface. In the Indirect group, MQDs were applied to the apical surface containing hCMEC/D3 cells, and 850 nm light irradiation was directed only to the apical compartment. The phototherapeutic treatment was administered to the U87 cells while preserving the barrier structure, allowing for the assessment of indirect effects mediated through the hCMEC/D3 cells monolayer. **Direct group:** hCMEC/D3 cells were seeded on the apical surface of the Transwell insert membrane, whereas U87 cells were cultured on the basolateral surface. In the Direct group, MQDs were administered to both the

apical and basal compartments, and light irradiation (850 nm) was applied simultaneously to both surfaces, allowing for direct exposure of U87 glioblastoma cells in the basal chamber.

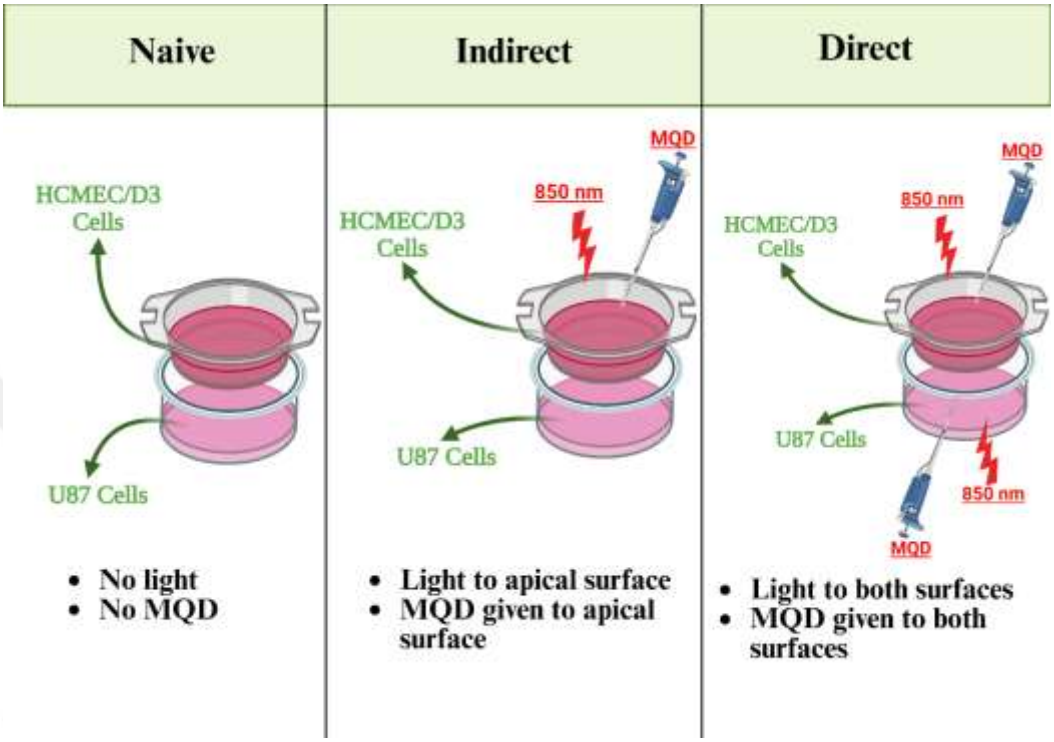

Figure 3.6 Experimental setups for Naive, Indirect, and Direct conditions in the hCMEC/D3–U87 Transwell co-culture model (Created by BioRender)

Following the completion of the phototherapy protocol (see Section 3.2.3.2), the Transwell inserts were cultured with hCMEC/D3 monolayers on the apical side and U87 cells on the basolateral side were thoroughly washed with DPBS to remove any remaining media and debris. The operating solution was newly formulated utilizing the Live/Dead Viability/Cytotoxicity Kit (e.g., Thermo Fisher Scientific, Cat. No. L3224) by diluting the subsequent components (Calcein-AM: final concentration of 2 micromolar, Ethidium Homodimer-1: final concentration of 4 micromolar) in DPBS (protected from light).

A total staining amount of 500 µL was applied to each insert to guarantee comprehensive coverage. The staining solution was meticulously introduced into both compartments of the Transwell system (apical and basolateral) without disturbing the cell layers. The plates were incubated in darkness at 37 °C with 5% CO_2 for 30 min. to enhance dye penetration

and response. Following incubation, surplus dye was eliminated by gently washing with DPBS.

Fluorescent pictures were promptly obtained using an inverted fluorescence microscope fitted with suitable filter sets (Calcein-AM: Excitation/Emission ~494/517 nm (green), EthD-1: Excitation/Emission ~528/617 nm (red)). The hCMEC/D3 and U87 cell layers were photographed independently to assess their distinct responses across the barrier under each experimental condition.

3.4 Statistical Analysis

The program known as GraphPad Prism, version 9, was utilized in order to do statistical analysis on the data. Statistical differences were investigated using a standard two-way analysis of variance (ANOVA), which was then followed by Tukey's multiple comparison test, which was carried out when required. Statistical significance was considered as $p < 0.05$, and the data displayed in the graphs were reported as the mean plus or minus the standard deviation, respectively.

4. RESULTS

4.1 Determination of Appropriate Material Concentration and Wavelength

The present research utilized the LDH assay to assess and evaluate the vitality of U87 brain cancer cells following the PTT&PDT protocol with various materials and concentrations, employing light wavelengths of 520 nm and 850 nm. Throughout the investigation, all groups were quantitatively assessed for cell viability, identifying the substance that most significantly diminished cancer cell viability, alongside determining the optimal quantity of the material and the light wavelength suitable for the PTT&PDT protocol.

U87 cancer cells were plated in 96-well plates at a density of 5.000 cells per well and incubated overnight at 37 °C with 5% CO_2. Upon completion of incubation, cancer cells were exposed to varying doses of titanium carbide-derived (Ti_3C_2) MQD and tantalum carbide-derived MQD (Ta_4C_3) (5, 10, 25, and 50 μg/ml) for 4 h. The media were subsequently aspirated, fresh media were introduced into the wells, and the samples were exposed to light at wavelengths of 520 nm and 850 nm for 1 hour. Following 24 hours, the Thermo LDH kit methods were used, and cell viability was assessed. The optical density was evaluated at wavelengths of 490 nm and 680 nm.

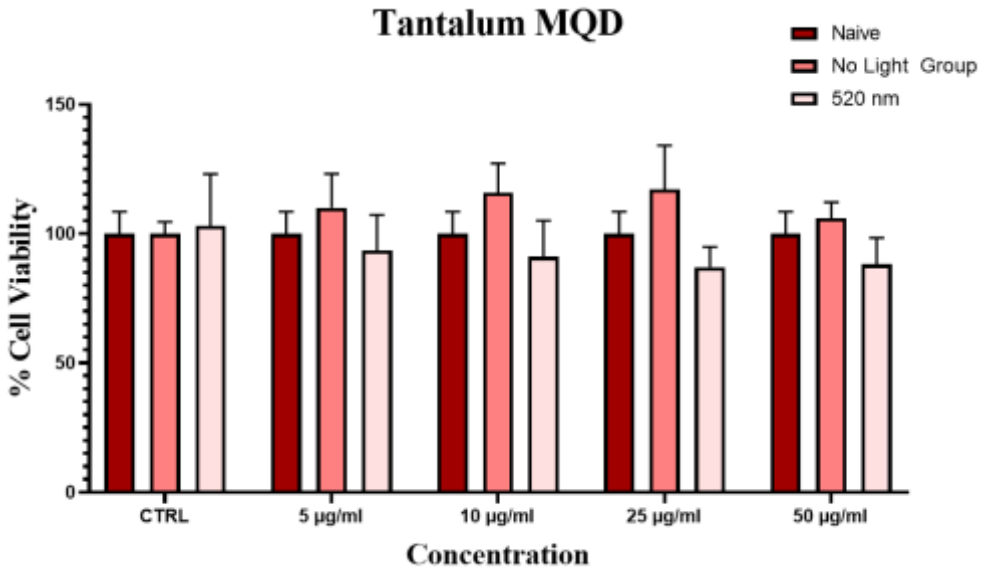

Figure 4.1 Cell viability of U87 cells. The cells treated with 520 nm and Tantalum carbide derived MQD after PTT & PDT protocol (n=5, P value>0.05)

The viability of U87 cells subjected to Ta_4C_3 MQDs at doses of 5, 10, 25, and 50 µg/mL was evaluated under Naive, No Light, and 520 nm irradiation conditions (Figure 4.1). Two-way ANOVA analysis indicated no statistically significant differences among treatment groups at any dose evaluated ($p > 0.05$). In all groups, viability values typically ranged from around 90% to 110% of control levels, suggesting that Ta_4C_3 MQDs did not elicit significant cytotoxicity under the specified circumstances, and 520 nm irradiation did not increase toxicity relative to the Naive or No Light groups.

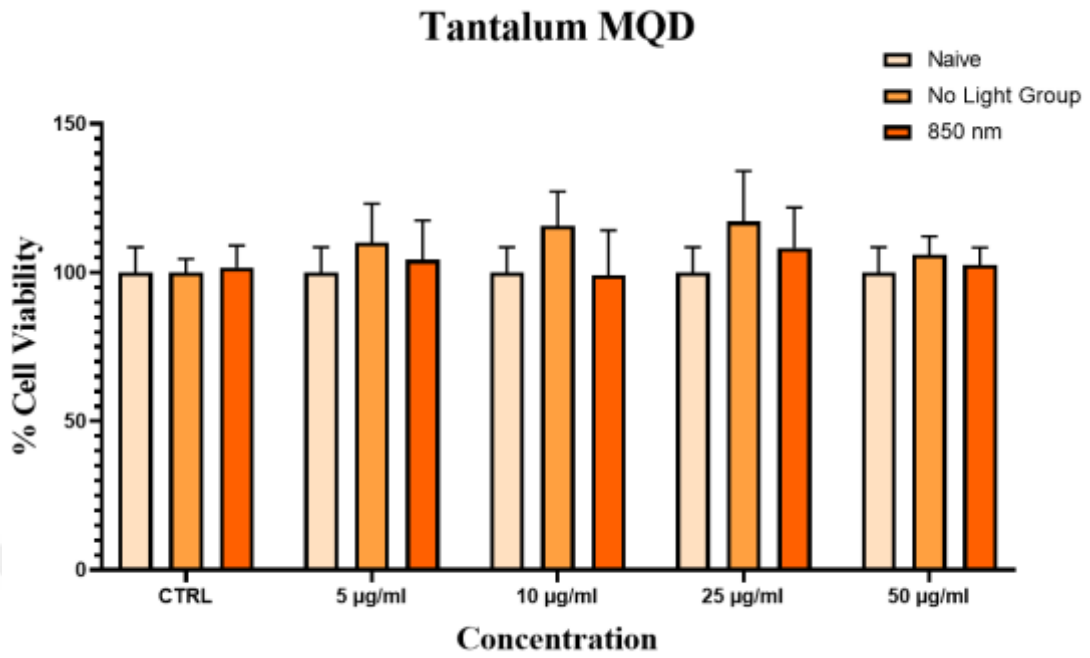

Figure 4.2 Cell viability of U87 cells. The cells treated with 850 nm and Tantalum carbide derived MQD after PTT & PDT protocol (n=5, P value>0.05)

The viability assessment of U87 cells subjected to Ta_4C_3 MQDs at concentrations of 5, 10, 25, and 50 µg/mL under Naive, No Light, and 850 nm irradiation conditions revealed no statistically significant differences among the treatment groups (two-way ANOVA, $p > 0.05$) (Figure 4.2). Viability values across all settings consistently fell within the 95–110% range of control levels, suggesting that Ta_4C_3 MQDs did not demonstrate measurable cytotoxicity under the tested conditions and that 850 nm irradiation did not enhance toxicity relative to the Naive or No Light groups.

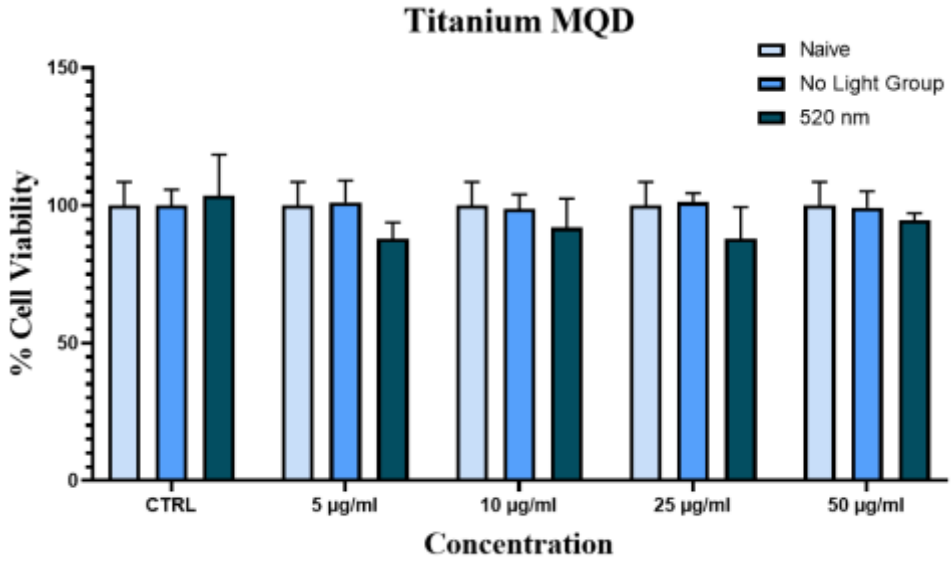

Figure 4.3 Cell viability of U87 cells. The Cells treated with 520 nm and Titanium carbide derived MQD after PTT & PDT protocol (n=5, P value>0,05)

Cell viability assessment of U87 cells subjected to Ti MQDs at concentrations of 5, 10, 25, and 50 µg/mL under Naive, No Light, and 520 nm irradiation conditions revealed no statistically significant changes among treatment groups (two-way ANOVA, $p > 0.05$) (Figure 4.3). Throughout all doses, viability values consistently ranged from 90% to 105% of the control, demonstrating that Ti MQDs did not elicit significant cytotoxicity under 520 nm irradiation. Exposure to light at this wavelength did not increase toxicity relative to the Naive or No Light groups.

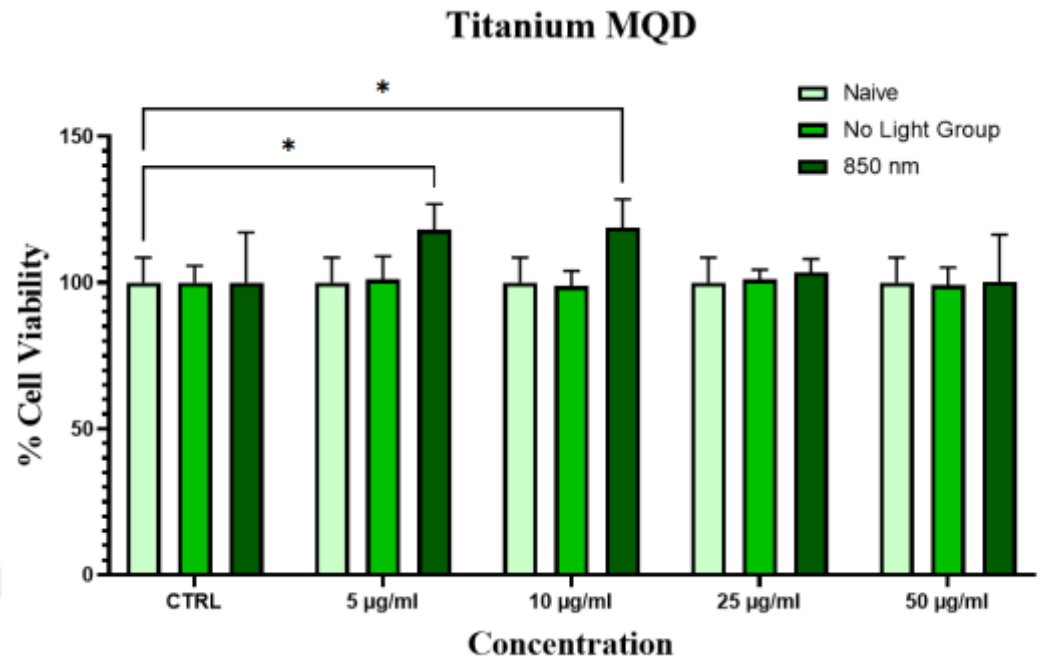

Figure 4.4 Cell viability of U87 cells. The cells treated with 850 nm and Titanium carbide derived MQD after PTT & PDT protocol (n=5, *P value<0,05)

The viability of U87 cells subjected to Ti_3C_2 MQDs (5, 10, 25, and 50 µg/mL) was assessed under Naive, No Light, and 850 nm irradiation conditions (Figure 4.4). Two-way ANOVA analysis demonstrated statistically significant differences, with 850 nm irradiation at 5 and 10 µg/mL doses yielding greater cell viability than the Naive control (*$p < 0.05$). The increase in viability indicates a possible photobiomodulation impact at low Ti MQD concentrations when exposed to NIR. At elevated quantities (25 and 50 µg/mL), no significant changes were seen among the groups, and cell viability values were comparable to control levels.

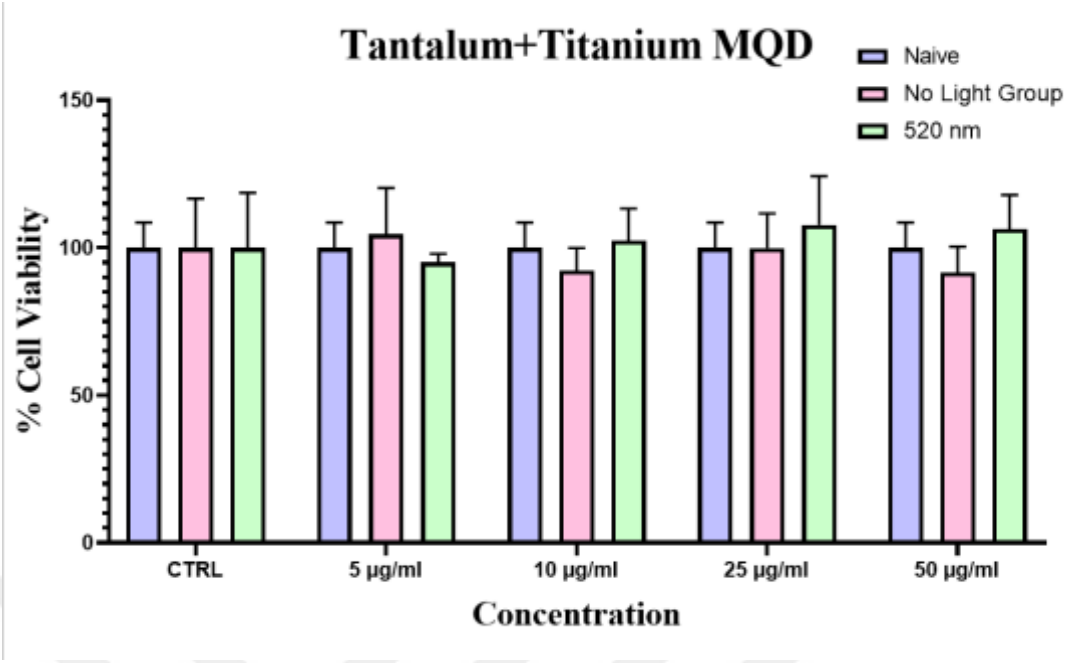

Figure 4.5 Cell viability of U87.The cancer cells treated with 520 nm, Ti+Ta combination MQD after PTT & PDT protocol (n=5, P value>0,05)

Cell viability assessment of U87 cells subjected to different doses of Ti+Ta MQDs (5, 10, 25, and 50 µg/mL) across Naive, No Light, and 520 nm irradiation groups revealed no statistically significant changes among treatment conditions (two-way ANOVA, $p > 0.05$) (Figure 4.5). At all tested doses, viability values were consistently between 90–110% of the control, and exposure to 520 nm light did not provide a significant decrease in viability relative to the Naive or No Light groups. The results demonstrate that Ti+Ta MQDs did not exhibit measurable cytotoxicity on U87 cells when subjected to 520 nm irradiation.

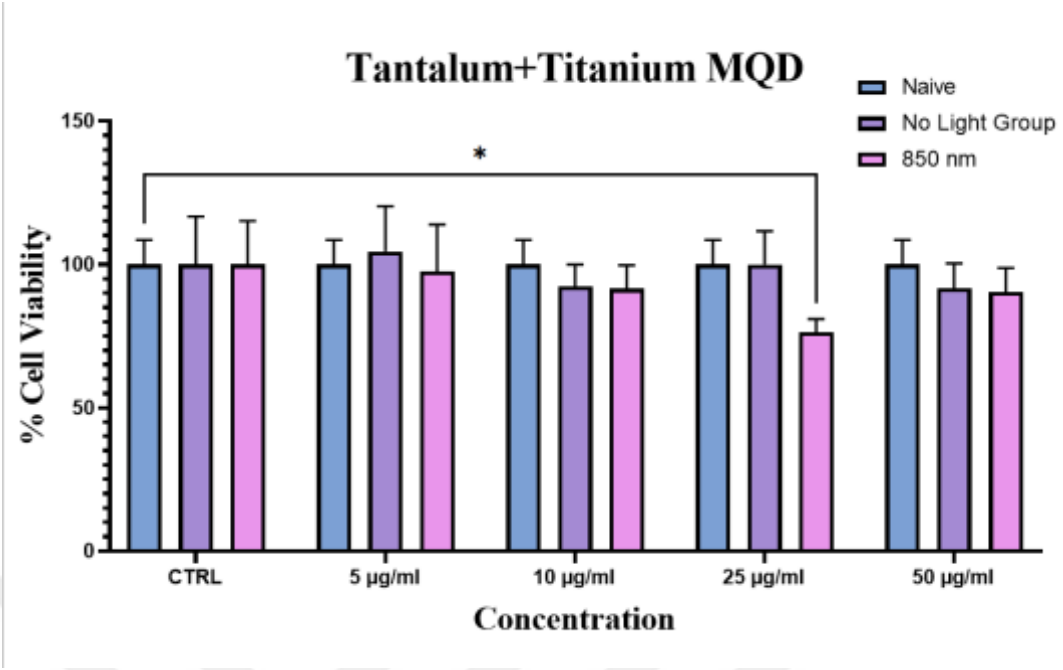

Figure 4.6 Cell viability of U87 cells.The cells treated with 850 nm, Ti+Ta combination MQD after PTT & PDT protocol (n=5, *P value<0,05)

Cell viability analysis of U87 cells treated with Ti+Ta MQDs (5, 10, 25, and 50 µg/mL) under Naive, No Light, and 850 nm irradiation conditions revealed a statistically significant reduction in viability for the 25 µg/mL + 850 nm group compared to the Naive control (two-way ANOVA, *p < 0.05) (Figure 4.6). While viability values for most concentrations remained within ~90–105% of the control, exposure to 850 nm light at 25 µg/mL resulted in the lowest observed cell viability, indicating an enhanced cytotoxic effect under this treatment condition. No other significant differences were observed among the remaining concentrations.

The LDH assay findings indicated that the titanium and tantalum combined MQD formulation (Ti+Ta) exhibited a much greater loss in U87 cell viability than the individual Ti or Ta MQD treatments. The impact was most pronounced at 25 µg/mL concentration under 850 nm irradiation, where the combined formulation elicited the highest cytotoxic reaction among the evaluated circumstances (Figure 4.2). Due to its exceptional efficacy and the novelty of this Ti+Ta combination as a photosensitizer for PTT and PDT

procedures, it was chosen for further phototherapeutic applications at a concentration of 25 μg/mL.

4.2 Live/Dead Assay Results

Live/Dead fluorescence imaging was used to investigate treatment-induced cytotoxicity in the hCMEC/D3–U87 Transwell co-culture, subsequent to the phototherapeutic regimen utilizing the Ti+Ta. Viable cells exhibited green fluorescence (Calcein-AM), while non-viable cells had red fluorescence (Ethidium homodimer-1). Representative photos for each setup are displayed in Figure 4.7, with merged panels facilitating concurrent evaluation of membrane integrity and morphology.

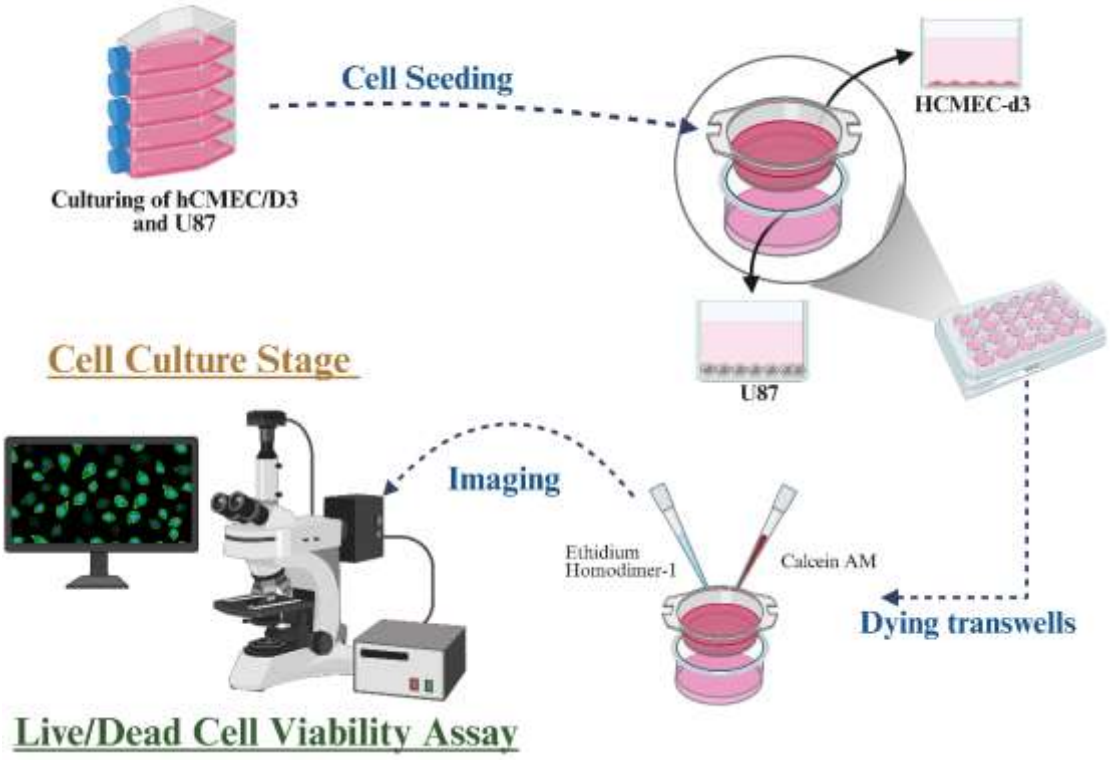

Figure 4.7 Schematic workflow of hCMEC/D3 and U87 co-culture in the Transwell system for Live/Dead cell viability assay (Created by BioRender)

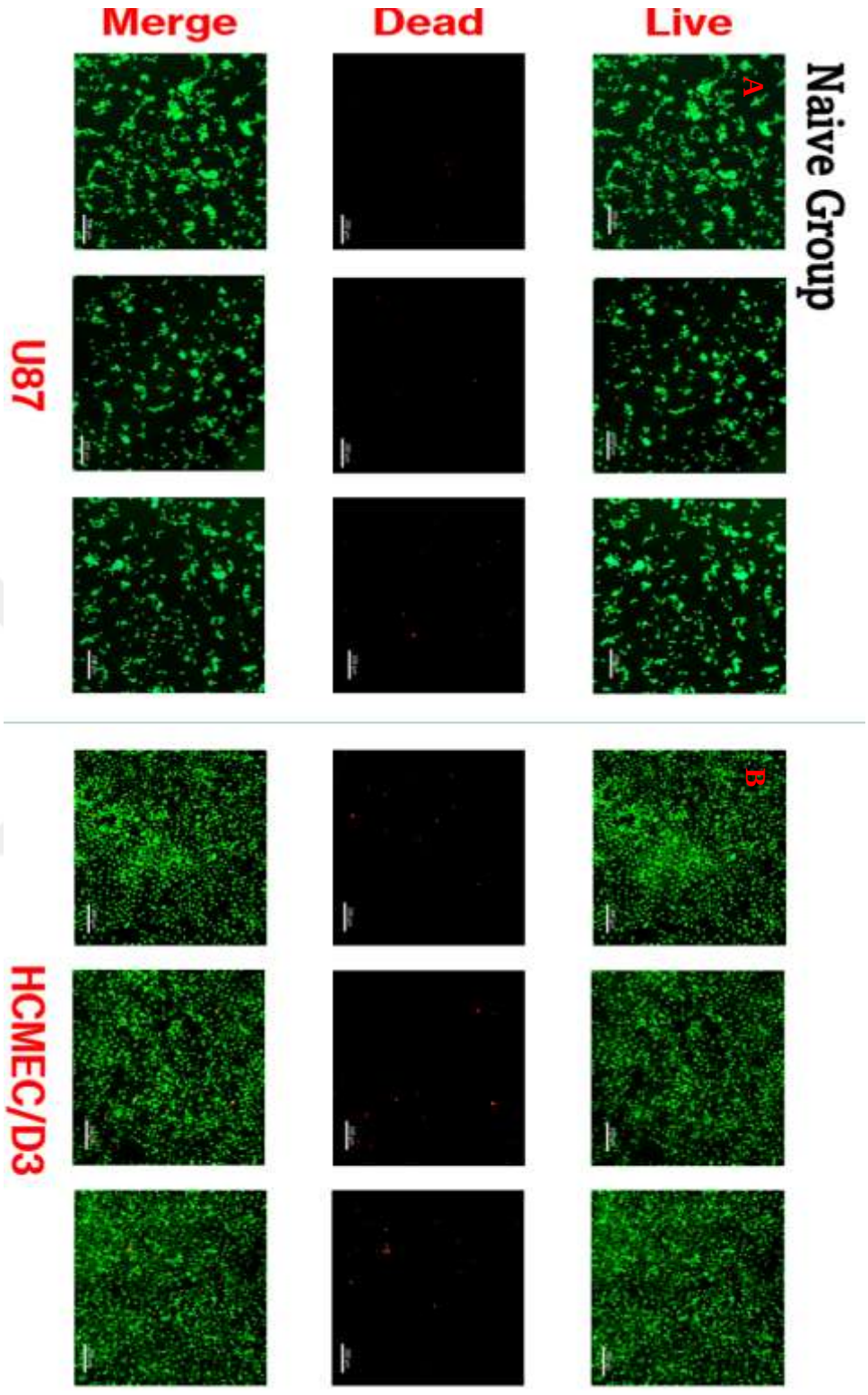

Figure 4.8 Representative Live/Dead fluorescence microscopy images of U87 glioblastoma cells (A) and hCMEC/D3 endothelial cells (Bin the groups. Scale bar: 200 μm

In the **Naive group**, both U87 and hCMEC/D3 cells displayed mostly green fluorescence with little red events (Fig. 4.7-A; 4.7-B), signifying elevated baseline viability and affirming that neither the co-culture configuration nor the staining protocol induced measurable cytotoxic stress.

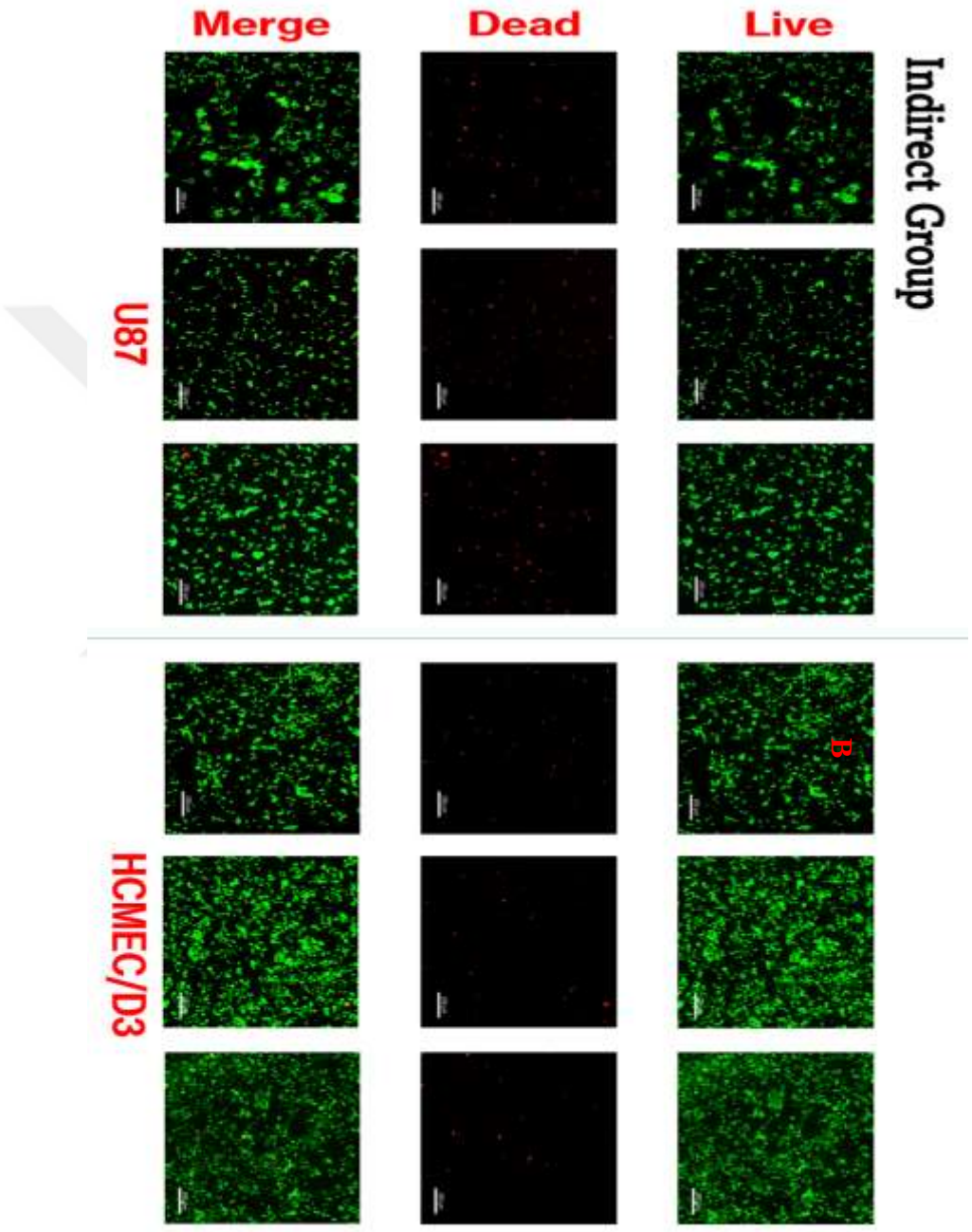

Figure 4.9 Representative Live/Dead fluorescence microscopy images of U87 glioblastoma cells (left) and hCMEC/D3 endothelial cells (right) in the Indirect group (Transwell configuration). Scale bar: 200 µm

In the Indirect group, where U87 and hCMEC/D3 cells were cultured in a Transwell configuration allowing barrier-mediated NP delivery, Live/Dead fluorescence imaging revealed a modest increase in red fluorescence in U87 cells compared to the Naive group, indicating a moderate rise in non-viable cells (Figure 4.8). Morphologically, U87 cells displayed early apoptotic features, including rounding and slight shrinkage, while still maintaining a substantial proportion of green-stained viable cells. In contrast, hCMEC/D3 cells monolayers largely retained green fluorescence with only a slight increase in red signal, suggesting minimal cytotoxicity to the endothelial barrier. The merged panels confirmed that cytotoxic effects were more pronounced in U87 glioblastoma cells than in hCMEC/D3 cells, consistent with partial attenuation of PDT/PTT effects by the Transwell interface and cell-type-specific susceptibility

In the Direct group, where both U87 and hCMEC/D3 cells were exposed directly to the Ti+Ta MQD solution and phototherapeutic illumination without the barrier separation of the Transwell system, Live/Dead fluorescence imaging revealed a marked increase in red fluorescence in U87 cells compared to both Naive and Indirect groups (Figure 4.9). This corresponded with pronounced morphological signs of cytotoxicity, such as cell rounding, membrane disruption, and reduced confluency. In contrast, hCMEC/D3 cells monolayers exhibited only a mild elevation in red signal relative to the Naive group, retaining a majority of green-stained viable cells, although minor membrane irregularities were observed. The merged panels visually confirmed the higher susceptibility of U87 glioblastoma cells to the combined photothermal and photodynamic effects of the Ti+Ta MQDs under direct exposure, consistent with LDH assay data indicating maximal cytotoxicity in this configuration.

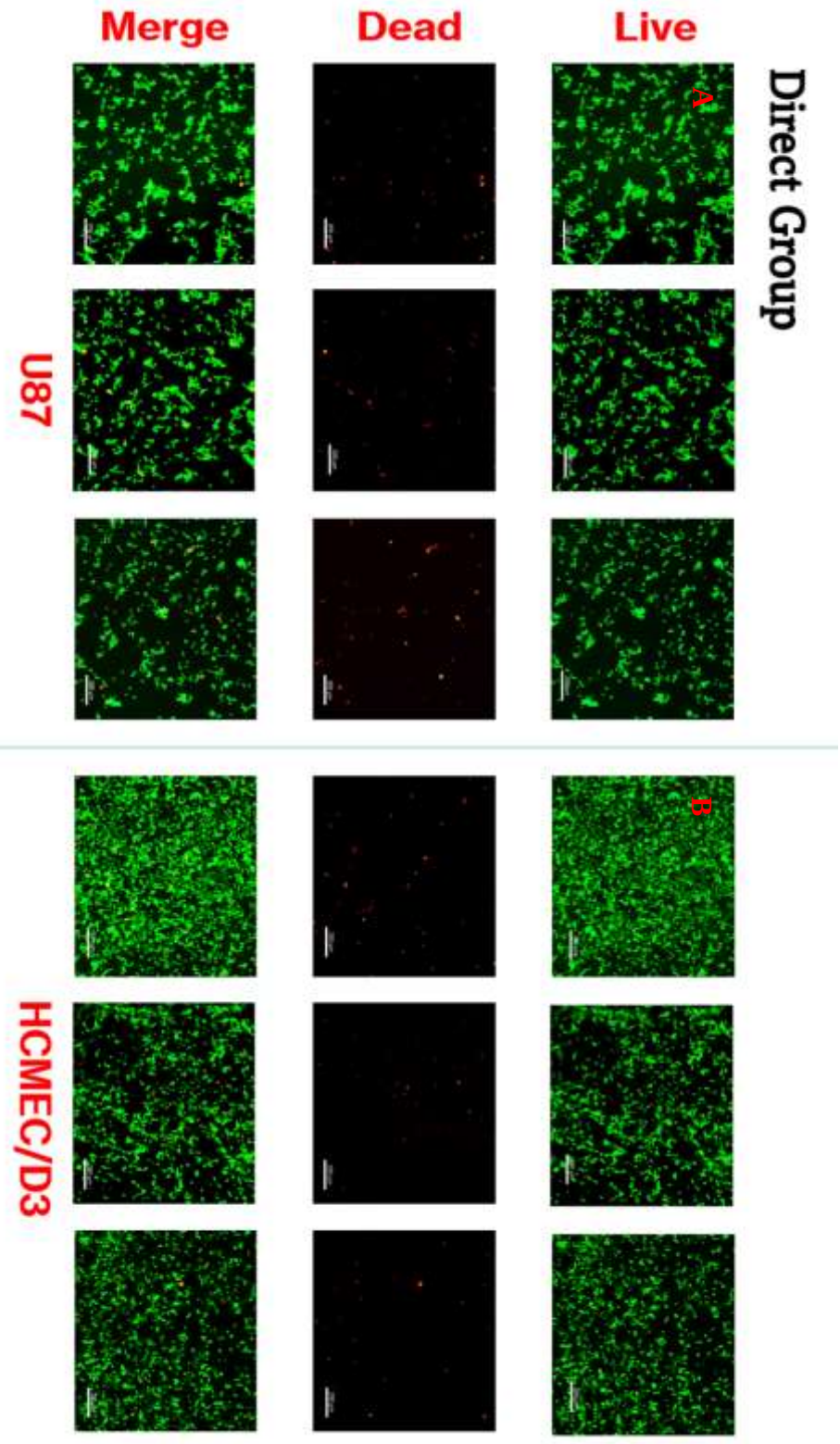

Figure 4.10 Representative Live/Dead fluorescence microscopy images of U87 glioblastoma cells (A) and hCMEC/D3 endothelial cells (B) in the Direct group.Scale bar: 200 μm

Cytotoxicity in U87 cells exhibited a distinct dependence on the experimental setup, with severity classified as Direct > Indirect > Naive. In the Direct group, U87 glioblastoma cells displayed significant red fluorescence and marked morphological impairment, characterized by cell rounding, membrane breakdown, and decreased confluency, signifying considerable cell mortality. In the Indirect group, U87 cells exhibited a considerable increase in red signal and a partial compromise of membrane integrity, aligning with diminished, although still notable, phototherapeutic effects conveyed via the barrier. The Naive group exhibited mostly green fluorescence, indicating elevated baseline vitality and negligible spontaneous cytotoxicity.

Conversely, hCMEC/D3 endothelial cells exhibited significantly elevated survival rates across all groups, with the highest viability observed in the Indirect group, where the Transwell barrier provided partial protection against NP-induced phototoxicity.

The Live/Dead fluorescence patterns corresponded well with LDH test results, revealing that Ti+Ta mixed MQDs produced the most significant decrease in U87 cells' viability at 25 μg/mL under 850 nm irradiation, while demonstrating low toxicity to hCMEC/D3 cells. The results indicate that the combined formulation elicits more potent cytotoxic effects than titanium or tantalum MQDs individually, especially under conditions of direct NP–cell interaction and sufficient light exposure. The findings further substantiate the idea that tantalum's superior photothermal conversion efficiency and titanium's robust photodynamic efficacy work synergistically to improve GBM destruction in the co-culture paradigm.

These data agree with previous reports on Mxene-based PDT/PTT, wherein near-infrared-responsive Ti_3C_2 platforms induce significant photothermal/photodynamic damage in tumor models while minimizing harm to non-malignant cells under comparable conditions (Z. Liu et al., 2018; Yu et al., 2017).

4.3 Intensity of Live/Dead Assay Results

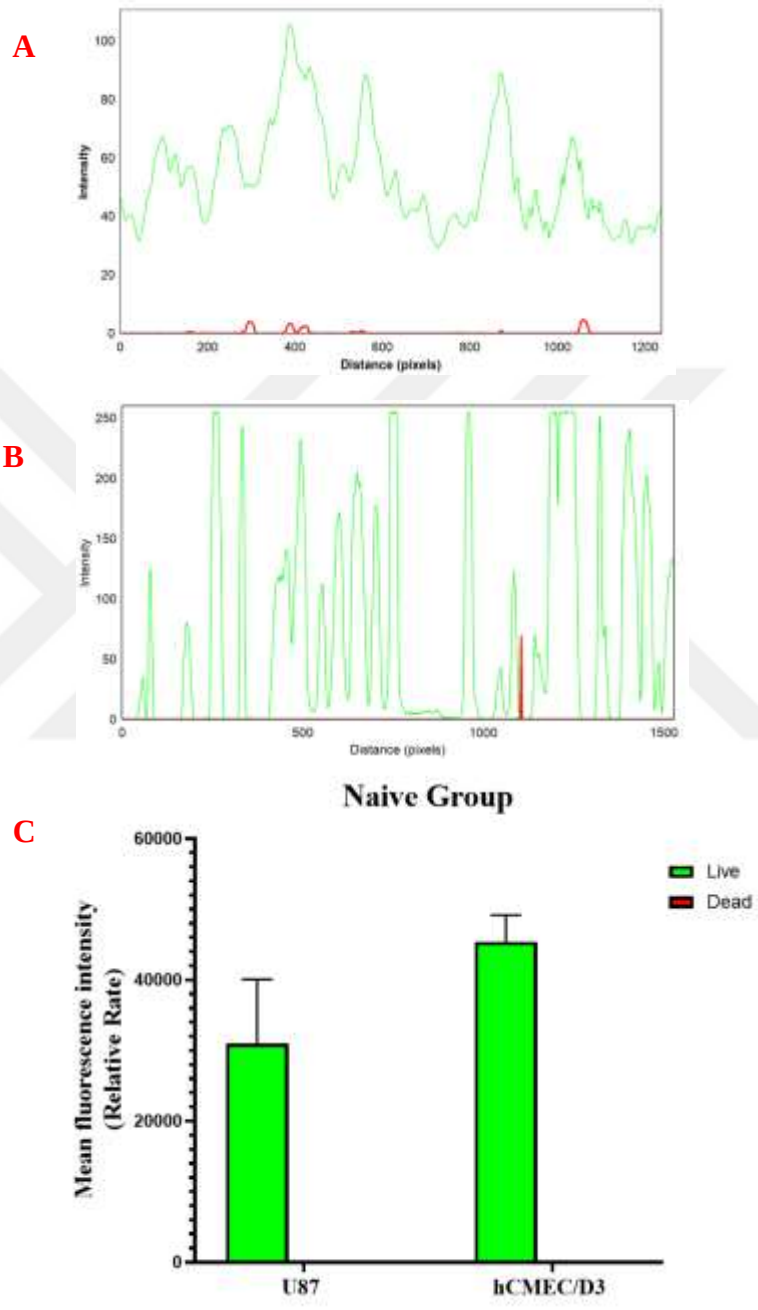

Figure 4.11 Live/Dead fluorescence intensity profiles and quantification of naive U87 and hCMEC/D3 cells

(A) Intensity profile of U87 naive cells showing sustained live-cell signal (green) and negligible dead-cell signal (red). (B) Intensity profile of hCMEC/D3 naive cells with recurrent live-cell peaks and virtually absent dead signal. (C) Quantification of mean fluorescence intensity confirms high live-cell fluorescence and minimal dead-cell signal in both U87 and hCMEC/D3 naive groups.

Live/Dead fluorescence intensity profiling was conducted on naive (negative control) U87 and hCMEC/D3 cultures to establish baseline viability prior to experimental treatments. For U87 cells, the intensity plot (Figure 4.11-A) revealed a continuous distribution of green fluorescence peaks across the scanned distance, corresponding to widespread viable cell populations. Red fluorescence, indicative of dead cells, remained at baseline levels with only sparse and low-amplitude peaks, confirming negligible cytotoxicity under naive conditions.

Similarly, the hCMEC/D3 naive group exhibited sharp and recurrent green fluorescence peaks of high amplitude (Figure 4.11-B), reflecting densely distributed viable endothelial cells. In contrast, the red fluorescence signal was virtually absent, with only a single localized peak of low intensity.

The quantitative bar graph (Figure 4.11-C) further substantiated these results, showing high mean fluorescence intensity of live signals in both U87 and hCMEC/D3 cells, with negligible dead-cell signal. As anticipated for the naive (negative control) condition, both U87 and hCMEC/D3 cells displayed a predominance of live-cell fluorescence with minimal dead-cell signal. These combined data confirm the physiological integrity and high viability of the control groups, thereby validating the reliability of subsequent comparative analyses across treatment conditions.

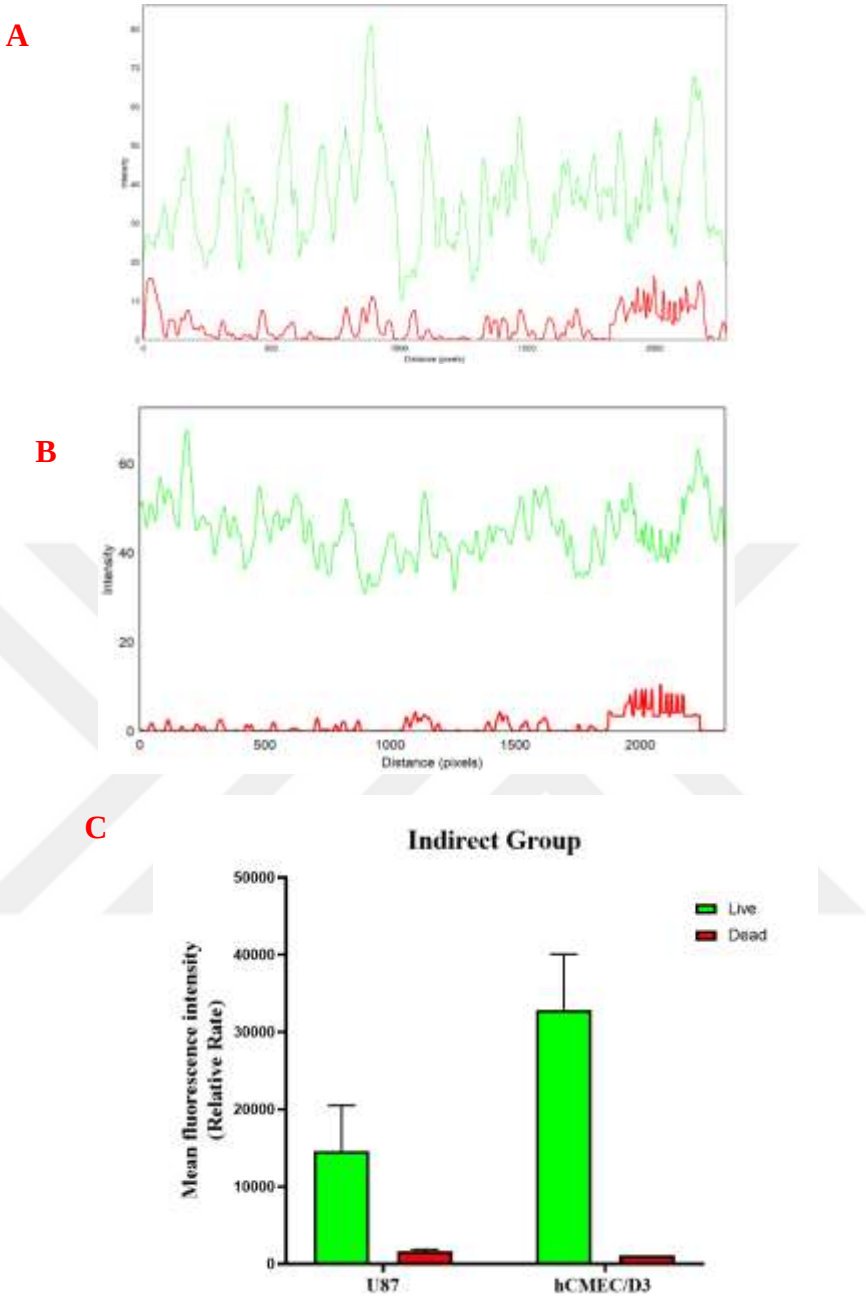

Figure 4.12 Live/Dead fluorescence intensity profiles and quantification of U87 and hCMEC/D3 cells in the Indirect (Transwell) group

(A) Intensity profile of U87 cells showing a sustained live-cell signal with localized red peaks indicating partial cytotoxicity. (B) Intensity profile of hCMEC/D3 cells demonstrating strong live-cell intensity with negligible dead-cell signal. (C) Quantification of mean fluorescence intensity confirming moderate red signal increase in U87 cells and preserved viability in hCMEC/D3 cells under indirect conditions.

In the Indirect (Transwell) configuration, where Ti+Ta MQDs and phototherapeutic illumination were applied to the upper compartment separated by the barrier, Live/Dead fluorescence intensity profiling further clarified the distinct responses of U87 and hCMEC/D3 cells.

For U87 cells, the intensity plot (Figure 4.12-A) revealed sustained green fluorescence with multiple peaks distributed across the scanned distance, reflecting a substantial population of viable cells. Nevertheless, compared to the Naive group, a noticeable elevation in red fluorescence signal was observed, particularly concentrated toward the latter portion of the scan (≈1800–2200 pixels). This pattern suggests that while the majority of U87 cells remained viable, a subset underwent cell death as a consequence of indirect exposure to Ti+Ta-mediated phototherapy.

For hCMEC/D3 cells, the intensity profile (Figure 4.12-B) displayed consistently high green fluorescence intensity across the scanned region, supporting the predominance of viable endothelial cells. Red fluorescence remained close to baseline with only sparse, low-amplitude fluctuations, slightly more pronounced than the Naive group but without any sharp or sustained peaks. This indicates minimal cytotoxicity in hCMEC/D3 monolayers under indirect conditions, confirming the protective function of the Transwell barrier.

The bar graph (Figure 4.12-C) quantitatively substantiated these observations, demonstrating that U87 cells showed a moderate but significant increase in red fluorescence intensity relative to the Naive control, whereas hCMEC/D3 cells preserved high green intensity with negligible red signal.

Together, these combined results demonstrate that in the Indirect group, U87 glioblastoma cells exhibited moderate susceptibility to Ti+Ta MQD-mediated phototherapy, while hCMEC/D3 endothelial cells largely maintained their viability. This outcome is consistent with the expected selective vulnerability of tumor cells to combined photothermal and photodynamic mechanisms when separated by a barrier system that limits direct nanoparticle contact.

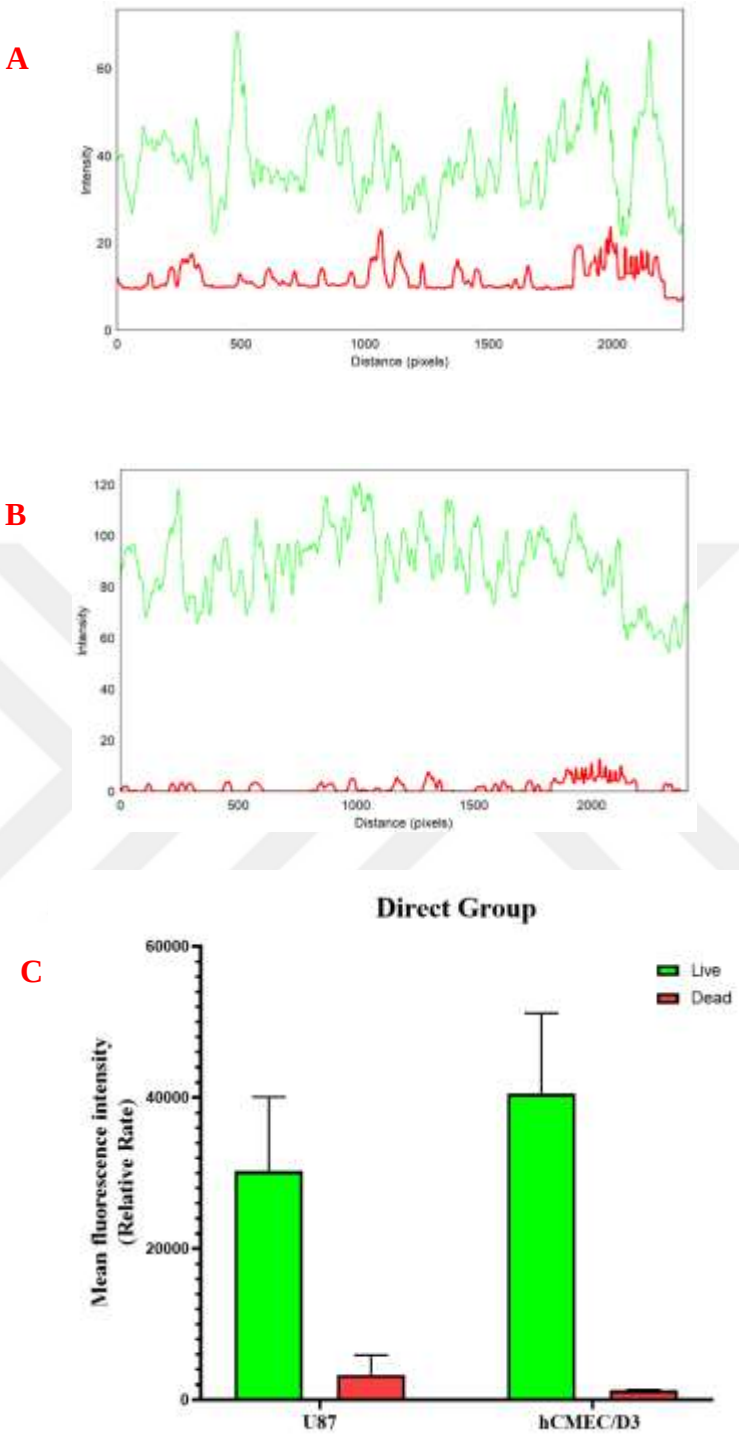

Figure 4.13 Live/Dead fluorescence intensity profiles and quantification of U87 and hCMEC/D3 cells in the Direct group

(A) Intensity profile of U87 cells showing sustained red fluorescence peaks and reduced green intensity, indicating extensive cytotoxicity. (B) Intensity profile of hCMEC/D3 cells demonstrating preserved green signal with modest red increases. (C) Bar graph quantification confirming elevated red fluorescence in U87 cells and high viability in hCMEC/D3 cells under direct nanoparticle–cell interaction.

Fluorescence intensity profiling provided a quantitative perspective on the Live/Dead assay outcomes in the Direct group. For U87 cells, the plots (Figure 4.13-A) revealed a marked elevation of red fluorescence intensity, with extended segments of the scan (≈1200–2200 pixels) showing sustained peaks, while the green signal decreased compared to Naive and Indirect conditions. This profile indicates a substantial increase in cell death and a corresponding reduction in viable populations resulting from direct nanoparticle–cell interaction.

In hCMEC/D3 cells, intensity plots (Figure 4.13-B) displayed consistently strong green fluorescence across the majority of the scanned distance, while red fluorescence exhibited modest but distinct increases relative to Naive and Indirect groups. Although endothelial cell death was detectable, its magnitude remained substantially lower than that observed in U87 cells, underscoring the relative resistance of hCMEC/D3 to Ti+Ta MQD-mediated phototherapy.

The bar graph (Figure 4.13-C) quantitatively substantiated these results, demonstrating a significant elevation of red signal in U87 cells compared to the Naive and Indirect groups, whereas hCMEC/D3 cells preserved high green intensity with only minor red increases.

Overall, the combined analyses confirmed the highest cytotoxic burden in U87 cells under Direct conditions, with only limited effects on hCMEC/D3 cells, thereby aligning with the selectivity observed in qualitative imaging. Taken together, the Live/Dead fluorescence imaging, intensity profiles, and quantitative analysis consistently demonstrated that cytotoxicity in U87 glioblastoma cells was strongly dependent on the experimental configuration, following the order Direct > Indirect > Naive. In contrast, hCMEC/D3 endothelial cells maintained high viability across all groups, with only limited increases in red signal under direct conditions and near-complete preservation of viability under indirect and naive conditions. These findings confirm the selective vulnerability of glioblastoma cells to Ti+Ta MQD-mediated phototherapy while highlighting the relative resistance of endothelial monolayers, thereby validating the co-culture Transwell model as a physiologically relevant platform for assessing therapeutic selectivity.

5. DISCUSSION

This thesis establishes an in vitro model of the BBB and BBTB utilizing hCMEC/D3 endothelial cells and U87 glioblastoma cells to assess the phototherapeutic efficacy of Ti_3C_2 and Ta_4C_3 MQDs. The primary objective was to evaluate the notion that these nanomaterials, alone or in conjunction, may penetrate physiologically relevant barrier models and selectively elicit glioblastoma cytotoxicity following NIR irradiation. Ti_3C_2 is acknowledged for its significant ability to produce ROS, facilitating PDT, whereas Ta_4C_3 demonstrates elevated photothermal conversion efficiency, rendering it appropriate for PTT (Xiaoxia Han et al., 2018; Z. Liu et al., 2018). Although these materials have been individually explored in various cancer models (Liao et al., 2023; G. Liu et al., 2017), their combined utilization in a barrier-integrated glioblastoma environment has not been previously documented, rendering our study a new addition to Mxene-based neuro-oncology.

While this is the first demonstration of dual-MQD phototherapy in barrier-integrated models, it is important to contextualise the findings within broader nanomedicine. Gold nanorods and nanoshells have been extensively studied for PTT due to their tunable plasmonic absorption in the NIR range, but their large size and poor clearance limit translational potential. Copper sulfide nanoparticles have shown strong PTT efficacy in glioblastoma xenografts (L. Gao et al., 2020), however, their stability and possible ion release elicit concerns over toxicity. Prussian blue nanocubes, FDA-approved for alternative uses, have commendable biocompatibility and robust photothermal characteristics; yet, their barrier penetration is inadequately characterized (Hill et al., 2024). Graphene quantum dots and carbon-based 0D nanomaterials exhibit elevated surface-to-volume ratios and inherent fluorescence; yet, their reactive oxygen species outputs frequently fall short compared to those of Ti_3C_2 MQDs (Kregielewski et al., 2025) have been explored for PTT or PDT in glioblastoma. These studies exhibited encouraging tumoricidal effects; nonetheless, the majority were confined to direct tumor cultures or in vivo tests without barrier integration. Even with the application of BBB/BBTB models, the emphasis remained predominantly on permeability and transport kinetics rather than on functional phototherapy results (Arvanitis et al., 2020).

To the best of our knowledge, no prior research has comprehensively examined Mxene quantum dots in barrier-based photodynamic therapy/photothermal therapy systems, nor has any study explored dual-MQD combinations inside these frameworks. This study addresses a methodological deficiency by incorporating functional therapeutic testing into Transwell-based BBB/BBTB platforms.

The observed synergy between Ti_3C_2 and Ta_4C_3 MQDs is mechanistically due to the interplay of oxidative and thermal stress. Ti_3C_2 produces reactive oxygen species that harm mitochondria, initiate apoptosis, and disrupt the redox equilibrium, whereas Ta_4C_3 raises local temperatures, denatures proteins, and suppresses the expression of defensive heat shock proteins (Kan et al., 2025; Overchuk et al., 2023). Collectively, these stimuli mutually enhance one another: heat increases cellular sensitivity to oxidative damage by augmenting perfusion and oxygenation, whereas ROS-mediated apoptosis lowers the threshold for thermal injury. This dual-stimulus synergy elucidates why tumor cell mortality was consistently higher in the combination groups compared to the single-material controls. The exact proportional roles of PDT and PTT remain unclear, as the combined formulation hinders definitive attribution. Direct thermal mapping and ROS-specific probes are necessary to determine whether the combined cytotoxicity is primarily heat-driven, ROS-driven, or genuinely synergistic.

A significant aspect of this work was the construction of two unique experimental settings, enabling the assessment of both tumor selectivity and nanoparticle penetration. In the direct arrangement, both endothelium and glioblastoma cells were concurrently exposed to MQDs and irradiated. Live/Dead imaging demonstrated extensive red staining and detachment in U87 glioblastoma cells, but hCMEC/D3 cells exhibited good vitality. This selective cytotoxicity underscores the intrinsic vulnerability of glioblastoma cells to oxidative and thermal stress, aligning with their heightened metabolic rate, disrupted redox equilibrium, and deficient antioxidant defenses (Zijian Zhou, Song, Nie, & Chen, 2016).

In addition to the qualitative Live/Dead images, fluorescence intensity plots and quantitative bar graphs provided convergent confirmation of these trends. In U87 cells,

line-scan analyses revealed a configuration-dependent escalation of red signal, with the strongest and most sustained peaks observed under direct exposure, intermediate elevations in the indirect setting, and negligible levels in the naive controls. The corresponding bar graphs further substantiated this pattern, showing significantly higher mean red fluorescence intensity in the direct group, moderate increases in the indirect group, and minimal values in the naive controls. In contrast, hCMEC/D3 cells consistently displayed high green fluorescence with only minor increases in red intensity under direct conditions and nearly baseline levels under indirect and naive conditions, a finding that was mirrored in the bar graph quantifications. These complementary datasets substantiate that the observed imaging patterns were not anecdotal but quantitatively reproducible, thereby reinforcing the conclusion that Ti_3C_2 and Ta_4C_3 MQD phototherapy selectively compromises glioblastoma viability while preserving endothelial integrity.

In the indirect configuration, MQDs were exclusively introduced into the apical chamber containing hCMEC/D3 endothelial cells, with NIR irradiation administered from above, while U87 cells were cultivated in the basolateral compartment. Tumour cells demonstrated notable cytotoxicity, albeit at reduced levels compared to the direct setting, but endothelial cells maintained viability. These data indicate that MQDs effectively penetrated the endothelium layer while maintaining phototherapeutic effectiveness post-transit. The reduced cytotoxicity compared to direct exposure is likely attributable to multiple factors: (i) partial nanoparticle loss during transit, (ii) reduction of near-infrared light intensity across the membrane and culture medium, and (iii) physical separation that reduces nanoparticle–tumor interactions. Significantly, Live/Dead analyses indicated that endothelial monolayers remained intact, implying that barrier viability was not jeopardized despite nanoparticle transit.

These outcomes are consistent with prior reports that ultrasmall nanoparticles (≤5 nm) can cross endothelial layers via vesicular and non-vesicular mechanisms(Fatima et al., 2020; Radka Gromnicova et al., 2016). The continuous eradication of glioblastoma cells in the indirect setup offers empirical evidence of nanoparticle translocation over the barrier, surpassing permeability tests to illustrate therapeutic significance.

Notwithstanding these encouraging results, some limitations warrant consideration. Initially, reactive oxygen species generation and hyperthermia were deduced from biological effects instead of being precisely quantified, resulting in an unclear mechanistic interplay between photodynamic therapy and photothermal therapy. Secondly, Live/Dead tests probably underestimated cytotoxicity because of cell loss during washing, highlighting the necessity for real-time imaging systems like Incucyte. The static Transwell system fails to simulate shear stress, an essential factor influencing endothelial physiology and nanoparticle absorption. Fourth, astrocytes, pericytes, and microglia were excluded, although these are known to modulate barrier integrity and nanoparticle interactions. Finally, only 850 nm irradiation was tested, which is suitable for both PDT and PTT but does not reveal wavelength-dependent differences such as the ROS-favouring 520 nm band or the deeper-penetrating NIR-II window.

Future investigations must tackle current limitations using a synthesis of mechanistic, biological, and translational methodologies. Accurate measurement of reactive oxygen species (ROS) and localized thermal profiles is crucial to elucidate the respective contributions of Ti_3C_2 and Ta_4C_3 to cytotoxicity and to refine treatment settings. Integrating astrocytes and pericytes into co-culture methods or utilizing microfluidic BBB-on-chip platforms would bring shear stress, extracellular matrix variability, and multicellular interactions, therefore improving the physiological accuracy of in vitro models. Validation in orthotopic glioblastoma animal models will be essential to verify biodistribution, barrier penetration, tumor inhibition, and systemic toxicity in therapeutically pertinent contexts.

In addition to these enhancements, combination treatments provide a significant pathway. PTT has demonstrated the ability to enhance drug absorption by altering tumor vasculature, indicating that MQDs may be utilized in conjunction with temozolomide to surmount chemoresistance. PDT-induced immunogenic cell death may synergize with immune checkpoint inhibitors, presenting prospects for photo-immunotherapy. Creating theranostic MQDs that can concurrently monitor ROS production, localized temperature, and medication release may enhance treatment accuracy by delivering real-time therapeutic feedback.

Future innovative strategies may encompass multiphoton excitation or fiber-optic catheter systems to address the issue of restricted light penetration in deep brain tissues, AI-driven modeling to forecast nanoparticle transport and enhance irradiation protocols, and patient-derived iPSC-based BBB/BBTB models for personalized therapy assessment. Collectively, these methodologies would augment the translational relevance of MQD-based phototherapy and perhaps alter its function in glioblastoma treatment.

This thesis presents the initial evidence that Ti_3C_2 and Ta_4C_3 MQDs may traverse barrier models and elicit selective cytotoxicity against glioblastoma upon light activation, with augmented effects seen in combination. Integrating phototherapy into barrier-integrated systems showcases both innovation and practical applicability. The current findings support the potential of dual-MQD methods; nonetheless, progression to clinical application necessitates mechanistic analysis, sophisticated in vitro modeling, in vivo validation, and the integration of multimodal therapies.

6. CONCLUSION

This thesis presents the inaugural proof that a dual-function MXene nanoplatform, including Ti_3C_2 and Ta_4C_3 quantum dots (MQDs), may induce synergistic photodynamic (PDT) and photothermal (PTT) effects against glioblastoma in physiologically pertinent in vitro blood-brain barrier (BBB) and blood-brain tumor barrier (BBTB) models. The combination of Ti_3C_2's robust ability to generate reactive oxygen species under near-infrared irradiation and Ta_4C_3's exceptional photothermal conversion efficiency resulted in significantly increased cytotoxicity in U87 glioblastoma cells compared to either nanomaterial individually, while preserving the viability of hCMEC/D3 endothelial cells. The indirect design indicated that MQDs may traverse the endothelium barrier while maintaining their therapeutic efficacy, showing functional barrier penetration without undermining endothelial integrity.

The results were corroborated using multiple assays, including Live/Dead fluorescence imaging, corresponding fluorescence intensity plots, quantitative bar graph analysis, and LDH cytotoxicity tests, all of which consistently demonstrated selective tumor cytotoxicity, minimal off-target endothelial effects, and effective penetration of tumor-compromised barriers. This selective effect appears to arise from the disruption of barriers associated with glioblastoma, modified transporter expression, and differences in nanoparticle uptake between malignant and non-malignant cells. Furthermore, the hCMEC/D3-derived BBB/BBTB model maintained essential structural and functional attributes of the human brain endothelium, underscoring its suitability as a platform for evaluating nanotherapeutic strategies in brain cancer.

Subsequent studies should expand upon these findings by directly measuring reactive oxygen species and local temperature variations to elucidate the molecular roles of photodynamic therapy and photothermal therapy. The use of sophisticated microfluidic BBB/BBTB-on-chip devices, featuring shear stress and other neurovascular unit components, will improve physiological accuracy. Enhancing nanoparticle surface chemistry for stability, targeted delivery, and regulated permeability would augment therapeutic precision. Broadening irradiation techniques to incorporate diverse

wavelengths, pulsed modalities, or multiphoton excitation may improve tissue penetration and therapeutic equilibrium. In vivo validation in orthotopic glioblastoma models is essential to evaluate biodistribution, safety, and long-term effectiveness in clinically relevant settings. Integration with adjunct therapies—such as chemotherapy to mitigate drug resistance, immunotherapy to exploit anti-tumor immunity, or gene therapy to attain sustained responses—provides further translational prospects.

The Ti_3C_2/Ta_4C_3 MQD system is an innovative dual modality nanophototherapy device that specifically targets glioblastoma while safeguarding healthy brain endothelium. This method, via mechanistic analysis, sophisticated modeling, and translational validation, shows considerable potential as a precise, minimally invasive treatment for malignant brain tumors, potentially transforming the application of phototherapy in neuro-oncology.

REFERENCES

Abbott, N. J., Patabendige, A. A., Dolman, D. E., Yusof, S. R., & Begley, D. J. (2010). Structure and function of the blood–brain barrier. Neurobiology of disease, 37(1), 13-25.

Abbott, N. J., Rönnbäck, L., & Hansson, E. (2006). Astrocyte–endothelial interactions at the blood–brain barrier. Nature Reviews Neuroscience, 7(1), 41-53.

Aboody, K., Najbauer, J., & Danks, M. (2008). Stem and progenitor cell-mediated tumor selective gene therapy. Gene therapy, 15(10), 739-752.

Al Ahmad, A., Gassmann, M., & Ogunshola, O. (2009). Maintaining blood–brain barrier integrity: pericytes perform better than astrocytes during prolonged oxygen deprivation. Journal of cellular physiology, 218(3), 612-622.

Alvarez, J. I., Dodelet-Devillers, A., Kebir, H., Ifergan, I., Fabre, P. J., Terouz, S., . . . Bernard, M. (2011). The Hedgehog pathway promotes blood-brain barrier integrity and CNS immune quiescence. science, 334(6063), 1727-1731.

Alyautdin, R., Khalin, I., Nafeeza, M. I., Haron, M. H., & Kuznetsov, D. (2014). Nanoscale drug delivery systems and the blood–brain barrier. International journal of nanomedicine, 795-811.

Amiry-Moghaddam, M., & Ottersen, O. P. (2003). The molecular basis of water transport in the brain. Nature Reviews Neuroscience, 4(12), 991-1001.

Appelt-Menzel, A., Cubukova, A., Günther, K., Edenhofer, F., Piontek, J., Krause, G., . . . Metzger, M. (2017). Establishment of a human blood-brain barrier co-culture model mimicking the neurovascular unit using induced pluri-and multipotent stem cells. Stem cell reports, 8(4), 894-906.

Argaw, A. T., Asp, L., Zhang, J., Navrazhina, K., Pham, T., Mariani, J. N., . . . Kramer, E. G. (2012). Astrocyte-derived VEGF-A drives blood-brain barrier disruption in CNS inflammatory disease. The Journal of Clinical Investigation, 122(7), 2454-2468.

Armulik, A., Genové, G., & Betsholtz, C. (2011). Pericytes: developmental, physiological, and pathological perspectives, problems, and promises. Developmental cell, 21(2), 193-215.

Armulik, A., Genové, G., Mäe, M., Nisancioglu, M. H., Wallgard, E., Niaudet, C., . . . Strittmatter, K. (2010). Pericytes regulate the blood–brain barrier. Nature, 468(7323), 557-561.

Arvanitis, C. D., Ferraro, G. B., & Jain, R. K. (2020). The blood–brain barrier and blood–tumour barrier in brain tumours and metastases. Nature Reviews Cancer, 20(1), 26-41.

Ashraf, I., Ahmad, S., Nazir, F., Dastan, D., Shi, Z., Garmestani, H., & Iqbal, M. (2022). Hydrothermal synthesis and water splitting application of d-Ti3C2 MXene/V2O5 hybrid nanostructures as an efficient bifunctional catalyst. International Journal of Hydrogen Energy, 47(64), 27383-27396.

Barbu, E., Molnàr, É., Tsibouklis, J., & Górecki, D. C. (2009). The potential for nanoparticle-based drug delivery to the brain: overcoming the blood–brain barrier. Expert opinion on drug delivery, 6(6), 553-565.

Barciszewska, A., Belter, A., Barciszewski, J., Gawrońska, I., Giel-Pietraszuk, M., & Naskręt-Barciszewska, M. (2024). P26. 09. A METFORMIN REPURPOSING FOR GLIOBLASTOMA TREATMENT. Neuro-oncology, 26(Supplement_5), v134-v134.

Bazzoni, G., Martınez-Estrada, O. M., Orsenigo, F., Cordenonsi, M., Citi, S., & Dejana, E. (2000). Interaction of junctional adhesion molecule with the tight junction components ZO-1, cingulin, and occludin. Journal of Biological Chemistry, 275(27), 20520-20526.

Bell, R. D., Winkler, E. A., Sagare, A. P., Singh, I., LaRue, B., Deane, R., & Zlokovic, B. V. (2010). Pericytes control key neurovascular functions and neuronal phenotype in the adult brain and during brain aging. Neuron, 68(3), 409-427.

Berthiaume, A.-A., Hartmann, D. A., Majesky, M. W., Bhat, N. R., & Shih, A. Y. (2018). Pericyte structural remodeling in cerebrovascular health and homeostasis. Frontiers in aging neuroscience, 10, 210.

Braun, K., Stürzel, C. M., Biskupek, J., Kaiser, U., Kirchhoff, F., & Lindén, M. (2018). Comparison of different cytotoxicity assays for in vitro evaluation of mesoporous silica nanoparticles. Toxicology in vitro, 52, 214-221.

Brown, J. A., Pensabene, V., Markov, D. A., Allwardt, V., Neely, M. D., Shi, M., . . . Brewer, B. M. (2015). Recreating blood-brain barrier physiology and structure on chip: A novel neurovascular microfluidic bioreactor. Biomicrofluidics, 9(5).

Cardoso, F. L., Brites, D., & Brito, M. A. (2010). Looking at the blood–brain barrier: molecular anatomy and possible investigation approaches. Brain research reviews, 64(2), 328-363.

Cecchelli, R., Berezowski, V., Lundquist, S., Culot, M., Renftel, M., Dehouck, M.-P., & Fenart, L. (2007). Modelling of the blood–brain barrier in drug discovery and development. Nature reviews Drug discovery, 6(8), 650-661.

Chakroun, R. W., Zhang, P., Lin, R., Schiapparelli, P., Quinones-Hinojosa, A., & Cui, H. (2018). Nanotherapeutic systems for local treatment of brain tumors. Wiley Interdisciplinary Reviews: Nanomedicine and Nanobiotechnology, 10(1), e1479.

Chen, H., Ji, J., Zhang, L., Luo, C., Chen, T., Zhang, Y., . . . Wang, J. (2024). Nanoparticles Coated with Brain Microvascular Endothelial Cell Membranes can

Target and Cross the Blood–Brain Barrier to Deliver Drugs to Brain Tumors. Small, 20(29), 2306714.

Chen, L.-J., Sun, S.-K., Wang, Y., Yang, C.-X., Wu, S.-Q., & Yan, X.-P. (2016). Activatable multifunctional persistent luminescence nanoparticle/copper sulfide nanoprobe for in vivo luminescence imaging-guided photothermal therapy. ACS applied materials & interfaces, 8(48), 32667-32674.

Chen, L., Dai, X., Feng, W., & Chen, Y. (2022). Biomedical applications of MXenes: from nanomedicine to biomaterials. Accounts of Materials Research, 3(8), 785-798.

Chen, Z., Zhao, P., Luo, Z., Zheng, M., Tian, H., Gong, P., . . . Ma, A. (2016). Cancer cell membrane–biomimetic nanoparticles for homologous-targeting dual-modal imaging and photothermal therapy. ACS nano, 10(11), 10049-10057.

Cheng, L., Huang, Z., Zhou, W., Wu, Q., Donnola, S., Liu, J. K., . . . Lathia, J. D. (2013). Glioblastoma stem cells generate vascular pericytes to support vessel function and tumor growth. Cell, 153(1), 139-152.

Cheng, X., Sun, R., Yin, L., Chai, Z., Shi, H., & Gao, M. (2017). Light-triggered assembly of gold nanoparticles for photothermal therapy and photoacoustic imaging of tumors in vivo. Advanced materials, 29(6), 1604894.

Choi, J., & Kim, S. Y. (2020). Photothermally enhanced photodynamic therapy based on glutathione-responsive pheophorbide a-conjugated gold nanorod formulations for cancer theranostic applications. Journal of Industrial and Engineering Chemistry, 85, 66-74.

Choudhari, M., Hejmady, S., Saha, R. N., Damle, S., Singhvi, G., Alexander, A., . . . Dubey, S. K. (2021). Evolving new-age strategies to transport therapeutics across the blood-brain-barrier. International journal of pharmaceutics, 599, 120351.

Chu, Z., Tian, T., Tao, Z., Yang, J., Chen, B., Chen, H., . . . Wang, H. (2022). Upconversion nanoparticles@ AgBiS2 core-shell nanoparticles with cancer-cell-specific cytotoxicity for combined photothermal and photodynamic therapy of cancers. Bioactive materials, 17, 71-80.

Cooke, V. G., LeBleu, V. S., Keskin, D., Khan, Z., O'Connell, J. T., Teng, Y., . . . Vong, S. (2012). Pericyte depletion results in hypoxia-associated epithelial-to-mesenchymal transition and metastasis mediated by met signaling pathway. Cancer cell, 21(1), 66-81.

Cornelissen, F. M., Markert, G., Deutsch, G., Antonara, M., Faaij, N., Bartelink, I., . . . Westerman, B. A. (2023). Explaining blood–brain barrier permeability of small molecules by integrated analysis of different transport mechanisms. Journal of Medicinal Chemistry, 66(11), 7253-7267.

Cuitian, C., Ziqing, D., Yan, Y., Ruixiang, L., Liang, P., Jianming, L., . . . Jianxin, W. (2017). Peptide-22 and Cyclic RGD Functionalized Liposomes for Glioma Targeting Drug Delivery Overcoming BBB and BBTB.

da Silva Chaves, C. A. (2016). Mechanisms of regulation of P-glycoprotein and breast cancer resistance protein at the blood-brain barrier: focus on the role of morphine, and P-glycoprotein activation: Universidade do Porto (Portugal).

Daneman, R., & Prat, A. (2015). The blood–brain barrier. Cold Spring Harbor perspectives in biology, 7(1), a020412.

Darrigues, E., Nima, Z. A., Griffin, R. J., Anderson, J. M., Biris, A. S., & Rodriguez, A. (2020). 3D cultures for modeling nanomaterial-based photothermal therapy. Nanoscale Horizons, 5(3), 400-430.

Dejana, E., & Orsenigo, F. (2013). Endothelial adherens junctions at a glance. Journal of cell science, 126(12), 2545-2549.

Dejana, E., Tournier-Lasserve, E., & Weinstein, B. M. (2009). The control of vascular integrity by endothelial cell junctions: molecular basis and pathological implications. Developmental cell, 16(2), 209-221.

Dmitriev, R. I., Borisov, S. M., Jenkins, J., & Papkovsky, D. B. (2015). Multi-parametric imaging of tumor spheroids with ultra-bright and tunable nanoparticle O2 probes. Paper presented at the Imaging, manipulation, and analysis of biomolecules, cells, and tissues XIII.

Domingo-Diez, J., Souiade, L., Manzaneda-González, V., Sánchez-Díez, M., Megías, D., Guerrero-Martínez, A., . . . Ramos-Gómez, M. (2023). Effectiveness of Gold Nanorods of Different Sizes in Photothermal Therapy to Eliminate Melanoma and Glioblastoma Cells. International Journal of Molecular Sciences, 24. doi:10.3390/ijms241713306

Eder, K. M., Marzi, A., Wågbø, A. M., Vermeulen, J. P., de la Fonteyne-Blankestijn, L. J., Rösslein, M., . . . Schnekenburger, J. (2022). Standardization of an in vitro assay matrix to assess cytotoxicity of organic nanocarriers: a pilot interlaboratory comparison. Drug delivery and translational research, 12(9), 2187-2206.

El Kheir, W., Marcos, B., Virgilio, N., Paquette, B., Faucheux, N., & Lauzon, M.-A. (2022). Drug delivery systems in the development of novel strategies for glioblastoma treatment. Pharmaceutics, 14(6), 1189.

Engelhardt, B. (2003). Development of the blood-brain barrier. Cell and tissue research, 314(1), 119-129.

Engelhardt, B., & Ransohoff, R. M. (2005). The ins and outs of T-lymphocyte trafficking to the CNS: anatomical sites and molecular mechanisms. Trends in immunology, 26(9), 485-495.

F Morales, J., Scioli Montoto, S., Fagiolino, P., & E Ruiz, M. (2017). Current state and future perspectives in QSAR models to predict blood-brain barrier penetration in central nervous system drug R&D. Mini reviews in medicinal chemistry, 17(3), 247-257.

Fang, X., Gong, R., Yang, D., Li, C., Zhang, Y., Wang, Y., . . . Zhang, B. (2024). NIR-II light-driven genetically engineered exosome nanocatalysts for efficient phototherapy against glioblastoma. Journal of the American Chemical Society, 146(22), 15251-15263.

Fatima, N., Gromnicova, R., Loughlin, J., Sharrack, B., & Male, D. (2020). Gold nanocarriers for transport of oligonucleotides across brain endothelial cells. PloS one, 15(9), e0236611.

Fröhlich, E. (2012). The role of surface charge in cellular uptake and cytotoxicity of medical nanoparticles. International journal of nanomedicine, 5577-5591.

Furuse, M., Hirase, T., Itoh, M., Nagafuchi, A., Yonemura, S., Tsukita, S., & Tsukita, S. (1993). Occludin: a novel integral membrane protein localizing at tight junctions. The Journal of cell biology, 123(6), 1777-1788.

Gao, H. (2016). Progress and perspectives on targeting nanoparticles for brain drug delivery. Acta Pharmaceutica Sinica B, 6(4), 268-286.

Gao, L., Zhang, L., Zhu, X., Chen, J., Zhao, M., Li, S., . . . Guo, Z. (2020). Hyaluronic acid functionalized gold nanorods combined with copper-based therapeutic agents for chemo-photothermal cancer therapy. J Mater Chem B, 8(22), 4841-4845. doi:10.1039/d0tb00097c

Garberg, P., Ball, M., Borg, N., Cecchelli, R., Fenart, L., Hurst, R., . . . Raub, T. (2005). In vitro models for the blood–brain barrier. Toxicology in vitro, 19(3), 299-334.

Gerhardt, H., & Betsholtz, C. (2003). Endothelial-pericyte interactions in angiogenesis. Cell and tissue research, 314, 15-23.

Godyń, J., Gucwa, D., Kobrlova, T., Novak, M., Soukup, O., Malawska, B., & Bajda, M. (2020). Novel application of capillary electrophoresis with a liposome coated capillary for prediction of blood-brain barrier permeability. Talanta, 217, 121023.

Gomez, K., Yarmey, V. R., Mane, H., & San-Miguel, A. (2025). Microfluidic and computational tools for neurodegeneration studies. Annual Review of Chemical and Biomolecular Engineering, 16.

Gonzalez-Carter, D., Liu, X., Tockary, T. A., Dirisala, A., Toh, K., Anraku, Y., & Kataoka, K. (2020). Targeting nanoparticles to the brain by exploiting the blood–brain barrier impermeability to selectively label the brain endothelium. Proceedings of the National Academy of Sciences, 117(32), 19141-19150.

Göritz, C., Dias, D. O., Tomilin, N., Barbacid, M., Shupliakov, O., & Frisén, J. (2011). A pericyte origin of spinal cord scar tissue. science, 333(6039), 238-242.

Gromnicova, R., Davies, H. A., Sreekanthreddy, P., Romero, I. A., Lund, T., Roitt, I. M., . . . Male, D. K. (2013). Glucose-coated gold nanoparticles transfer across human brain endothelium and enter astrocytes in vitro. PloS one, 8(12), e81043. doi:10.1371/journal.pone.0081043

Gromnicova, R., Kaya, M., Romero, I. A., Williams, P., Satchell, S., Sharrack, B., & Male, D. (2016). Transport of gold nanoparticles by vascular endothelium from different human tissues. PloS one, 11(8), e0161610.

Gust, J., Hay, K. A., Hanafi, L.-A., Li, D., Myerson, D., Gonzalez-Cuyar, L. F., . . . Lopez, J. A. (2017). Endothelial activation and blood–brain barrier disruption in neurotoxicity after adoptive immunotherapy with CD19 CAR-T cells. Cancer discovery, 7(12), 1404-1419.

Halfter, W., Dong, S., Yip, Y.-P., Willem, M., & Mayer, U. (2002). A critical function of the pial basement membrane in cortical histogenesis. Journal of Neuroscience, 22(14), 6029-6040.

Han, H. S., & Choi, K. Y. (2021). Advances in nanomaterial-mediated photothermal cancer therapies: toward clinical applications. Biomedicines, 9(3), 305.

Han, X., Gelein, R., Corson, N., Wade-Mercer, P., Jiang, J., Biswas, P., . . . Oberdörster, G. (2011). Validation of an LDH assay for assessing nanoparticle toxicity. Toxicology, 287(1-3), 99-104.

Han, X., Huang, J., Lin, H., Wang, Z., Li, P., & Chen, Y. (2018). 2D ultrathin MXene-based drug-delivery nanoplatform for synergistic photothermal ablation and chemotherapy of cancer. Advanced Healthcare Materials, 7(9), 1701394.

Hanada, S., Fujioka, K., Inoue, Y., Kanaya, F., Manome, Y., & Yamamoto, K. (2014). Cell-based in vitro blood–brain barrier model can rapidly evaluate nanoparticles' brain permeability in association with particle size and surface modification. International Journal of Molecular Sciences, 15(2), 1812-1825.

Hatherell, K., Couraud, P.-O., Romero, I. A., Weksler, B., & Pilkington, G. J. (2011). Development of a three-dimensional, all-human in vitro model of the blood–brain barrier using mono-, co-, and tri-cultivation Transwell models. Journal of neuroscience methods, 199(2), 223-229.

Hawkins, B. T., & Davis, T. P. (2005). The blood-brain barrier/neurovascular unit in health and disease. Pharmacological reviews, 57(2), 173-185.

Hayashi, Y., Nomura, M., Yamagishi, S. I., Harada, S. I., Yamashita, J., & Yamamoto, H. (1997). Induction of various blood-brain barrier properties in non-neural endothelial cells by close apposition to co-cultured astrocytes. Glia, 19(1), 13-26.

He, X., Liu, Y., Lin, X., Yuan, F., Long, D., Zhang, Z., . . . Yang, G.-Y. (2018). Netrin-1 attenuates brain injury after middle cerebral artery occlusion via downregulation of astrocyte activation in mice. Journal of neuroinflammation, 15(1), 268.

Helms, H. C., Abbott, N. J., Burek, M., Cecchelli, R., Couraud, P.-O., Deli, M. A., . . . Shusta, E. V. (2016). In vitro models of the blood–brain barrier: an overview of commonly used brain endothelial cell culture models and guidelines for their use. Journal of Cerebral Blood Flow & Metabolism, 36(5), 862-890.

Hill, M. L., Chung, S. J., Woo, H. J., Park, C. R., Hadrick, K., Nafiujjaman, M., . . . Kim, T. (2024). Exosome-Coated Prussian Blue Nanoparticles for Specific Targeting and Treatment of Glioblastoma. ACS Appl Mater Interfaces, 16(16), 20286-20301. doi:10.1021/acsami.4c02364

Hiremath, N., Kumar, R., Hwang, K. C., Banerjee, I., Thangudu, S., & Vankayala, R. (2022). Near-infrared light activatable two-dimensional nanomaterials for theranostic applications: a comprehensive review. ACS applied nano materials, 5(2), 1719-1733.

Hoffmann, A., Bredno, J., Wendland, M., Derugin, N., Ohara, P., & Wintermark, M. (2011). High and low molecular weight fluorescein isothiocyanate (FITC)–dextrans to assess blood-brain barrier disruption: Technical considerations. Translational stroke research, 2(1), 106-111.

Hoshyar, N., Gray, S., Han, H., & Bao, G. (2016). The effect of nanoparticle size on in vivo pharmacokinetics and cellular interaction. Nanomedicine, 11(6), 673-692.

Hou, Y.-j., Yang, X.-x., Liu, R.-q., Zhao, D., Guo, C.-x., Zhu, A.-c., . . . Meng, H.-x. (2020). Pathological mechanism of photodynamic therapy and photothermal therapy based on nanoparticles. International journal of nanomedicine, 6827-6838.

Hsu, J.-F., Chu, S.-M., Liao, C.-C., Wang, C.-J., Wang, Y.-S., Lai, M.-Y., . . . Tsai, M.-H. (2021). Nanotechnology and nanocarrier-based drug delivery as the potential therapeutic strategy for glioblastoma multiforme: An update. Cancers, 13(2), 195.

Hu, C.-M. J., & Zhang, L. (2012). Nanoparticle-based combination therapy toward overcoming drug resistance in cancer. Biochemical pharmacology, 83(8), 1104-1111.

Huang, J., Li, Y. B., Charlebois, C., Nguyen, T., Liu, Z., Bloemberg, D., . . . Leclerc, S. (2022). Application of blood brain barrier models in pre-clinical assessment of glioblastoma-targeting CAR-T based immunotherapies. Fluids and Barriers of the CNS, 19(1), 38.

Huang, X., Wu, J., He, M., Hou, X., Wang, Y., Cai, X., . . . Chen, Y. (2019). Combined cancer chemo-photodynamic and photothermal therapy based on ICG/PDA/TPZ-loaded nanoparticles. Molecular pharmaceutics, 16(5), 2172-2183.

Huber, J. D., Hau, V. S., Mark, K. S., Brown, R. C., Campos, C. R., & Davis, T. P. (2002). Viability of microvascular endothelial cells to direct exposure of formalin, λ-carrageenan, and complete Freund's adjuvant. European journal of pharmacology, 450(3), 297-304.

Hynynen, K., & McDannold, N. (2004). MRI guided and monitored focused ultrasound thermal ablation methods: a review of progress. International journal of hyperthermia, 20(7), 725-737.

Jain, R. K., Di Tomaso, E., Duda, D. G., Loeffler, J. S., Sorensen, A. G., & Batchelor, T. T. (2007). Angiogenesis in brain tumours. Nature Reviews Neuroscience, 8(8), 610-622.

Jain, R. K., & Stylianopoulos, T. (2010). Delivering nanomedicine to solid tumors. Nature reviews Clinical oncology, 7(11), 653-664.

Jia, Y., Wang, X., Hu, D., Wang, P., Liu, Q., Zhang, X., . . . Liu, B. (2018). Phototheranostics: active targeting of orthotopic glioma using biomimetic proteolipid nanoparticles. ACS nano, 13(1), 386-398.

Jiang, T., Zhan, Y., Ding, J., Song, Z., Zhang, Y., Li, J., & Su, T. (2024). Biomimetic Cell Membrane-Coated Nanoparticles for Cancer Theranostics. ChemMedChem, 19(22), e202400410.

Kadry, H., & Cucullo, L. (2023). Evaluation of barrier integrity using a two-layered microfluidic device mimicking the blood-brain barrier. In Vascular hyperpermeability: methods and protocols (pp. 77-88): Springer.

Kan, D., Ding, R., Yang, H., Jia, Y., Lei, K., Wang, Z., . . . Xie, F. (2025). Synergistic strategies in photodynamic combination therapy for cancer: mechanisms, nanotechnology, and clinical translation. Frontiers in oncology, 15, 1607259.

Kaya, S., Callan, B., & Hawthorne, S. (2023). Non-invasive, targeted nanoparticle-mediated drug delivery across a novel human BBB model. Pharmaceutics, 15(5), 1382.

Kim, J., Piao, Y., & Hyeon, T. (2009). Multifunctional nanostructured materials for multimodal imaging, and simultaneous imaging and therapy. Chemical Society Reviews, 38(2), 372-390.

Kokalj, A. J., Drobne, D., & Novak, S. (2018). Nanotoxicity evaluation using experimental animals: a detailed review. Nanotoxicology: Toxicity Evaluation, Risk Assessment and Management, CRC Press, Boca Raton.

Kolhar, P., Anselmo, A. C., Gupta, V., Pant, K., Prabhakarpandian, B., Ruoslahti, E., & Mitragotri, S. (2013). Using shape effects to target antibody-coated nanoparticles to lung and brain endothelium. Proceedings of the National Academy of Sciences, 110(26), 10753-10758.

Kolter, M., Ott, M., Hauer, C., Reimold, I., & Fricker, G. (2015). Nanotoxicity of poly (n-butylcyano-acrylate) nanoparticles at the blood–brain barrier, in human whole blood and in vivo. Journal of Controlled Release, 197, 165-179.

Kong, C., & Chen, X. (2022). Combined photodynamic and photothermal therapy and immunotherapy for cancer treatment: a review. International journal of nanomedicine, 17, 6427.

Kong, W., Niu, Y., Liu, M., Zhang, K., Xu, G., Wang, Y., . . . Li, J. (2019). One-step hydrothermal synthesis of fluorescent MXene-like titanium carbonitride quantum dots. Inorganic Chemistry Communications, 105, 151-157. doi:https://doi.org/10.1016/j.inoche.2019.04.033

Kregielewski, K., Fraczek, W., & Grodzik, M. (2025). Graphene Quantum Dots for Glioblastoma Treatment and Detection-Systematic Review. Molecules, 30(12). doi:10.3390/molecules30122483

Kroll, A., Pillukat, M. H., Hahn, D., & Schnekenburger, J. (2012). Interference of engineered nanoparticles with in vitro toxicity assays. Archives of toxicology, 86(7), 1123-1136.

Lee, J., Lilly, G. D., Doty, R. C., Podsiadlo, P., & Kotov, N. A. (2009). In vitro toxicity testing of nanoparticles in 3D cell culture. Small, 5(10), 1213-1221.

Lee, S. W. L., Campisi, M., Osaki, T., Possenti, L., Mattu, C., Adriani, G., . . . Chiono, V. (2020). Modeling nanocarrier transport across a 3D in vitro human blood-brain–barrier microvasculature. Advanced Healthcare Materials, 9(7), 1901486.

Lewinski, N., Colvin, V., & Drezek, R. (2008). Cytotoxicity of nanoparticles. Small, 4(1), 26-49.

Li, J., Wang, S., Fontana, F., Tapeinos, C., Shahbazi, M.-A., Han, H., & Santos, H. A. (2023). Nanoparticles-based phototherapy systems for cancer treatment: Current status and clinical potential. Bioactive materials, 23, 471-507.

Li, Y., Wu, C., Long, X., Wang, X., Gao, W., Deng, K., . . . Liu, Q. (2024). Single-cell transcriptomic analysis of glioblastoma reveals pericytes contributing to the blood–brain–tumor barrier and tumor progression. MedComm, 5(12), e70014.

Liao, T., Chen, Z., Kuang, Y., Ren, Z., Yu, W., Rao, W., . . . Jiang, B. (2023). Small-size Ti3C2Tx MXene nanosheets coated with metal-polyphenol nanodots for enhanced cancer photothermal therapy and anti-inflammation. Acta Biomaterialia, 159, 312-323.

Liebner, S., Cavallaro, U., & Dejana, E. (2006). The multiple languages of endothelial cell-to-cell communication. Arteriosclerosis, thrombosis, and vascular biology, 26(7), 1431-1438.

Liebner, S., Corada, M., Bangsow, T., Babbage, J., Taddei, A., Czupalla, C. J., . . . Fruttiger, M. (2008). Wnt/β-catenin signaling controls development of the blood–brain barrier. Journal of Cell Biology, 183(3), 409-417.

Linville, R. M., Komin, A., Lan, X., DeStefano, J. G., Chu, C., Liu, G., . . . Searson, P. C. (2021). Reversible blood-brain barrier opening utilizing the membrane active peptide melittin in vitro and in vivo. Biomaterials, 275, 120942.

Liu, D., Dai, X., Ye, L., Wang, H., Qian, H., Cheng, H., & Wang, X. (2023). Nanotechnology meets glioblastoma multiforme: Emerging therapeutic strategies. Wiley Interdisciplinary Reviews: Nanomedicine and Nanobiotechnology, 15(1), e1838.

Liu, G., Zou, J., Tang, Q., Yang, X., Zhang, Y., Zhang, Q., . . . Dong, X. (2017). Surface modified Ti3C2 MXene nanosheets for tumor targeting photothermal/photodynamic/chemo synergistic therapy. ACS applied materials & interfaces, 9(46), 40077-40086.

Liu, S., Agalliu, D., Yu, C., & Fisher, M. (2012). The role of pericytes in blood-brain barrier function and stroke. Current pharmaceutical design, 18(25), 3653-3662.

Liu, T., Zhu, M., Chang, X., Tang, X., Yuan, P., Tian, R., . . . Chen, X. (2023). Tumor-specific photothermal-therapy-assisted immunomodulation via multiresponsive adjuvant nanoparticles. Advanced materials, 35(18), 2300086.

Liu, Z., Lin, H., Zhao, M., Dai, C., Zhang, S., Peng, W., & Chen, Y. (2018). 2D superparamagnetic tantalum carbide composite MXenes for efficient breast-cancer theranostics. Theranostics, 8(6), 1648.

Lou, O., Alcaide, P., Luscinskas, F. W., & Muller, W. A. (2007). CD99 is a key mediator of the transendothelial migration of neutrophils. The Journal of Immunology, 178(2), 1136-1143.

Löscher, W., & Potschka, H. (2005a). Blood-brain barrier active efflux transporters: ATP-binding cassette gene family. NeuroRx, 2(1), 86-98.

Löscher, W., & Potschka, H. (2005b). Drug resistance in brain diseases and the role of drug efflux transporters. Nature Reviews Neuroscience, 6(8), 591-602.

Lubin, K. E., Xu, Z., Sluka, J. P., & Knipp, G. T. (2024). Development of an in vitro model of the neurovascular unit for BBB permeability-linked neuroactivity screening. Medicinal Chemistry Research, 33(8), 1450-1463.

Luptáková, D., Vallianatou, T., Nilsson, A., Shariatgorji, R., Hammarlund-Udenaes, M., Loryan, I., & Andrén, P. E. (2021). Neuropharmacokinetic visualization of regional and subregional unbound antipsychotic drug transport across the blood–brain barrier. Molecular Psychiatry, 26(12), 7732-7745.

Marino, A., Tricinci, O., Battaglini, M., Filippeschi, C., Mattoli, V., Sinibaldi, E., & Ciofani, G. (2018). A 3D real-scale, biomimetic, and biohybrid model of the blood-brain barrier fabricated through two-photon lithography. Small, 14(6), 1702959.

Mark, K. S., & Davis, T. P. (2002). Cerebral microvascular changes in permeability and tight junctions induced by hypoxia-reoxygenation. American Journal of Physiology-Heart and Circulatory Physiology, 282(4), H1485-H1494.

Melancon, M. P., Zhou, M., & Li, C. (2011). Cancer theranostics with near-infrared light-activatable multimodal nanoparticles. Accounts of chemical research, 44(10), 947-956.

Menezes, M. J., McClenahan, F. K., Leiton, C. V., Aranmolate, A., Shan, X., & Colognato, H. (2014). The extracellular matrix protein laminin α2 regulates the maturation and function of the blood–brain barrier. Journal of Neuroscience, 34(46), 15260-15280.

Morris, E. K., Daignault-Mill, S., Stehbens, S. J., Genovesi, L. A., & Lagendijk, A. K. (2023). Addressing blood-brain-tumor-barrier heterogeneity in pediatric brain tumors with innovative preclinical models. Frontiers in oncology, 13, 1101522.

Muller, W. A., Weigl, S. A., Deng, X., & Phillips, D. M. (1993). PECAM-1 is required for transendothelial migration of leukocytes. Journal of Experimental Medicine, 178(2), 449-460.

Naeem, A., Hu, P., Yang, M., Zhang, J., Liu, Y., Zhu, W., & Zheng, Q. (2022). Natural products as anticancer agents: current status and future perspectives. Molecules, 27(23), 8367.

Nasdala, I., Wolburg-Buchholz, K., Wolburg, H., Kuhn, A., Ebnet, K., Brachtendorf, G., . . . Vestweber, D. (2002). A transmembrane tight junction protein selectively expressed on endothelial cells and platelets. Journal of Biological Chemistry, 277(18), 16294-16303.

Neal, E. H., Marinelli, N. A., Shi, Y., McClatchey, P. M., Balotin, K. M., Gullett, D. R., . . . Wikswo, J. P. (2019). A simplified, fully defined differentiation scheme for producing blood-brain barrier endothelial cells from human iPSCs. Stem cell reports, 12(6), 1380-1388.

Neumann, E., Tönsing, K., Kakorin, S., Budde, P., & Frey, J. (1998). Mechanism of electroporative dye uptake by mouse B cells. Biophysical journal, 74(1), 98-108.

Nitta, T., Hata, M., Gotoh, S., Seo, Y., Sasaki, H., Hashimoto, N., . . . Tsukita, S. (2003). Size-selective loosening of the blood-brain barrier in claudin-5–deficient mice. The Journal of cell biology, 161(3), 653-660.

Nowak, M., Brown, T. D., Graham, A., Helgeson, M. E., & Mitragotri, S. (2020). Size, shape, and flexibility influence nanoparticle transport across brain endothelium under flow. Bioengineering & translational medicine, 5(2), e10153.

Nzou, G., Wicks, R. T., VanOstrand, N. R., Mekky, G. A., Seale, S. A., El-Taibany, A., . . . Makani, V. S. (2020). Multicellular 3D neurovascular unit model for assessing hypoxia and neuroinflammation induced blood-brain barrier dysfunction. Scientific reports, 10(1), 9766.

Obermeier, B., Daneman, R., & Ransohoff, R. M. (2013). Development, maintenance and disruption of the blood-brain barrier. Nature medicine, 19(12), 1584-1596.

Overchuk, M., Weersink, R. A., Wilson, B. C., & Zheng, G. (2023). Photodynamic and photothermal therapies: synergy opportunities for nanomedicine. ACS nano, 17(9), 7979-8003.

Ozcelikkale, A., Moon, H. r., Linnes, M., & Han, B. (2017). In vitro microfluidic models of tumor microenvironment to screen transport of drugs and nanoparticles. Wiley Interdisciplinary Reviews: Nanomedicine and Nanobiotechnology, 9(5), e1460.

Padhani, A. R., & Miles, K. A. (2010). Multiparametric imaging of tumor response to therapy. Radiology, 256(2), 348-364.

Palma-Florez, S., López-Canosa, A., Moralez-Zavala, F., Castaño, O., Kogan, M. J., Samitier, J., . . . Mir, M. (2023). BBB-on-a-chip with integrated micro-TEER for permeability evaluation of multi-functionalized gold nanorods against Alzheimer's disease. Journal of nanobiotechnology, 21(1), 115.

Park, J. S., Choe, K., Khan, A., Jo, M. H., Park, H. Y., Kang, M. H., . . . Kim, M. O. (2023). Establishing co-culture blood–brain barrier models for different neurodegeneration conditions to understand its effect on BBB integrity. International Journal of Molecular Sciences, 24(6), 5283.

Petersen, E. J., Reipa, V., Xia, M., & Sharma, M. (2021). Resources for developing reliable and reproducible in vitro toxicological test methods. Chemical research in toxicology, 34(6), 1367-1369.

Prabhakarpandian, B., Shen, M.-C., Nichols, J. B., Mills, I. R., Sidoryk-Wegrzynowicz, M., Aschner, M., & Pant, K. (2013). SyM-BBB: a microfluidic blood brain barrier model. Lab on a Chip, 13(6), 1093-1101.

Quail, D. F., & Joyce, J. A. (2017). The microenvironmental landscape of brain tumors. Cancer cell, 31(3), 326-341.

Rastin, H., Zhang, B., Mazinani, A., Hassan, K., Bi, J., Tung, T. T., & Losic, D. (2020). 3D bioprinting of cell-laden electroconductive MXene nanocomposite bioinks. Nanoscale, 12(30), 16069-16080.

Raut, B., Chen, L.-J., Hori, T., & Kaji, H. (2021). An open-source add-on EVOM® device for real-time transepithelial/endothelial electrical resistance measurements in multiple transwell samples. Micromachines, 12(3), 282.

Rosenberg, G., Estrada, E., & Dencoff, J. (1998). Matrix metalloproteinases and TIMPs are associated with blood-brain barrier opening after reperfusion in rat brain. Stroke, 29(10), 2189-2195.

Rustenhoven, J., Jansson, D., Smyth, L. C., & Dragunow, M. (2017). Brain pericytes as mediators of neuroinflammation. Trends in pharmacological sciences, 38(3), 291-304.

Saitou, M., Furuse, M., Sasaki, H., Schulzke, J.-D., Fromm, M., Takano, H., . . . Tsukita, S. (2000). Complex phenotype of mice lacking occludin, a component of tight junction strands. Molecular biology of the cell, 11(12), 4131-4142.

Saraiva, C., Praça, C., Ferreira, R., Santos, T., Ferreira, L., & Bernardino, L. (2016). Nanoparticle-mediated brain drug delivery: Overcoming blood–brain barrier to treat neurodegenerative diseases. Journal of Controlled Release, 235, 34-47.

Sarkaria, J. N., Hu, L. S., Parney, I. F., Pafundi, D. H., Brinkmann, D. H., Laack, N. N., . . . Laramy, J. K. (2018). Is the blood–brain barrier really disrupted in all glioblastomas? A critical assessment of existing clinical data. Neuro-oncology, 20(2), 184-191.

Sattiraju, A., & Mintz, A. (2019). Pericytes in glioblastomas: multifaceted role within tumor microenvironments and potential for therapeutic interventions. Pericyte Biology in Disease, 65-91.

Scheibe, B. e., Wychowaniec, J. K., Scheibe, M., Peplińska, B., Jarek, M., Nowaczyk, G., & Przysiecka, Ł. (2019). Cytotoxicity assessment of Ti–Al–C based MAX phases and Ti3C2T x MXenes on human fibroblasts and cervical cancer cells. ACS Biomaterials Science & Engineering, 5(12), 6557-6569.

Schimetz, J., Shah, P., Keese, C., Dehnert, C., Detweiler, M., Michael, S., . . . Padilha, E. C. (2024). Automated measurement of transepithelial electrical resistance (TEER) in 96-well transwells using ECIS TEER96: Single and multiple time point assessments. SLAS technology, 29(1), 100116.

Shamjith, S., Murali, V. P., Joesph, M. M., TS, F., Chandana, R., Jayarajan, R. O., & Maiti, K. K. (2024). Hydrogen Sulfide-Induced Activatable Photodynamic Therapy Adjunct to Disruption of Subcellular Glycolysis in Cancer Cells by a Fluorescence-SERS Bimodal Iridium Metal–Organic Hybrid. ACS applied materials & interfaces, 16(21), 27114-27126.

Shao, W., Yang, C., Li, F., Wu, J., Wang, N., Ding, Q., . . . Ling, D. (2020). Molecular design of conjugated small molecule nanoparticles for synergistically enhanced PTT/PDT. Nano-Micro Letters, 12(1), 147.

Shilo, M., Sharon, A., Baranes, K., Motiei, M., Lellouche, J.-P. M., & Popovtzer, R. (2015). The effect of nanoparticle size on the probability to cross the blood-brain barrier: an in-vitro endothelial cell model. Journal of nanobiotechnology, 13, 1-7.

Shinde, V. R., Revi, N., Murugappan, S., Singh, S. P., & Rengan, A. K. (2022). Enhanced permeability and retention effect: A key facilitator for solid tumor targeting by nanoparticles. Photodiagnosis and Photodynamic Therapy, 39, 102915.

Simard, M., & Nedergaard, M. (2004). The neurobiology of glia in the context of water and ion homeostasis. Neuroscience, 129(4), 877-896.

Song, Y., Hu, C., Fu, Y., & Gao, H. (2022). Modulating the blood–brain tumor barrier for improving drug delivery efficiency and efficacy. View, 3(1), 20200129.

Sood, A., Kumar, A., Dev, A., Gupta, V. K., & Han, S. S. (2022). Advances in hydrogel-based microfluidic blood–brain-barrier models in oncology research. Pharmaceutics, 14(5), 993.

Srinivasan, B., Kolli, A. R., Esch, M. B., Abaci, H. E., Shuler, M. L., & Hickman, J. J. (2015). TEER measurement techniques for in vitro barrier model systems. Journal of laboratory automation, 20(2), 107-126.

Steeg, P. S. (2021). The blood–tumour barrier in cancer biology and therapy. Nature reviews Clinical oncology, 18(11), 696-714.

Straehla, J. P., Hajal, C., Safford, H. C., Offeddu, G. S., Boehnke, N., Dacoba, T. G., . . . Hammond, P. T. (2022). A predictive microfluidic model of human glioblastoma to assess trafficking of blood–brain barrier-penetrant nanoparticles. Proceedings of the National Academy of Sciences, 119(23), e2118697119.

Stylli, S. S. (2020). Novel treatment strategies for glioblastoma. In (Vol. 12, pp. 2883): MDPI.

Sun, L., Liu, H., Ye, Y., Lei, Y., Islam, R., Tan, S., . . . Cai, L. (2023). Smart nanoparticles for cancer therapy. Signal transduction and targeted therapy, 8(1), 418.

Sweeney, M. D., Ayyadurai, S., & Zlokovic, B. V. (2016). Pericytes of the neurovascular unit: key functions and signaling pathways. Nature neuroscience, 19(6), 771-783.

Sweeney, M. D., Zhao, Z., Montagne, A., Nelson, A. R., & Zlokovic, B. V. (2018). Blood-brain barrier: from physiology to disease and back. Physiological reviews.

Tang, M., Rich, J. N., & Chen, S. (2021). Biomaterials and 3D bioprinting strategies to model glioblastoma and the blood–brain barrier. Advanced materials, 33(5), 2004776.

Thomsen, M. S., Humle, N., Hede, E., Moos, T., Burkhart, A., & Thomsen, L. B. (2021). The blood-brain barrier studied in vitro across species. PloS one, 16(3), e0236770.

Thomsen, M. S., Routhe, L. J., & Moos, T. (2017). The vascular basement membrane in the healthy and pathological brain. Journal of Cerebral Blood Flow & Metabolism, 37(10), 3300-3317.

Tian, M., Sun, J., Tang, Y., Dong, B., & Lin, W. (2018). Discriminating live and dead cells in dual-color mode with a two-photon fluorescent probe based on ESIPT mechanism. Analytical chemistry, 90(1), 998-1005.

Tilling, T., Korte, D., Hoheisel, D., & Galla, H. J. (1998). Basement membrane proteins influence brain capillary endothelial barrier function in vitro. Journal of neurochemistry, 71(3), 1151-1157.

Tong, F., Hu, H., Xu, Y., Zhou, Y., Xie, R., Lei, T., . . . Gao, H. (2023). Hollow copper sulfide nanoparticles carrying ISRIB for the sensitized photothermal therapy of breast cancer and brain metastases through inhibiting stress granule formation and

reprogramming tumor-associated macrophages. Acta Pharm Sin B, 13(8), 3471-3488. doi:10.1016/j.apsb.2022.11.003

Tréhin, R., Figueiredo, J.-L., Pittet, M. J., Weissleder, R., Josephson, L., & Mahmood, U. (2006). Fluorescent nanoparticle uptake for brain tumor visualization. Neoplasia, 8(4), 302-311.

Tricinci, O., De Pasquale, D., Marino, A., Battaglini, M., Pucci, C., & Ciofani, G. (2020). A 3D biohybrid real-scale model of the brain cancer microenvironment for advanced in vitro testing. Advanced materials technologies, 5(10), 2000540.

Tsai, Y.-C., Vijayaraghavan, P., Chiang, W.-H., Chen, H.-H., Liu, T.-I., Shen, M.-Y., . . . Chiu, H.-C. (2018). Targeted delivery of functionalized upconversion nanoparticles for externally triggered photothermal/photodynamic therapies of brain glioblastoma. Theranostics, 8(5), 1435.

van der Helm, M. W., Odijk, M., Frimat, J.-P., van der Meer, A. D., Eijkel, J. C., van den Berg, A., & Segerink, L. I. (2016). Direct quantification of transendothelial electrical resistance in organs-on-chips. Biosensors and bioelectronics, 85, 924-929.

Verissimo, T. V., Santos, N. T., Silva, J. R., Azevedo, R. B., Gomes, A. J., & Lunardi, C. N. (2016). In vitro cytotoxicity and phototoxicity of surface-modified gold nanoparticles associated with neutral red as a potential drug delivery system in phototherapy. Materials Science and Engineering: C, 65, 199-204.

Wang, J. D., Khafagy, E.-S., Khanafer, K., Takayama, S., & ElSayed, M. E. (2016). Organization of endothelial cells, pericytes, and astrocytes into a 3D microfluidic in vitro model of the blood–brain Barrier. Molecular pharmaceutics, 13(3), 895-906.

Wang, M. (2016). Emerging multifunctional NIR photothermal therapy systems based on polypyrrole nanoparticles. Polymers, 8(10), 373.

Wilkins, H. N., Knerler, S. A., Warshanna, A., Colón Ortiz, R., Haas, K., Orsburn, B. C., & Williams, D. W. (2024). All Blood Brain Barrier Cell Types Demonstrate Capability to Influence Differential Tenofovir and Emtricitabine Metabolism and Transport in the Brain. ACS Pharmacology & Translational Science, 7(11), 3626-3640.

Winkler, F., Kozin, S. V., Tong, R. T., Chae, S.-S., Booth, M. F., Garkavtsev, I., . . . di Tomaso, E. (2004). Kinetics of vascular normalization by VEGFR2 blockade governs brain tumor response to radiation: role of oxygenation, angiopoietin-1, and matrix metalloproteinases. Cancer cell, 6(6), 553-563.

Wolburg, H., Noell, S., Wolburg-Buchholz, K., Mack, A., & Fallier-Becker, P. (2009). Agrin, aquaporin-4, and astrocyte polarity as an important feature of the blood-brain barrier. The Neuroscientist, 15(2), 180-193.

Wong, J. F., Mohan, M. D., Young, E. W., & Simmons, C. A. (2020). Integrated electrochemical measurement of endothelial permeability in a 3D hydrogel-based microfluidic vascular model. Biosensors and bioelectronics, 147, 111757.

Wong, M.-X., Harbour, S. N., Wee, J. L., Lau, L.-M., Andrews, R. K., & Jackson, D. E. (2004). Proteolytic cleavage of platelet endothelial cell adhesion molecule-1 (PECAM-1/CD31) is regulated by a calmodulin-binding motif. FEBS letters, 568(1-3), 70-78.

Wu, D., Chen, Q., Chen, X., Han, F., Chen, Z., & Wang, Y. (2023). The blood–brain barrier: Structure, regulation and drug delivery. Signal transduction and targeted therapy, 8(1), 217.

Wu, H., Lu, H., Xiao, W., Yang, J., Du, H., Shen, Y., . . . Ramachandran, M. (2020). Sequential targeting in crosslinking nanotheranostics for tackling the multibarriers of brain tumors. Advanced materials, 32(14), 1903759.

Xie, Q., Thompson, R., Hardy, K., DeCamp, L., Berghuis, B., Sigler, R., . . . Dykema, K. (2008). A highly invasive human glioblastoma pre-clinical model for testing therapeutics. Journal of translational medicine, 6(1), 77.

Yang, Z., Du, Y., Sun, Q., Peng, Y., Wang, R., Zhou, Y., . . . Qi, X. (2020). Albumin-based nanotheranostic probe with hypoxia alleviating potentiates synchronous multimodal imaging and phototherapy for glioma. ACS nano, 14(5), 6191-6212.

Yao, Y., Chen, Z.-L., Norris, E. H., & Strickland, S. (2014). Astrocytic laminin regulates pericyte differentiation and maintains blood brain barrier integrity. Nature communications, 5(1), 3413.

Yu, X., Cai, X., Cui, H., Lee, S.-W., Yu, X.-F., & Liu, B. (2017). Fluorine-free preparation of titanium carbide MXene quantum dots with high near-infrared photothermal performances for cancer therapy. Nanoscale, 9(45), 17859-17864.

Zamanian, J. L., Xu, L., Foo, L. C., Nouri, N., Zhou, L., Giffard, R. G., & Barres, B. A. (2012). Genomic analysis of reactive astrogliosis. Journal of Neuroscience, 32(18), 6391-6410.

Zhang, M., Wang, W., Mohammadniaei, M., Zheng, T., Zhang, Q., Ashley, J., . . . Tang, B. Z. (2021). Upregulating aggregation-induced-emission nanoparticles with blood–tumor-barrier permeability for precise photothermal eradication of brain tumors and induction of local immune responses. Advanced materials, 33(22), 2008802.

Zhang, Y. S., Aleman, J., Shin, S. R., Kilic, T., Kim, D., Mousavi Shaegh, S. A., . . . Hu, N. (2017). Multisensor-integrated organs-on-chips platform for automated and continual in situ monitoring of organoid behaviors. Proceedings of the National Academy of Sciences, 114(12), E2293-E2302.

Zhao, B., Hu, X., Chen, L., Wu, X., Wang, D., Wang, H., & Liang, C. (2024). Fe3O4@ TiO2 microspheres: harnessing O2 release and ROS generation for combination CDT/PDT/PTT/chemotherapy in tumours. Nanomaterials, 14(6), 498.

Zhao, H., Xu, J., Huang, W., Zhan, G., Zhao, Y., Chen, H., & Yang, X. (2019). Spatiotemporally light-activatable platinum nanocomplexes for selective and cooperative cancer therapy. ACS nano, 13(6), 6647-6661.

Zhou, W., Chen, C., Shi, Y., Wu, Q., Gimple, R. C., Fang, X., . . . Ping, Y.-F. (2017). Targeting glioma stem cell-derived pericytes disrupts the blood-tumor barrier and improves chemotherapeutic efficacy. Cell stem cell, 21(5), 591-603. e594.

Zhou, Z., Song, J., Nie, L., & Chen, X. (2016). Reactive oxygen species generating systems meeting challenges of photodynamic cancer therapy. Chemical Society Reviews, 45(23), 6597-6626.

Zhou, Z., Xie, J., Ma, S., Luo, X., Liu, J., Wang, S., . . . Luo, F. (2021). Construction of smart nanotheranostic platform Bi-Ag@ PVP: multimodal CT/PA imaging-guided PDT/PTT for cancer therapy. ACS omega, 6(16), 10723-10734.

Zhu, Y., Feng, L., Zhao, R., Liu, B., & Yang, P. (2024). Review of MXene-Derived Quantum Dots for Cancer Theranostics. ACS applied nano materials, 7. doi:10.1021/acsanm.3c05675